UNIVERSITAT POLITÈCNICA DE CATALUNYA

DOCTORAL THESIS

Doctoral Program in Signal Theory and Communications

On the detection of ionospheric waves, relationship with earthquakes and tsunamis

---

Author:
Heng YANG[1]

Supervisor:
Dr. Enrique MONTE-MORENO[1]
Dr. Manuel HERNÁNDEZ-PAJARES[2]

A thesis submitted in fulfillment of the requirements for the degree of Doctor of Philosophy

in the

Department of Signal Theory and Communications

April 9, 2019

[1] Department of Signal Theory and Communications, Universitat Politècnica de Catalunya, Barcelona, Spain
[2] Department of Mathematics, IonSAT, Universitat Politècnica de Catalunya, Barcelona, Spain

UNIVERSITAT POLITÈCNICA DE CATALUNYA

Abstract

Escola Tècnica Superior d'Enginyeria de Telecomunicació de Barcelona

Department of Signal Theory and Communications

Doctor of Philosophy

On the detection of ionospheric waves, relationship with earthquakes and tsunamis

by Heng YANG

The research of this thesis addresses the detection and characterization of ionospheric waves and its application to traveling ionospheric disturbances (TIDs) induced by the natural events, in particular figures out the relationship between circular TIDs and the tsunami. The characterization is done from regional detrended Vertical Total Electron Content (VTEC) maps which are obtained from the line-of-sight (LOS) paths in ionosphere from a set of Global Navigation Satellite System (GNSS) satellites to a set of ground receiver stations. Note that from the mathematical / signal-processing point of view, the problem presents two key difficulties that are (a) the fact that ionospheric sampling is nonuniform, with different density of samples that somehow reflect the distribution of ground-based stations and (b), that the estimation method can not introduce any constraints in the number of disturbances and their propagation parameters.

In the first contribution of the thesis, we propose a method for detecting the number of simultaneous TIDs from a time series of high-pass-filtered VTEC maps and their parameters. The method, which we refer to as the Atomic Decomposition Detector of TIDs (ADDTID), is tested on the detrended VTEC map corresponding to a simulated realistic scenario from the dense GNSS network, Global Positioning System Earth Observation Network (GEONET) in Japan. The contribution consists of the

detection of the exact number of independent TIDs from a nonuniform sampling of the ionospheric pierce points (IPPs). The solution to the problem is set as the estimation of the representative perturbations from a dictionary of atoms that span a linear space of possible TIDs. The estimate is done by a sparse decomposition based on the improved LASSO algorithm. These atoms consist of plane waves characterized by a wavelength, direction, and phase on a surface defined, the part of the ionosphere sounded by the GNSS observation network (e.g., GEONET, 25°N to 50°N of latitude and 125°E to 155°E of longitude). The geophysical contribution is showing the detection of several simultaneous Medium Scale Traveling Ionospheric Disturbances (MSTIDs) of different characteristics, with a continuous change in the velocity.

As the second contribution, we apply ADDTID on actual detrended VTEC data from dual-frequency Global Positioning System (GPS) measurements gathered by +1200 GPS receivers of the GEONET network. For testing the method, we have studied the MSTIDs during the Spring Equinox day of 21 March 2011. The geophysical contribution is: (a) detection of circular MSTID waves compatible by time and center with a specific earthquake; (b) simultaneous superposition of two distinct MSTIDs, with almost the same azimuth; and (c) the presence at nighttime of MSTIDs with velocities in the range 400–600 m/s. These results can be verified visually, in time evolution of the detrended VTEC maps. It is important to emphasize that the algorithm allows to observe disturbances that at first sight could go unnoticed.

In the third contribution we provide a detailed characterization of the TIDs originated from the total solar eclipse of 21 August 2017, the shadow of which crossed the United States from the Pacific to the Atlantic ocean. The analysis is also done by means of ADDTID algorithm. The set of disturbances generated by the eclipse has a richer and more varied behavior than that associated with the shock wave directly produced by cooling effects of the moon shadow. This can be modeled in part as if the umbra and penumbra of the eclipse were moving cylinders that intersects with variable elevation angle a curved surface. This projection gives rise to regions of equal penumbra with shapes similar to ellipses, with different centers and foci. The result of this is reflected in the time evolution of the TID wavelengths produced by the eclipse, which depend on the solar zenith angle of the umbra center, and also a double bow wave phenomenon, where the bow waves are generated in advance to the umbra. We show that the delay in the appearance of the disturbances with the transit of the eclipse is compatible with the physical explanations, mentioned in the text, which are linked to the different origins of the disturbances and the wavelengths. Finally, we detected a clear pattern of MSTIDs, which appeared in advance of the penumbra, which we could hypothesize as soliton waves associated with the bow wave. In all cases, the detected disturbances were checked visually on the detrended VTEC maps and keogram plots.

In the fourth contribution we characterized the MSTIDs generated during the Japan Tohoku earthquake of 11 March 2011. By means of the ADDTID algorithm, we found: (a) a confirmation of the performance of the algorithm in face of simultaneous multi-TIDs, the robustness to the curvature of the wave fronts of the perturbations and the accuracy of the estimated parameters. The results were double checked by the additional visual inspection from detrended VTEC maps and keogram plots; (b) The detection of different wave fronts between the west and east MSTIDs around the epicenter, consistent in time and space with the post-earthquake tsunami; (c) The complete evolution of the circular MSTIDs driven by the tsunami during the GNSS observable area; (d) The detection of the fast and short circular TIDs related to the acoustic waves of earthquake.

Acknowledgements

First of foremost, I would like to express my sincere gratitude to my advisors Prof. Enric Monte Moreno and Prof. Manuel Hernández Pajares, for their full support, insightful guidance, valuable advice and continued encouragement. They have opened me the door to the wonderful world of ionosphere research, taught me the knowledge, patience and imagination, encouraged me to research with freedom, and helped me out of hard periods. I am exceedingly impressed by their profound knowledge background, extensive experience, great enthusiasm, good foresight and keen insight. It has been a privilege to work with them, I am deeply honored and grateful.

I want to thank all my colleges in the department of Signal Theory and Communications, and the group of IonSAT. Their help, suggestion and encouragement have played a significant role in completing my doctoral research. Also I greatly appreciate the reviewers' thoughtful comments for the thesis.

I am thankful to the Japan Geospatial Information Authority (GSI) provides for the GPS observational data of GEONET, the US National Geodetic Survey (NGS) for the GPS observation data of CORS, the Japan world data center (WDC) for Auroral electrojet activity index, the US Geological Survey (USGS) provides global earthquake data, the US NASA's Community Coordinated Modeling Center (CCMC) for the climatic hmF2 data. I am also thankful to the US NOAA's National Centers for Environmental Information (NCEI) for the geomagnetic activity data, the solar activity data, the global historical tsunami data and the global significant earthquake data. I acknowledge that all the code regarding the Ph.D. thesis was done in Python using the machine learning library "scikit-learn".

I would like to appreciate the support of the project 2017 SGR-0851 grant of the Generalitat de Catalunya, the support of the project TEC2015-69266-P (MINECO/FEDER, UE), the support of the joint scholarship of China Scholarship Council – Universitat Politećnica de Catalunya (CSC–UPC) under the grant No. 201508390017, and the support of Yangtze Normal University of China.

I am deeply grateful to all the friends who have been with me in Barcelona during my Ph.D., this will be a splendid piece of my life. Also many thanks to my wonderful family, friends and colleges in China, for their support and blessings over past years.

Finally and more importantly, I am truly appreciative to my wife, Yanli, for her support, understanding, encouragement and companionship, in particular for everything she does for me every day during years. I am extremely grateful to my parents, for their endless love, infinite patience and full support. They have raised me up, and taught me to courageously and optimistically face all the challenges of my life, not only my Ph.D. thesis.

Contents

List of Figures

List of Tables

List of Acronyms

AM	**A**mplitude **M**odulation
ADDTID	**A**tomic **D**ecomposition **D**etector of **T**ravelling **I**onospheric **D**isturbance
AE	**A**uroral **E**lectrojet
cGII	**c**omprehensive **G**lobal navigation satellite system **I**onospheric **I**nterferometry
CORS	**C**ontinuously **O**perating **R**eference **S**tation
DST	**D**isturbance **S**torm **T**ime
EUV	**E**xtreme **U**ltra**V**iolet
GEONET	**G**NSS **E**arth **O**bservation **NET**work system
GIM	**G**lobal **I**onospheric **M**ap
GNSS	**G**lobal **N**avigation **S**atellite **S**ystem
GPS	**G**lobal **P**ositioning **S**ystem
HF	**H**igh **F**requency
hmF2	**h**eight **m**aximum of the **F2** layer
ICA	**I**ndependent **C**omponent **A**nalysis
IONEX	**ION**osphere map **EX**change format
IPP	**I**onospheric **P**ierce **P**oint
IRI	**I**nternational **R**eference **I**onosphere
LASSO	**L**east **A**bsolute **S**hrinkage and **S**election **O**perator
LARS	**L**east **A**ngle **R**egression and **S**hrinkage
LOS	**L**ine **O**f **S**ight
LOFAR	**LO**w-**F**requency **AR**ray
LSTID	**L**arge **S**cale **T**ravelling **I**onospheric **D**isturbance
MATLAB	**MAT**rix **LAB**oratory
MHD	**M**agneto-**H**y**D**rodynamic
MSTID	**M**edium **S**cale **T**ravelling **I**onospheric **D**isturbance
RANSAC	**RAN**dom **SA**mple **C**onsensus
PRN	**P**seudo **R**andom **N**oise
RINEX	**R**eceiver **IN**dependent **EX**change format
SNR	**S**ignal **N**oise **R**atio
SRMTID	**S**ingle **R**eceiver **M**S**TID**
STEC	**S**lant **T**otal **E**lectron **C**ontent

SuperDARN	**Super D**ual **A**uroral **R**adar **N**etwork
TID	**T**raveling **I**onospheric **D**isturbance
TEC	**T**otal **E**lectron **C**ontent
TECU	**T**otal **E**lectron **C**ontent **U**nit
UV	**U**ltra**V**iolet
VTEC	**V**ertical **T**otal **E**lectron **C**ontent

Dedicated to my beloved family for their love, understanding, endless support, encouragement & sacrifices.

Introduction

Motivation

This thesis addresses the detection and characterization of ionospheric disturbances. The typology of ionospheric disturbances is diverse, and one of its manifestations is in the form of waves. It is known that ionospheric disturbances can propagate as waves and have different origins. Each origin gives a specific signature, which characterizes the shape of the wave fronts and characteristics of the disturbance, such as wavelength, period, velocity, azimuth, etc. In addition, the way in which the type of disturbance manifests itself, depending on the origin, is influenced by the ionization state, and by the dynamics of the changes in the ionosphere (Hernández-Pajares et al., 2012a).

This thesis focuses on the detection and characterization of Traveling Ionospheric disturbances (TIDs), using a method that employs measurements made using satellites. The TIDs are the plasma density fluctuations that can be inferred from the detrended Total Electron Content (TEC) from the delays of the Global Navigation Satellite System (GNSS) signals, like the Global Positioning System (GPS) signals. This provides an estimate of the variation of the detrended TEC as a function of height and location. Therefore the signal measured from GNSS receivers in a given region allows us to determine the state of the ionosphere and the disturbances that are present at a given moment. Although the density of ground based stations and satellites is neither uniform nor high, in places where there are sufficient stations a good estimate of the 4D (3D + time) detrended TEC can be estimated. The latter, from the point of view of signal processing, is difficult, as it involves estimating waves, in which the total number of waves present is unknown and sampling is nonuniform, with directions in which there is a greater density of measurements and regions without measurements. The primary objective of this thesis has been to develop a tool that allows the estimation of disturbances under these conditions ensuring that biases are minimal. For this purpose, in the results that are presented, we will always compare the detections made automatically by the algorithm, with maps in which the measurements are presented and thus the reliability of the method can be checked.

The second goal of the thesis was to test the developed algorithm on problems such as characterizing TIDs in the dense GPS network of Japan on a given day, characterizing the typology of TIDs during a total solar eclipse, and finally the study of tsunamis caused by earthquakes. Note that from the point of view of signal processing, characterizing the TIDs over Japan is challenging, due to the geographical distribution of the stations that measured the state of the ionosphere, in the sense, that the density of stations followed the shape of the island, and the different ratio of length vs wide of the network, affects the resolution in wavelength depending of the direction. An interesting finding was that there were TIDs that were compatible in direction and delay with a seismologic origin. The measurement of the disturbances during an eclipse, allowed us to find different phenomena that had not been yet reported, related to the possible early soliton waves. Finally, we tested the algorithm with earthquake related tsunamis, and have found that there is a clear structure of disturbances related to the appearance of the tsunami, which are able to give information that does not appear in the Keograms. Note that tsunamis actually have other origins such as a giant lake Geneva tsunami caused by the collapse of a mountainside (see Kremer, Simpson, and Girardclos, 2012). From the temporal coherence between phenomena, i.e. time of the events and propagation time of the perturbations such as the umbra center of an solar eclipse, the epicenter of an earthquake, or relationship between the wavefront of the eclipse / tsunami and the TIDs, one can infer possible cause-effect relationships, and try to explain them by physical models. In this thesis we have checked the theoretical explanations of the disturbances, with the measurements done with the algorithm.

Natural phenomena such as eclipses, earthquakes or tsunamis create waves in the ionosphere, which in these situations consist of circular waves. These waves appear in the ionosphere with a certain delay, which can be explained by different physical origins, which we will describe in this document. These waves can be measured and characterized by the existence of dense networks of receivers covering large geographic areas, such as the US CORS network with ~ 2000 receivers or the Japanese GEONET network with ~ 1200 receivers. Other natural phenomena that create TIDs are volcano eruptions and tropical storms, which we will study in the future.

One valuable point of the research thesis is to model, recognize and determine the TIDs from measurements of GNSS networks. The result could be used for real-time detection / warning worldwide.

An open question deserving more research is the occurrence and actual source of ionospheric waves which are detected right after some natural events such as the earthquakes happening on the sea. Are they associated with the sea itself? Are they associated with the new induced natural events like tsunamis? Both? Clarifying

this point can pave the way for new, more effective and cheaper natural event warning systems. In this regard the combined UPC experience on Signal Processing and Global Navigation Satellite Systems, including the modeling of ionospheric waves (such as Medium Scale TID, MSTID for short) can facilitate to significantly advance in this research, Hernández-Pajares et al. (2012b). The results obtained have been consistent with the explanations / predictions in the literature, as outlined in the discussion sections of each chapter.

Research Objectives

The research objectives of this thesis can be summarized as the development of an algorithm that determines the number of disturbances over certain regions and their characteristics. We present the results from two viewpoints: on the one hand, the characteristics detected by the algorithm we have developed, and on the other, the maps of the ionosphere, in which the consistency with respect to the presence and characteristics of the disturbances is verified. It is important to highlight that the measurements given by the algorithm are consistent with the approximate measurements on the maps, and provide greater resolution and reliability. In addition to the results, we also discuss the literature related with the phenomena that generates the disturbances (i.e. such as solar / geomagnetic activity, atmospheric gravity waves, solar eclipse, earthquakes or tsunamis), and check the consistency of the explanations found in the literature with the different features detected by our algorithm, such as intensities, velocities, delays, etc.

The tool for detecting the number of independent disturbances, as well as their characteristics is based on signal processing and optimization tools that allow to process measurements from a network of GNSS signals. This problem is particularly hard to solve, due to the nonuniform sampling, and to the geometry of the possible distributions of GNSS stations. We denote the tool for modeling simultaneous multi-TIDs, as Atomic Decomposition Detector of TIDs (ADDTID).

This algorithm has made it possible to gather new knowledge about the dynamics of the ionosphere, in particular, the relationship between the sudden natural events such as eclipse, earthquake and tsunami and waves on the ionosphere. We present the results due to this new algorithm developed on several problems, such has the behavior of the ionospheric disturbances such as the seasonal MSTIDs in the spring equinox, the multi-MSTIDs induced by medium earthquakes / tsunamis, and the rich and wide-ranging patterns of ionospheric disturbances that appear during the solar eclipse.

The ADDTID, as currently implemented is a retrospective tool. Nevertheless, an implementation for real time operation is feasible, and the real time implementation is part of the continuation work of this thesis. This real time implementation will allow to use the ADDTID algorithm for early warnings of tsunamis, and also for improving the precision of GNSS positioning.

Atomic Decomposition Detector of Traveling Ionospheric Disturbances

The Atomic Decomposition Detector of Traveling Ionospheric Disturbances algorithm, ADDTID, see Yang, Monte-Moreno, and Hernández-Pajares (2017), can detect and characterize TIDs from the ionospheric piercing points (IPPs), by means of data from dense GNSS receiver networks (such as the US CORS network with $\sim$ 2000 receivers or the Japan GEONET network with $\sim$ 1200 receivers). The algorithm is based on the use of a dictionary of possible waves that encompass the area under study. The estimation is done approximating IPP samples in the span of the elements of the dictionary, by solving a sparse convex optimization problem with a regularization term. The solution is sparse in the sense that the use of norm ℓ_1 yields solutions with a minimum number of active elements in the subspace spanned by the dictionary. The detected TIDs are therefore, the active elements of the dictionary that best approximate the observations at the IPPs. Stating the problem in this way has several advantages, mainly, that the number and characteristics of possible waves to be detected does not have to be stated beforehand. Also, and perhaps the most challenging aspect of the estimation problem, the algorithm can work with nonuniform spatial sampling, including the presence of directions with higher density of sensors, or regions of the network lacking sensors.

Methodology

To characterize the possible relationships between the various sources and ionospheric waves (in particular wavelike TIDs), the fundamental methodology used for ADDTID consists of the following phases:

- Generation and Model of the detrended VTEC Maps
- Generation and Justification of the Wave Model
- Design and Justification of the Estimation Model
- Construction of the Dictionary, Loss Function, Regularization and Estimation Criteria

- Improved Least Absolute Shrinkage and Selection Operator (LASSO) Solution
- TIDs Determination and Parameter Estimation

Thesis Breakdown

This thesis has been focused on several research topics as follows:

- Introduction
- Chapter 1: Multi-TID modeling technique based GNSS ionospheric sounding and applied to a simulated scenario
- Chapter 2: Multi-MSTID characterization of the spring equinox day, and medium intensity earthquake / tsunami-driven TIDs detection from dense GNSS network
- Chapter 3: Detection and Description of the Different TIDs during the Solar Eclipse of 21 August 2017 in North America
- Chapter 4: Large earthquake / tsunami-driven TIDs detection from dense GNSS network of 2011 Japan Tohoku Earthquake
- Conclusion

Chapter 1

Multi-TID Modeling Technique based GNSS Ionospheric Sounding

1.1 Introduction

The ionosphere is the region of the Earth's atmosphere defined by its free electron population and located between approximately 50 to 1000 km altitude. The most frequent wavelike structures of the electron density are called Medium Scale Traveling Ionospheric Disturbances (MSTIDs), presenting variations up to a few Total Electron Content Units (TECUs) in solar cycle maximum conditions (1 TECU = 10^{16} electrons/m^2 which correspond to a $\approx$16 cm delay in L1 GPS signal). The MSTIDs have different properties in relation to the temporal and spatial variation. Typically, the MSTIDs occurring in mid-latitude are roughly characterized by periods between 15 and 60 min, horizontal wavelengths between 50 and 300 km, and velocities between 100 and 300 m/s, with predominant propagation towards the equator at daytime in local fall and winter seasons, and towards the west at night in local spring and summer seasons (see Hernández-Pajares, Juan, and Sanz, 2006; Hunsucker, 1982). Their origins include the response to atmospheric gravity waves (Hocke and Schlegel, 1996), the Solar Terminator (Hernández-Pajares, Juan, and Sanz, 2006), the Perkins instability (Kelley, 2011), the inter-hemispheric coupling effect (Otsuka et al., 2004), and others. Although the MSTID perturbation may be small compared to background electron densities, significant effects are observed in electromagnetic waves propagating through the affected ionospheric region. In particular, the GNSS signals, like the GPS signals, are affected by the time-varying and space-varying delays of the electron fluctuation densities associated with the MSTIDs. This effect can be exploited to use the GNSS system as a global ionospheric sensor (or "ionoscope") for detecting and characterizing the MSTIDs (see Hernández-Pajares et al., 2012b). The use of the GNSS for studying the ionosphere has the benefit of using a large-scale, pre-exisiting observation network, which contrasts with other techniques that

are more specific and local, such as Low-Frequency Array (LOFAR) (Mevius et al., 2016), OI 630.0 nm all-sky images (Stefanello et al., 2015) and amplitude modulation (AM) radio transmissions (Chilcote et al., 2015).

Prior GNSS MSTID studies include, Hernández-Pajares, Juan, and Sanz (2006), Hocke and Schlegel (1996), and Hunsucker (1982), which use a horizontal planar wave model over a fixed-height ionospheric thin-shell around the earth. Also, Chen et al. (2016), Lee, Kamalabadi, and Makela (2008), and Ssessanga, Kim, and Kim (2015) estimate a three-dimension (3D) structure of electron density for modeling the MSTID at variable heights by means of computerized ionospheric tomography from the large dense GNSS network. Using as source data a GNSS network, Saito, Fukao, and Miyazaki (1998) and Tsugawa et al. (2006, 2007a,b) show a high-resolution 2D mapping of the typical daytime and nighttime MSTID waves with their properties. The above mentioned 2D mappings have been validated by other observational techniques, for instance the OI 630.0 nm all-sky imagers (Shiokawa et al., 2003) and the SuperDARN HF radars (Ogawa et al., 2009). An additional method is proposed in Ding et al. (2011) and Huang et al. (2016), where they use a cross-spectra method to obtain the MSTID parameters from the GPS TEC series. An alternative is Deng et al. (2013) where the parameters of a unique MSTID plane wave are computed by spectrum analysis techniques from one-dimension (1D) space of detrended VTEC profiles from the 2D maps.

Another method for characterizing the MSTIDs using GNSS data was proposed in Hernández-Pajares, Juan, and Sanz (2006) and Hernández-Pajares et al. (2012b, 2017) where the authors introduce the comprehensive GNSS ionospheric interferometry method that estimates the characteristics of the MSTIDs, assuming a unique or predominant planar wave from the received signal of several neighboring GNSS receivers. This method computes the instantaneous wave parameters (i.e. velocity, azimuth, and wavelength) at every epoch, at the line-of-sight paths through the ionosphere from moving satellites to permanent receivers. One limitation in common with the previous methods is that this only estimates the parameters of the dominant MSTID wave. In addition to the detection of the dominant MSTID, we are interested in detecting and characterizing multiple simultaneous MSTIDs, which might have different origins and parameters.

In this work, we propose a multi-wave parameter estimation model for detecting simultaneously the number of MSTIDs present and corresponding parameters of each disturbance. This method, which we refer to as the Atomic Decomposition Detector of TIDs, ADDTID, comprises of:

1. The construction of a time-series of detrended VTEC maps. This is done from observational data of dense but sometimes nonuniform distributed receivers

of the GNSS network, such as the GEONET network in Japan or the CORS network in United States.

2. The method also comprises the construction of a redundant dictionary, i.e., a set of elements that span the space of possible MSTID waves traveling on the detrended VTEC maps. The cardinality of the dictionary will be much higher than the dimensionality of the space and will be used to reconstruct the observed detrended VTEC maps. The elements of the dictionary will consist of snapshots of planar waves at a realistic range of parameters.

3. The method performs a sparse reconstruction of the observed detrended VTEC map from a small subset of elements of the redundant dictionary. This is done by solving an optimization problem based on the norms ℓ_1 and ℓ_2. The number of selected elements of the dictionary, will give the estimated number of MSTIDs present, and the properties of each MSTID, i.e. amplitude, azimuth, wavelength, period and velocity. The technique for the sparse reconstruction is based on ideas of atomic decomposition (Chen, Donoho, and Saunders, 2001) and the Least Absolute Shrinkage and Selection Operator (LASSO) (Tibshirani, 1996).

1.2 Generation of Detrended VTEC Maps

The ionospheric combination (also called geometry-free combination) L_I is computed from the carrier phase difference between L_1 and L_2 in length units, which is an affine function of the slant total electron content (STEC), i.e., the integrated electron density of the line-of-sight path in the ionosphere from the satellite j to the i^{th} receiver, at each sample epoch t (see Hernández-Pajares et al., 2002), is given as,

$$L_{I_i}^{j}(t) = L_{1_i}^{j}(t) - L_{2_i}^{j}(t) = \alpha S_i^j(t) + B_{I_i}^{j}(t) + w_i^j(t) \tag{1.1}$$

where the linear coefficient α has the approximate value $\alpha \approx 0.105$ m/TECU, and the wind-up term $w_i^j(t)$, originating from the relative rotation between the satellite and receiver antennas, is typically at centimeter level and supposed to be corrected. $B_{I_i}^{j}(t)$, is the sometimes suddenly time-variable bias, encompassing the carrier phase ambiguities (the unknown integer number of carrier wavelengths and the non-integer satellite and receiver dependent terms) due to receiver losses of lock, i.e., cycle-slips. The bias $B_{I_i}^{j}(t)$ remains almost constant when no new losses of lock occur, so we split $L_{I_i}^{j}(t)$ into independent sub-series defined by the cycle-slips. $S_i^j(t)$, represents trends such as diurnal variations and elevation angle variation, which are characterized by extremely low frequencies and very high energies. This contrasts typical MSTID waveform characteristics, which consist of higher frequency components with lower

energies. The separation of the component related to the MSTID, from other components is done by a double difference of the time-series (i.e., bandpass filter) of measured $L_{I_i}^{j}(t)$, which we will denote as $\tilde{S}_i^j(t)$ (see Hernández-Pajares, Juan, and Sanz, 2006). In the intervals between cycle slips, the term $B_{I_i}^{j}$ can be considered constant, and thus can be eliminated by the double time difference,

$$\tilde{S}_i^j(t) \approx L_{I_i}^{j}(t) - \frac{1}{2}[L_{I_i}^{j}(t+\Delta t) + L_{I_i}^{j}(t-\Delta t)] \tag{1.2}$$

where Δt is the detrending time interval, set to 300 sec, and enhances the frequency band of the MSTIDs. From the corresponding line-of-sight path in the ionosphere we can compute VTEC from the STEC by means of a mapping function $M(t)$ approximation, assuming a thin spherical layer is placed at a mean effective height (see Hernández-Pajares et al., 2009). Also, we discarded observations with an elevation angle of less than 30° to reduce the effect of any mapping function error. We define the detrended and projected VTEC, $\tilde{V}_i^j(t)$ as the projection of the $\tilde{S}_i^j(t)$ by means of the mapping function $M(t)$ (see Hernández-Pajares et al., 2011), that is $\tilde{V}_i^j(t) = \frac{\tilde{S}_i^j(t)}{M(t)}$.

1.3 Model of Ionospheric Maps

In our model, the detrended VTEC $\tilde{V}_i^j(t)$ (satellite j and station i) contains the MSTIDs signal at the ionospheric pierce points (IPPs) located on a shell with the mean effective height where we assume the MSTID occurs. In contrast with the global ionospheric maps (GIMs) of VTEC on a worldwide scale (see Dow, Neilan, and Rizos, 2009; Hernández-Pajares et al., 2009), we reconstruct the ionospheric activity maps at a smaller scale, with a higher resolution of space-time, and generate a localized time-series of snapshots of the maps (for a similar precedent, see Tsugawa et al., 2007a,b).

We will denote the set of observed detrended VTECs $\tilde{V}_i^m(t)$ as $\tilde{V}_i^m(\phi, \lambda, t)$ (see Equation 1.3), i.e., a function of IPP geocentric latitude ϕ, longitude λ, and sample epoch t. The construction of this variable is as follows: for each satellite m and for each station i, we create a list of measurement $\tilde{V}_i^m(\phi, \lambda, t)$ at the IPP. Only satellites with elevations of $\geqslant 30°$ are used. Another selection filter includes only MSTID activity maps with more than 1,000 IPPs (i. e., with more than 80% of the potential measurements available). Thus,

$$\tilde{V}^m(\phi, \lambda, t) = \left[\tilde{V}_1^m(\phi, \lambda, t), .., \tilde{V}_i^m(\phi, \lambda, t), .., \tilde{V}_N^m(\phi, \lambda, t)\right] \tag{1.3}$$

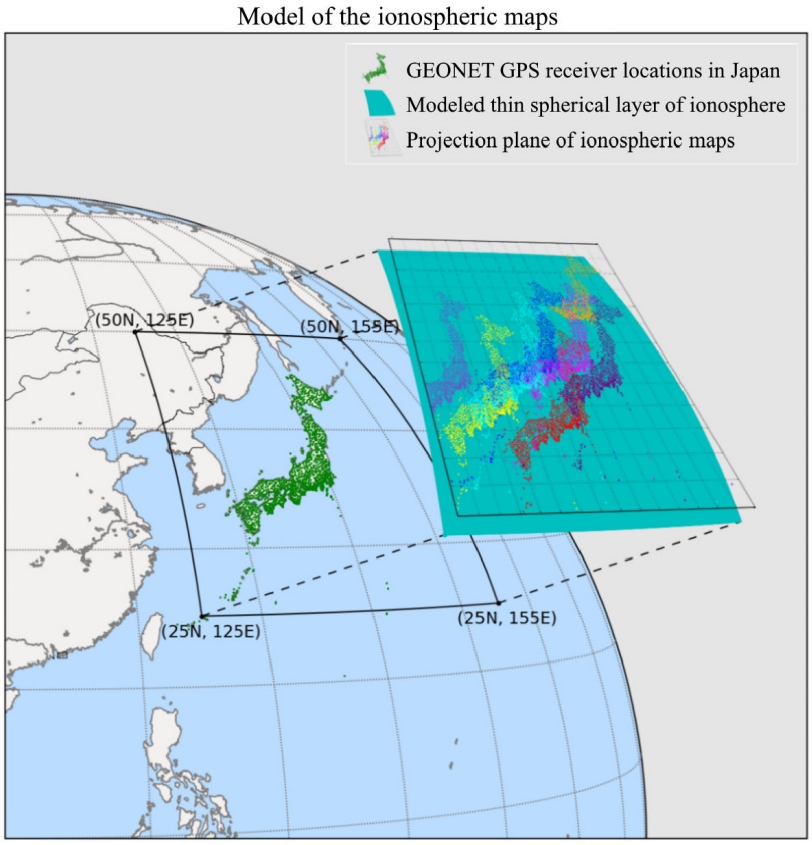

FIGURE 1.1: IPPs distribution in the ionospheric map for different satellites, e.g., the model of map for the Japan GEONET GNSS network.

In Figure 1.1, we show Japan GEONET network of GNSS receivers. Overlapped to this network and following a color code for each satellite, we also depict the detrended VTEC $\{\tilde{V}^m(\phi, \lambda, t), m = 1, 2, ..., M\}$ for all the observable satellites. Note that the set of IPPs due to each satellite will be different, and is the source of the difficulty of the estimation problem. This is because the estimation must be performed from a nonuniform 2D distribution of the observations, with variable spatial density. In addition, the different elevations of the satellites will give a different signal-to-to-noise ratio.

The range of the measured detrended VTEC by each satellite is different, thus, to improve the estimation process, the map $\tilde{V}^m(\phi, \lambda, t)$ of each satellite was normalized, assigning the value 1.0 to the 95% quantile and 0.0 to the 5% quantile. The upper and lower trimming was done so as not to bias the scale because of the outliers.

Each satellite is scaled independently of the other. To not clutter the notation, henceforth, the MSTID activity map $\tilde{V}^m(\phi, \lambda, t)$ at epoch t of satellite m will be denoted as $\tilde{V}(\phi, \lambda)$.

The variable $\tilde{V}(\phi, \lambda)$, is a 2D map, of the local time variation of the detrended VTEC. This map can be expressed in more convenient coordinates as $\tilde{V}(x, y)$ by the transformation of the pierce points from Latitude-Longitude-Height coordinates (ϕ, λ, h) to East-North-Up coordinates (x, y, z). These East-North-Up coordinates (x, y, z) are projected to the plane, i.e., horizontal coordinates (x, y). The approximation of the spherical section by a plane introduces a negligible error which is minimized by assuming the center of mass of the pierce points set as the reference point of East-North-Up coordinates.

Figure 1.1 also shows the distortion of approximating locally the curved surface of the earth by a tangent plane. The range of the IPP in the experiment is defined from 25°N to 50°N of latitude, and 125°E to 155°E of longitude. The formula that gives the error made by approximating the curvature of the spherical model by a plane, given the of figure 1.1, is,

$$error = (R + h) \cdot (\tan \frac{\alpha}{2} - \frac{\alpha}{2}) \tag{1.4}$$

where R, h are the radius of the earth and height of IPPs respectively, and α is the angle subtended by each side of the rectangle. This gives for the latitude an error of 24 km over 1488 km which is an error of about 1.61% and for the longitude an error of 42 km over 1786 km which is an error of about 2.35%.

From Figure 1.1, at a given epoch t, the image consists of a nonuniform 2D sampled representation of the IPPs at the effective height, which we will model as a linear combination of Kronecker deltas located at the set of pierce points coordinates,

$$\tilde{V}(x, y) = \sum_{(x_i, y_j) \in I_{x,y}} \alpha_{i,j} \delta(x - x_i, y - y_j) \tag{1.5}$$

where $I_{x,y}$, is the set of coordinates (x_i, y_j) of the IPPs, i.e., the coordinates of effective height (i.e., at the average MSTID activity height) of the line of sight that joins the station and the satellite, and $\alpha_{i,j}$ is proportional to the detrended VTEC at the coordinates (x_i, y_j) in the set $I_{x,y}$. The sampling is not uniform, as the samples are originated by the pierce points of the satellites, and each satellite is associated with a set of points, that mimics the shape of the projection of the stations to the effective height, as can be seen in Figure 1.1. Another effect, is that the SNR depends on the elevation of the satellite line of sight with respect to the receiver stations. The satellites are selected by an elevation mask of 30°.

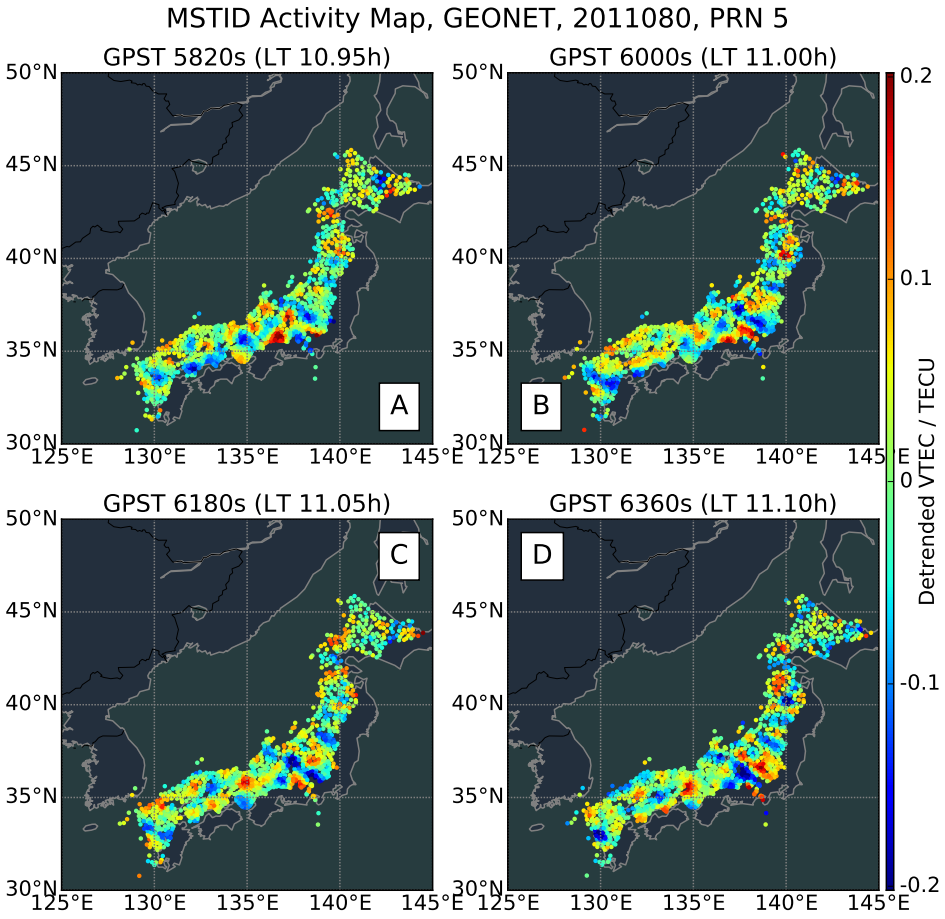

FIGURE 1.2: Wavefront propagation directly seen in the detrended VTEC maps (in TECUs), that illustrate daytime MSTIDs, from GEONET, on the 80th day of 2011. Figures A to D are the detrended VTEC maps near local noon (10:57–11:06 LT) for satellite PRN 5 (four sampling GPS time epochs 5820, 6000, 6180 and 6360 sec).

1.4 Justification of the Planar Wave Model

The problem to be solved consists of detecting and characterizing an unknown set of simultaneous MSTIDs and their properties, from a detrended VTEC map with nonuniform sampling, and spatially varying SNR.

In addition to an irregular and nonuniform spatial sampling, the model should deal with the directional bias associated with the geographical distribution of the stations. This directional bias is because the samples are aligned in directions that

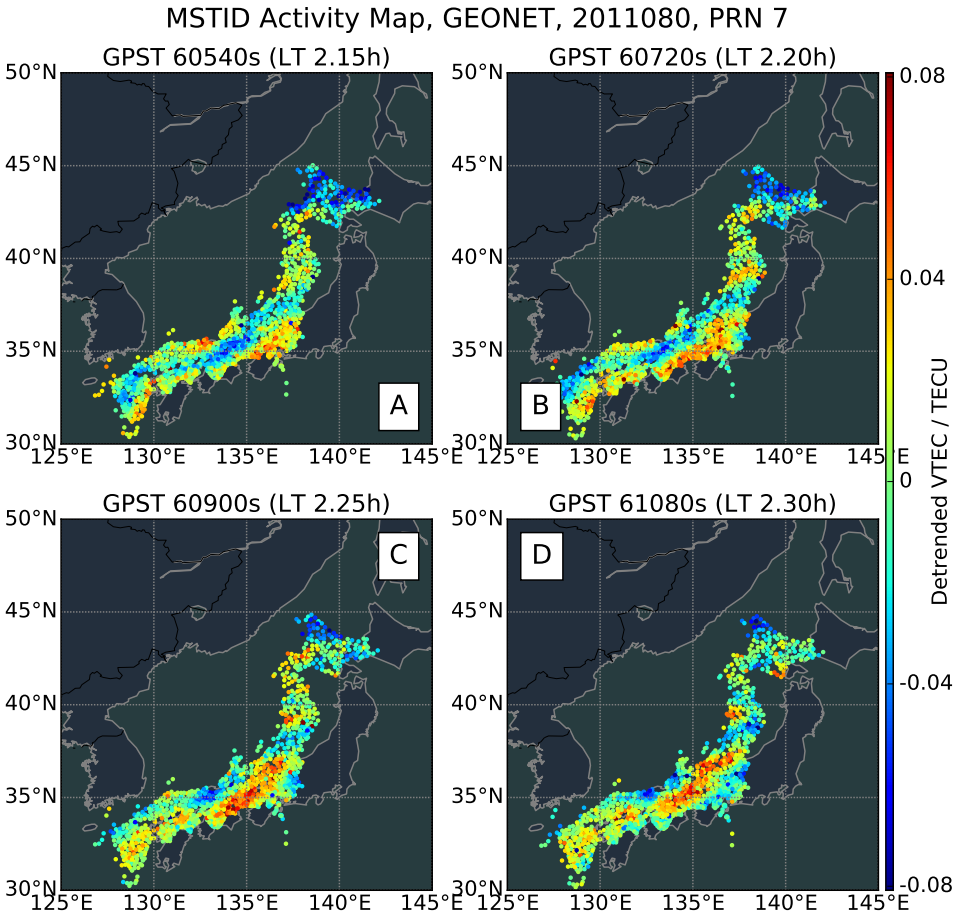

FIGURE 1.3: Wavefront propagation directly seen in the detrended VTEC maps (in TECUs), that illustrate nighttime MSTIDs, from GEONET, on the 80th day of 2011. Figures A to D are the detrended VTEC maps near local midnight (2:09–2:18 LT) for satellite PRN 7 (four sampling GPS time epochs 60540, 60720, 60900 and 61080 sec).

follow the underlying geography of the Japanese network (SW to NE). The model MSTID should consider:

1. The fact that by visual inspection, the underlying structure of the MSTID signal sometimes appears as a superposition of several plane waves (see Hernández-Pajares, Juan, and Sanz, 2006). Figure 1.2A–1.2D show the interference pattern due to several waves of similar amplitudes.

2. The complexity of the estimation process. As shown in Section 1.6.5, each additional parameter of the model entails an increase in the size of the optimization

problem, which is proportional to the product of the number of possible values of the parameters that define the atoms of the dictionary. Therefore, we have limited the model to plane waves. The inclusion of the terms that allow for modelling circular waves (this will be considered in future research) would make the problem more difficult from the computational point of view.

3. The GEONET set of receivers are located in a region that is elongated, which introduces a bias in the estimation of the parameters of the waves. For instance, in Figure 1.3A–1.3D, the number of cycles observed for a given wave depends on the azimuth.

In this paper, we will limit our model to the estimation of superposition of planar waves.

1.5 Justification of the Estimation Method

Before developing the ADDTID method, we attempted to solve the problem of nonuniform sampling by transforming the maps into regular grids of points on which the estimation of the MSTIDs was conducted. The following techniques were attempted:

- **Interpolation by means of 2D low pass filtering**. We explored different approaches to the 2D filtering, which included linear filtering, combined with techniques such as median, and morphological filtering. The 2D interpolation method was discarded because it only allowed for modelling the waves locally, and that the presence of multiple MSTID gave rise to morphologies with different spatial modes that were irregular, which did not allow for a clear detection of the different waves. Furthermore false detections appeared because the amplitude of the filtered image was modulated by the effect of non uniform sampling. This modulation that related to the different density of receivers, and also gave rise to artifacts with spatial frequencies that followed the shape of the island in the case of GEONET given by the IPP associated to each satellite.

- **Fourier transform of the smoothed 2D sampled data**. This option is based on the fact that the Fourier transform of a 2D plane wave on the map is two points in the transformed domain, and the slope of the line consisting of these two points is related to the parameters of the plane wave. This option (in combination with the previous one) was discarded because the spatial frequencies were low, and the nonuniform sampling (i.e. signal measured at the position of the pierce points) yielded Fourier transforms where the components related to the plane waves could not be discerned.

- **Hough Transformation**. Duda and Hart (1972) presented a tool for detecting partially occluded straight lines in images. We applied the Hough transform after a low pass filtering of the image, and trying different processing such as equalization, binarization, etc. in order to emphasize the linear structures. Note that in principle, this technique is promising, because one can obtain global information about linear structures from partial observations. The results were unclear and yielded a high number of false MSTIDs.

- **Independent Component Analysis (ICA)**. It is a technique that has been used for signal processing (see for instance Bartlett, Movellan, and Sejnowski, 2002; Hyvärinen, Karhunen, and Oja, 2004). This technique deals with a linear mix of unknown signals, and if the number of sources is known, it can successfully estimate the inverse of the mixing matrix. In our case, this technique is not adequate, because of the number of MSTID is unknown a priori, the fact that there might be a correlation between the MSTIDs that have to be estimated, and finally because the technique does not allow naturally to introduce constraints on the set of possible solutions.

- **Kriging**. This method is a variant of Gaussian processes (see Rasmussen and Williams, 2005), used for spatial interpolation when the observations depend on geographic coordinates. In principle, this should be a tool that is adequate to the problem at hand, because by means of the variogram model (i.e. a model of the spatial statistical dependencies) one can introduce a priori knowledge about the problem at hand. In our case we discarded this method because, although one can specify the model to be interpolated, it assumes a metric in the variogram matrix, and thus an implicit decay for points that are far from the zone with a high density of receivers. In addition it does not allow for more than one MSTID and to take into account the fact that the slant correction M_0 term introduces a multiplicative distortion.

All of above-mentioned techniques gave unsatisfactory results.

The approach that we propose is based on both the Atomic Decomposition of signals (Chen, Donoho, and Saunders, 2001) and the LASSO (Tibshirani, 1996), which allows for extracting a sparse signal representation from highly overcomplete dictionaries. Each atom of the dictionary represents a possible MSTID. Note that although both of the approaches are equivalent, the former emphasizes the structure of the dictionary, while the later the estimation aspects of the problem.

The approach consists of the decomposition of a signal in the span over an overdetermined dictionary, and introducing a penalty in the norm of the weights of the span to obtain a sparse solution. The formal specification of the method is described

in detail in Section 1.6.2. The loss function consists of a mean-square reconstruction error term and a regularization term on the norm of the parameters.

The reconstruction of the observation from a sparse linear combination of the elements of the dictionary can be expressed as a convex optimization problem, where the sparseness on the solution is achieved by the regularization term. The amplitudes of the elements of the dictionary will be mostly zero, except the weights $\alpha_{i,j}$ of the atoms (see Equation 1.5) that best approximate the value of the detrended VTEC at the pierce points.

The dictionary does not need to be composed of orthogonal elements, but can be any arbitrary set of elements, in particular, a set of elements that is adapted to the problem at hand. The atomic decomposition has several additional properties that are useful, namely: a) in addition to dealing with Gaussian noise, one can also deal with noise of other origins that might introduce a large distortion on some of the samples (see Section 1.6.6), b) allows for a natural way of dealing with the nonuniform sampling process, and c) provides an objective criterion for determining the number of MSTIDs. The formal model of the MSTIDs (i.e., the parametric description) is presented in Section 1.6, Equations 1.6 and 1.8.

1.6 Construction of the Dictionary and Estimation Criteria

In this section, we will primarily present: a) the model of the MSTID, and the design of the dictionary (see subsection 1.6.1), b) the definition of the loss function and regularization criteria (see subsection 1.6.2), and c) the method that computes the sparse decomposition and implementation aspects (see subsection 1.6.4).

The dictionary is designed from a model that assumes that the pierce point observations $V(x, y)$ at epoch t, can be expressed as a linear combination of several MSTID waves $T_i(x, y)$, as in Equation 1.6. The parameters α_i for epoch t are estimated from the reconstruction error only at the set of pierce points $I_{x,y}$. Thus, for a map containing M MSTIDs we have,

$$V(x, y) = \sum_{i=0}^{M} \alpha_i T_i(x, y) + n(x, y) \tag{1.6}$$

The coordinates x and y are coordinates on the map, (note that although the model is for the whole region, only the IPP coordinates are used in the estimation process), the dictionary atom $T_i(x, y)$ models the wavefront snapshot of one MSTID wave at epoch t. The term $n(x, y)$ is an additive random noise, and α_i is the parameter to be estimated, which represents the amplitude of the i^{th} MSTID.

We will define the vector of amplitudes at epoch t, as: $\alpha_t = [\alpha_1, \alpha_2, \alpha_3, ..., \alpha_N]$, where N is the size of the dictionary. The number M of MSTIDs is much smaller than the number of elements of the dictionary N.

1.6.1 Dictionary Design

The model consists of the superposition of several planar monochromatic waves from a dictionary of elements $T_i(x, y)$. We will model the MSTID $A(x, y, t)$ as a 2D monochromatic planar wave such as,

$$A\left(x, y, t\right) = A_0 \cos\left(\vec{k} \cdot (x, y) - \omega(t - t_0) + \varphi_0\right) \tag{1.7}$$

where $\vec{k}$ is the 2D angular wave number vector, with the module $\left|\vec{k}\right| = \frac{2\pi}{\lambda}$; λ is the wavelength and the normal vector $\frac{\vec{k}}{\left|\vec{k}\right|} = (\cos\theta, \sin\theta)$ points in the direction of propagation of the wave. The wave amplitude is A_0. The terms ω, t_0 and φ_0 are the angular frequency, the starting epoch and initial phase of the MSTID wave, respectively. The i^{th} dictionary element $T_i(x, y)$ at epoch t is defined as follows:

$$T_i\left(x, y\right) = \cos\left(\frac{2\pi}{\lambda_i}\left(x\cos\theta_i + y\sin\theta_i\right) + \varphi_i\right) \tag{1.8}$$

The element $T_i(x, y)$ of the dictionary is characterized by: λ_i wavelength, φ_i phase, and θ_i wave azimuth. The parameters of each element of the dictionary (θ, λ, and φ), are quantized as real numbers, with values restricted to realistic ranges.

The dictionary D is constructed by the concatenation of the set of N elements $T_i(x, y)$, reshaped as vectors, giving an array, defined as $D = [T_1, T_2, T_3, ..., T_N]$. The elements $T_i(x, y)$ are generated by assigning to the parameters $\{\lambda, \theta, \varphi\}$, all possible feasible values in a quantized range. Each element $T_i(x, y)$ consists of a grid of P_v rows and P_h columns, i.e., a uniform sampling of the geographical region of interest. Then, the array is reshaped to a vector T_i of dimension $P_v \times P_h$. Note that the observations correspond to the IPPs, hence, in the estimation of the vector, α_t will be done only with the coordinates (x, y) corresponding to measured IPPs.

1.6.2 Loss Function and Regularization

Here we will analyze the criterion for estimating the parameters α_t, by means of a trade-off between a loss function (i.e., how well we approximate the observations by means of the model) and a regularization term (i.e., constraints on the possible solutions).

The loss function term implicitly expresses our assumptions about the statistics of the estimation error. We define our loss function as the logarithm of the likelihood function, i.e., the logarithm of the joint probability of the observations given the parameters to be estimated. We assume that the probability of the model depends exponentially on the norm ℓ_p of the difference between the observed values and the values generated by our model. Also we introduce in the model a regularization term which allows for expressing desirable properties of the solution. In our case, as we want sparsity on the solution, we will penalize certain distributions of values of the estimated vector of parameters α_t by means of a norm ℓ_q. Therefore, the general form of the problem to solve can be expressed as:

$$\min_{\alpha_t} \|V - D\alpha_t\|_{\ell_p}, \qquad \text{subject to} \quad \|\alpha_t\|_{\ell_q} < \tau \tag{1.9}$$

Where V consists of the IPP observations, D is the dictionary for reconstructing the observation at the pierce points, α_t is the vector to be estimated at time t, and ℓ_p and ℓ_q define the norms that are applied to each term of the optimization problem. Note that the norm of the reconstruction error ℓ_p is different from the norm ℓ_q of the regularization term. The above expression can be written in the Lagrangian form as:

$$\alpha_t^\star = \arg\min_{\alpha_t} \frac{1}{2}\|V - D\alpha_t\|_{\ell_p} + \rho\|\alpha_t\|_{\ell_q} \tag{1.10}$$

There is a one-to-one correspondence between the parameter τ in (1.9) and ρ in (1.10), see for details in Hastie, Tibshirani, and Friedman (2009). The arguments for selecting the values of each norm are discussed in detail in subsections 1.6.2.1 and 1.6.2.2.

1.6.2.1 Loss Function

The metric ℓ_p in the loss function is equivalent to assuming a particular probability distribution of the reconstruction error in Equation 1.9. In particular, the term $\|V - D\alpha_t\|_{\ell_p}$ can be interpreted as the logarithmic likelihood of an exponential distribution. The metrics that we considered were:

1. $\ell_p = \ell_2$: Assumes a multivariate Gaussian distribution, thus the logarithmic likelihood function is the sum of the squares of reconstruction errors. Note that this criterion penalizes quadratically the error, so sample points where the reconstruction error is significant will have a large impact on the estimation of the parameters α_t. That is, the solution will be very sensitive to values far from the mean.

2. $\ell_p = \ell_1$: Assumes a multivariate Laplacian, thus the logarithmic likelihood function is the sum of the absolute values of the errors on the data. The

key point is that this distribution assumes that important deviations in the reconstruction error are more likely than the case of a Gaussian distribution. Therefore, the penalization is lower, and the impact of large errors in the estimation of the parameters α_t is lower.

3. Huber Loss: This loss is used for robust estimation of parameters, and consists of applying ℓ_2 to reconstruction errors under a threshold and ℓ_1 over the threshold, and therefore inherits the properties of ℓ_1 when dealing with high value reconstruction errors. See Hastie, Tibshirani, and Friedman (2009) chapter 10, for a discussion on the use of this criterion for robust estimation.

For the selection of the norm ℓ_p, we considered the following fact. The solution to the problem posed by Equation 1.9 is especially sensitive to the norm ℓ_p, because of the geometry of the pierce points. This is because as the points are not uniformly distributed over the plane, the IPPs follow a pattern that consists of the projection of the ground stations to the effective height viewed from the satellite. The consequence is a bias in the detection of the directions of the waves imposed by the geography of the network. This bias is a consequence of the elongated distribution of receivers and the regions with the highest density of receivers, which make the outliers dependent on the azimuth of the MSTID.

As a result, the contribution to the reconstruction error of the receivers located on the border of the network will be larger than those in the central part of the network. This is because small errors in the estimation of the propagation azimuths will be enhanced over long distances (i.e., NE and SW extremes). That is, a leverage effect will appear due to the geometry and distribution of the receivers.

If we assume a ℓ_1 penalty for the reconstruction error, the outliers have a lower impact in the estimation compared to the case of ℓ_2. Therefore, as we want an estimator that is sensitive to the small deviations of the estimated angle of the MSTID (i.e., leverage effect), we selected ℓ_2 for the loss function. In this way, a small error in the estimation of the angle will result in a larger contribution to the total error of the IPP located at the extreme points of the network, and therefore will have a high influence in the final estimation. Another aspect of the estimation of the data is that we would like to impose sparsity in the solution by means of the regularization term, in this case, the requirements on the norm are inverted.

1.6.2.2 Regularization Term

The dictionary D is designed to be redundant and with highly correlated elements, in order to detect a specific family of waveforms. We would like to solve the approximation problem summarized in Equation 1.9 using the least number of elements of

the dictionary, i.e., a sparse solution in the space of the parameters α_t. This can be done in principle by means of the pseudo metric ℓ_0, which minimizes the number of elements different from zero regardless from their value. For a discussion about why ℓ_0 is a pseudo metric (see Hastie, Tibshirani, and Wainwright, 2015). The problem to be solved can be stated as follows:

$$\min_{\alpha_t} \|\alpha_t\|_0, \qquad \text{subject to} \quad \|V - D\alpha_t\|_2 \leqslant \varepsilon \tag{1.11}$$

where ε represents the permissible deviation of the representation $D\alpha_t$ from the global IPP measurements of the detrended VTEC map $V(x, y)$. Unfortunately, this problem is not convex and can only be solved by combinatorial methods, which for the number of unknowns in the problem at hand is computationally unfeasible.

In this section, we argue that the most adequate norm for the regularization term is ℓ_1. The objective is to select the smallest subset of uncorrelated elements of the dictionary, while minimizing the reconstruction error on a dictionary of redundant and nonorthogonal elements that spans the space of possible solutions.

The effect of the inequality $\|\alpha_t\|_{\ell_q} < \tau$ is to introduce a priori information on the desired values of the set of parameters α_t. In one case ($q = 1$) the inequality affects the sum of either the absolute value of the terms α_t, which indirectly controls the number of elements different from zero, and in the case ($q = 2$) the inequality effects the sum of square values of the terms α_t, which has as a consequence a simultaneous shrinkage of all the coefficients. The detailed analysis of the use of a regularization term for linear regression can be found in Hastie, Tibshirani, and Friedman (2009) in chapter 3.

The use of $q = 2$ produces solutions where all the coefficients α_t are shrinked uniformly which allows for selecting a specific solution for the case of an undetermined system. This is the case of our problem, where the number of elements of the design of the dictionary D, is higher than the dimensionality of the observation vector. On the other hand solution uses almost all the elements of the dictionary. This is not suited to the problem that we want to solve, which is to determine a small set of different waves, i.e. a few number of elements of the dictionary.

The use of norm ℓ_1, gives rise to sparse solutions in the linear regression (see Hastie, Tibshirani, and Wainwright, 2015, for a geometrical explanation), and under certain situations is a good approximation of the pseudonorm ℓ_0, which explicitly minimizes the number of terms different from zero. The use of norms ℓ_p, with $p < 1$, increases the sparsity, but the resulting problem is not convex any more, and therefore the techniques of convex programming cannot be used. Consequently, for this problem, we will use the ℓ_1 norm as a regularizer on the parameters. Note that in

Section 1.6.7, we introduce an iterative solution using ℓ_1 that indirectly approximates the norm ℓ_p, with $p < 1$, in order to obtain a more sparse solution.

The technique that fulfills all the requirements is the LASSO (see Hastie, Tibshirani, and Wainwright, 2015) which is stated as an optimization problem that minimizes the square of the reconstruction error, with a regularization norm on the weights based on ℓ_1. This is the technique that was selected for the estimation of the MSTIDs.

A related technique, is the elastic net (see Hastie, Tibshirani, and Wainwright, 2015, chapter 4), which is a convex combination of the ℓ_1 and ℓ_2 norms on the regularization term. In contrast to LASSO, this technique assigns non-zero values to correlated elements of the dictionary. But in our case, the dictionary consists of highly correlated atoms, because the elements consist of a fine-grained enumeration of the parameters of the wavefronts. In our preliminary experiments, we found that the elastic net yielded poor performance, therefore it was discarded. On the other hand, the use of only the ℓ_1 norm on the regularization term gives a crisp solution assigning the resources to only clearly distinct elements, which is compatible with our initial hypothesis that there is only a limited number of distinct MSTIDs.

Finally, to solve an ambiguity that might arise in the estimation coefficients α_t, we impose the solution to be in the first quadrant, that is that all the elements of the vector α_t should be positive. This is justified by the interpretation of coefficients α_t as amplitudes for each existing MSTID and by the fact that changing the sign of an element of the vector α_t, that multiplies the elements of the dictionary $T_i(x, y)$ (see Equation 1.8) equals a change in the phase φ_i of 180°.

1.6.3 Redundant Dictionary Design

We propose to model 2D detrended VTEC map $V(x, y, t)$ as a linear combination of several MSTID waves as expressed in section 1.3, but it is not easy to directly decompose this combination of MSTID waves into a linear combination as Eq. 1.6. A first approach is to construct a redundant dictionary D of MSTID waves candidates with all the possible parameters, and next to find the optimal solution from D,

$$D = [T_1, T_2, T_3, ...T_N] \tag{1.12}$$

The solution with the minimum number of elements different from zero, correponds to the use of the ℓ_0 norm, which would give a sparse decomposition into individual MSTID waves from the detrended VTEC map. The problem can be stated as,

$$\min_{\alpha_t} \|\alpha_t\|_0, \qquad \text{subject to} \quad \|V(x, y, t) - D\alpha_t\|_2 \leqslant \varepsilon \tag{1.13}$$

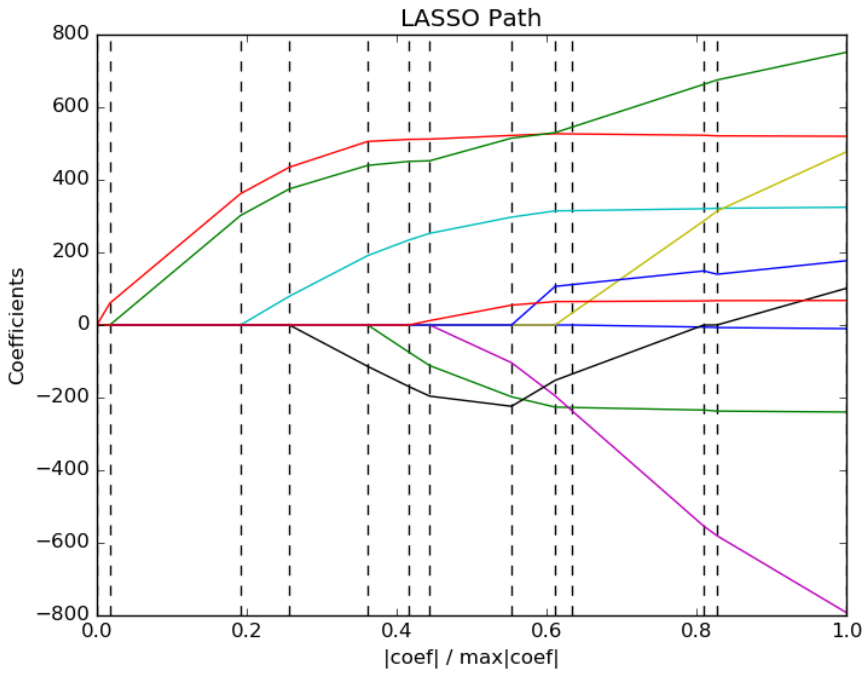

FIGURE 1.4: Example of a LASSO path along the regularization parameter using the Least Angle Regression and Shrinkage (LARS) algorithm. Reproduce from Hastie, Tibshirani, and Wainwright (2015).

where ε stands for the permissible deviation of the representation $D\alpha_t$ from the detrended VTEC map $V(x, y, t)$.

1.6.4 Parameter Estimation, the LASSO Solution

Finally, the components of the MSTIDs are obtained by solving an optimization problem with a term on ℓ_2 for the reconstruction error and a term on ℓ_1 for the regularization term. This can be stated as the following,

$$\hat{\alpha}_t = \arg\min_{\alpha_t} \frac{1}{2}\|V - D\alpha_t\|_2^2 + \rho\|\alpha_t\|_1 \tag{1.14}$$

The sparseness of the solution will depend on an independent parameter ρ which has to be adjusted as explained in Section 1.6.5. Empirically, we have found a low sensitivity of the sparseness with respect to the parameter ρ, since the number of active elements of the dictionary is piecewise constant for wide margins of ρ.

By means of an adequate value of the parameter ρ, (determined for instance by means of cross validation) the Least Angle Regression and Shrinkage (LARS) LASSO gives a good sparse estimation over the redundant dictionary D, see the example of

a LASSO path along the regularization parameter in Figure 1.4. This solution is a very sparse combination of atomic MSTID waves, as follows,

$$V(x,y,t)_{M\times 1} = D_{M\times N}\cdot \hat{\alpha}_{t_{N\times 1}} + \varepsilon \tag{1.15}$$

1.6.5 Two Step Estimation of TID Parameters

The MSTID model presented in Equation 1.8 is characterized by three parameters: $\{\lambda, \theta, \varphi\}$. As the reconstruction error depends on the parameters through trigonometric functions, and a division, this error is more sensitive to some parameters than others. Specifically, the impact of small deviations of the parameters $\{\lambda, \theta\}$ on the final performance is much higher than the case of φ. The method is extremely precise in the estimation of propagation azimuth and wavelength, but the velocity estimation is less accurate, possibly because it is computed from differences of φ at each snapshot. Taking this into consideration, the estimation strategy will have two steps, in the first step, the parameters $\{\lambda, \theta\}$ are estimated using a dictionary fine-grained in the range of these parameters and rough in $\{\varphi\}$. In the second step, the estimation is done with λ and θ fixed to the values of the first step, and the parameter φ will be used to construct a new dictionary with a fine grained range of values.

The first approach for solving the problem (1.14) was based on coordinate descent, as explained in detail in Hastie, Tibshirani, and Wainwright (2015). For our implementation, we have used a method for solving the problem which yields equivalent solutions but is computationally faster. This method is the LARS, see for instance Efron et al. (2004) and Hastie, Tibshirani, and Wainwright (2015). The computational complexity of the LARS algorithm is equivalent to the ordinary least squares estimation which has a complexity of the order $O\left(p^2N\right)$, where p is the number of elements of the dictionary, and N the number of pierce points.

The effect of splitting the estimation into two steps also has an important impact on the computational requirements of the problem. If the granularity (i.e., increments) on the values of each parameter were of n, the size of the dictionary would be $O(n^3)$. By dividing the estimation into two phases, the dictionary of the structure in Equation 1.19 gives a requirement of $O(n^2)$ for the first phase. The resulting nonzero-weight elements of the dictionary of the detected MSTID in the first phase M (where $M \ll N$) reduces the total number of operations on the second phase to $O(Mn)$. The range of values n needs to be adapted to the problem at hand, which depends on the margin of phases, frequencies, and azimuths of the MSTIDs that we want to detect.

1.6.5.1 Step I: Estimation of $\{\lambda, \theta\}$ and the Number of TIDs

For the estimation of $\{\lambda, \theta\}$, we can simplify the dictionary by means of simple trigonometry, the parameter φ of the elements $T_i(x, y)$ of the dictionary (See Equation 1.8) is absorbed by the amplitude of the wave. Thus the element $T_i(x, y)$, for the snapshot t is:

$$\alpha_i T_i(x, y) = \beta_i \cos\left(\frac{2\pi}{\lambda_i}(x \cdot \cos\theta_i + y \cdot \sin\theta_i)\right) + \gamma_i \sin\left(\frac{2\pi}{\lambda_i}(x \cdot \cos\theta_i + y \cdot \sin\theta_i)\right) \tag{1.16}$$

which can be rearranged as two new dictionary elements as,

$$T_{\beta i}(x, y) = \cos\left(\frac{2\pi}{\lambda_i}(x\cos\theta_i + y\sin\theta_i)\right) \tag{1.17}$$

$$T_{\gamma i}(x, y) = \sin\left(\frac{2\pi}{\lambda_i}(x\cos\theta_i + y\sin\theta_i)\right) \tag{1.18}$$

where β_i and γ_i are the amplitudes of the pair orthogonal sinusoidal basis, which satisfy the relationship of $\beta_i = \alpha_i \cos(\varphi_i)$ and $\gamma_i = -\alpha_i \sin(\varphi_i)$. Note the values of β_i and γ_i are used only for deciding the set of elements of the dictionary $T_i(x, y)$ to be used in the following step. And we decided to work with an augmented dictionary, with elements of the form shown in equations 1.17 and 1.18, and estimate the amplitudes β_i and γ_i by means of the LASSO algorithm.

Although the phase φ_i can be obtained from β_i and γ_i, by their ratio and the use of the *arctan* function, this method is extremely unreliable, which justifies postponing the estimation of φ_i for step II. The estimation of φ is done in step II keeping the fixed values λ and θ estimated in step I.

The dictionary D_I for step I has the following structure:

$$D_I = [D_\beta, D_\gamma] = [T_{\beta 1}, T_{\beta 2}, ..., T_{\beta N}, T_{\gamma 1}, T_{\gamma 2}, ..., T_{\gamma N}] \tag{1.19}$$

where $T_{\beta i}$ and $T_{\gamma i}$ denotes the elements of the dictionary defined in Equation 1.17 and Equation 1.18 with the corresponding parameters $\theta_{\beta i}$, $\lambda_{\beta i}$ and $\theta_{\gamma i}$, $\lambda_{\gamma i}$. We denote the vectors of the weights associated with each estimated parameter as: β_t and γ_t. Note that we did not introduce a constraint in the elements of the vectors β_t and γ_t so that they should be non-null simultaneously; we decided to take as candidates of MSTID the union of indices i found in both vectors, to filter the values in step II. That is, some of the candidates to be detected MSTIDs, will be discarded in the second step. The map $V(x, y)$ at epoch t can be expressed as follows,

$$V(x, y) = D_I \cdot [\hat{\beta}_t, \hat{\gamma}_t]^T = D_\beta \cdot \hat{\beta}_t + D_\gamma \cdot \hat{\gamma}_t \tag{1.20}$$

where the vector of coefficients $\hat{\beta}_t$ and $\hat{\gamma}_t$ are estimated by means of the LASSO algorithm. The elements of the dictionary D_I associated with the coefficients $\hat{\beta}_t$ and $\hat{\gamma}_t$ different from zero, determine the wavelengths $\hat{\lambda}_t$ and directions $\hat{\theta}_t$ of each MSTID candidate and are the input for the next step.

The parameter φ_t can can be approximately computed by,

$$\hat{\varphi}_t = -\arctan\frac{\hat{\gamma}_t}{\hat{\beta}_t} \tag{1.21}$$

Nevertheless, we have found that this estimate was extremely unreliable and inconsistent between different snap shots. Note that the solution from LASSO is the approximated decomposition of detrended VTEC map $V(x,y,t)$ with the deviation of $D\cdot[\hat{\beta}_t,\hat{\gamma}_t]$. The method we described above in the text gives a reliable estimation for the parameters of $\hat{\theta}_t$ and $\hat{\lambda}_t$ from the improved dictionary, but a weak estimation for φ_t. In order to improve the reliability of our estimation, we use another LASSO step in order to have a better estimate of φ_t.

1.6.5.2 Step II: Estimation of φ

In step I at epoch t, we detect a set of M possible MSTIDs candidates. We define the parameters of the i^{th} detected MSTID at epoch t as the pair $(\hat{\lambda}_i,\hat{\theta}_i)$, which remains fixed in step II, where we create a new smaller dictionary for estimating the φ_i associated with each pair $(\hat{\lambda}_i,\hat{\theta}_i)$, from a new variable that is more suitable. We will denote it as B and is defined as: $B_{(\hat{\lambda}_i\hat{\theta}_i)j}=\frac{\hat{\lambda}_i}{2\pi}\varphi_{(\hat{\lambda}_i\hat{\theta}_i)j}$ (see Equation 1.22 and 1.23 below). Thus given a pair $(\hat{\lambda}_i,\hat{\theta}_i)$, we create $j=1,2,...,N$ possible values of $B_{(\hat{\lambda}_i\hat{\theta}_i)j}$. An error analysis showed that the expression 1.23 has a lower sensitivity to the estimation error of φ_j than 1.22. Hence, the dictionary is parametrized by $B_{(\hat{\lambda}_i\hat{\theta}_i)j}$.

The structure for the elements j associated with the pair $(\hat{\lambda}_i,\hat{\theta}_i)$ of the dictionary of step II, will be as follows:

$$T_{(\hat{\lambda}_i\hat{\theta}_i)j}(x,y) = \cos\left(\frac{2\pi}{\hat{\lambda}_i}\left(x\cdot\cos\hat{\theta}_i+y\cdot\sin\hat{\theta}_i\right)+\varphi_{(\hat{\lambda}_i\hat{\theta}_i)j}\right) \tag{1.22}$$

$$= \cos\left(\frac{2\pi}{\hat{\lambda}_i}\left(x\cdot\cos\hat{\theta}_i+y\cdot\sin\hat{\theta}_i+B_{(\hat{\lambda}_i\hat{\theta}_i)j}\right)\right) \tag{1.23}$$

with $i=1,2,...,M, j=1,2,...,N$. Each element of the new dictionary will correspond to a given φ, and the structure of the new dictionary, which we will denote as D_{II} is created by concatenation of the dictionaries specific for each MSTID associated with each pair $(\hat{\lambda}_i,\hat{\theta}_i)$ detected in step I. Therefore, the dictionary associated with a given MSTID $D_{\hat{\lambda}_i\hat{\theta}_i}$, will consist of a set of waveforms that characterize the MSTID estimated for fixed values of $\hat{\theta}_i$ and $\hat{\lambda}_i$ and the range of values $B_{(\hat{\lambda}_i\hat{\theta}_i)j}$ related to the

phase φ_j of the waveform.

$$D_{II} = [D_{\hat{\lambda}_1\hat{\theta}_1}, D_{\hat{\lambda}_2\hat{\theta}_2}, ..., D_{\hat{\lambda}_M\hat{\theta}_M}] = [T_{\hat{\lambda}_1\hat{\theta}_1 1}, T_{\hat{\lambda}_1\hat{\theta}_1 2}, ..., T_{\hat{\lambda}_M\hat{\theta}_M N}] \tag{1.24}$$

Thus, if the range of possible values of $B_{(\hat{\lambda}_i\hat{\theta}_i)j}$ is N, the size of the dictionary D_{II} is $M \times N$ (M is the number of candidate MSTIDs from step I).

Note that dividing the estimation into two steps, in addition to solving the estimation uncertainty in φ_j, reduces the computational needs. That is, the combined size of the two dictionaries is $2N^2 + MN$, which is much smaller than the size N^3 needed for simultaneously computing all the parameters. For instance, if the resolution of θ, λ and B are 2°, 2 km and 0.1 km respectively, assuming $M \leq 10$ in each snapshot, the size of the dictionary is $N^3 \approx 10^8$ versus $2N^2 + MN \approx 10^6$. The value of N was variable and depended on the resolution of each variable. Typically the value of N was around 500.

1.6.6 Dealing with Noise and Distortion

The difficulty of estimating the number of MSTIDs and their characteristics from an incomplete and nonuniform sampling is aggravated by the presence of noise that depends on the elevation of each satellite and of distortions due to the geometry. The noise and distortion can be summarized into two categories, which are dealt with differently by the algorithm ADDTID presented in this work.

1.6.6.1 Additive Noise

The term $\frac{1}{2}\|V - D\alpha_t\|_{\ell_2} < \tau$ in the optimization problem allows for small deviations of the order of τ. Note that as the metric is quadratic, the underlying hypothesis is that this additive noise follows a Gaussian distribution.

1.6.6.2 Distortion due to Multiplicative Effects

These are effects that modify subsets of samples, e.g. the inaccuracy in the estimation of the slant factor $\cos\chi(t)$, loss of data from one station, cycle slips, elevation of the satellites, etc. These effects can be dealt with by extending the dictionary by means of a diagonal matrix of the size of the number of samples, that is, adding a diagonal sub-dictionary. This idea was introduced by Wright et al. (2009), to model the effect of occlusions in the context of image processing, and is appropriate for modeling the categories of distortion mentioned above. This diagonal sub-dictionary allows for assigning a specific value to the sampling points that have suffered an extreme degradation, while allowing the set of global dictionary entries that model

the MSTID as plane waves. The structure of the extended dictionary is as follows,

$$D_{M\times(N+M)} = [T_1, T_2, T_3, ...T_N, I_{M\times M}], \tag{1.25}$$

with $I_{M\times M}$ being the diagonal term. Therefore, now the reconstruction of the plane wave model is given by:

$$V(x,y) = \sum_{i=0}^{N} \alpha_i \cdot T_i(x,y) + \sum_{j=0}^{M} \delta_j \cdot I_j(x,y) \tag{1.26}$$

where the diagonal term $I_{M\times M}$ in the dictionary allows for modeling effects on the isolated observations by means of the coefficient δ_j. Note that this coefficient is a dummy variable in the sense that it enters the optimization problem as a variable but is not used. The variables of interest are α_i, i.e., the coefficients of the elements of the dictionary related to the waves that we want to detect.

1.6.7 Improvement: Reweighted LASSO

As mentioned in 1.6.4, the LASSO algorithm allows for the reconstruction of the initial observation vector of pierce points by means of a sparse set of elements of a dictionary. This can be thought of as an approximation of ℓ_0 by means of ℓ_1. Nevertheless, the ℓ_1 solution still allows for similar elements of the dictionary to have weights different from zero. The underlying physical phenomenon consists of a small number of significant MSTIDs with different velocities, azimuths, and wavelengths. To improve the sparseness of the solution, we have implemented a variant that provides a higher degree of sparsity than the original LASSO. This solution is based on iteratively solving the problem stated in Equation 1.14 by reweighting the vector of estimated coefficients α from each intermediate solution. The idea, proposed by Candes, Wakin, and Boyd (2008), uses a diagonal weight matrix W designed to penalize the use of correlated elements of the dictionary in the reconstruction of the observation. The estimation of α for the weighted ℓ_1-ℓ_2 optimization can be stated as,

$$\hat{\alpha} = \arg\min_{\alpha} \frac{1}{2}\|V - D\alpha\|_2^2 + \rho\|W\alpha\|_1 \tag{1.27}$$

where the diagonal of W consists of positive weights w_i (i=1, 2, ..., dim(α)), which redefines the influence of the MSTID wave atoms.

Beyond the similarity with the ℓ_1-ℓ_2 optimization, the weighted ℓ_1-ℓ_2 optimization can be viewed as a convex relaxation of a weighted ℓ_0 minimization problem, which gives qualitatively different estimations, in the sense that the sparsity is enhanced.

$$\min_{\alpha}\|W\alpha\|_0 \qquad \text{subject to} \quad \|V(x,y) - D\alpha\|_2 \leqslant \varepsilon \tag{1.28}$$

Note that the weighted ℓ_0 minimization problem (see Eq. 1.28) has a unique solution based on the unique solution of ℓ_0 problem (see Eq. 1.11). But the solutions are different between original ℓ_1-ℓ_2 optimization (see Eq. 1.14) and re-weighted ℓ_1-ℓ_2 optimization (see Eq. 1.27). Therefore, a set of reasonable weights can improve the atomic decomposition of detrended VTEC map. Candes, Wakin, and Boyd (2008) proposed a method where the weights at each step of the estimation iterations are the inverse of the true atomic MSTID wave magnitude as follows:

$$w_i = \begin{cases} \frac{1}{|\alpha_i|+\varepsilon_w} & \text{, if } \alpha_i \neq 0 \\ \infty & \text{, if } \alpha_i = 0 \end{cases} \tag{1.29}$$

The term $\varepsilon_w > 0$, which typically is slightly smaller than the mean of the elements of $\hat{\alpha}^{(j)}$, ensures that there are no divisions by zero. This normalization forces the solution $\hat{\alpha}^{(j)}$ to concentrate on the indices where w_i is small to prevent a penalization of larger coefficients in the regularization term.

Observe that the weighting term W in Equation 1.27 affects the regularization term, not the reconstruction error term. This rescaling method seeks to achieve the selection of the weights independent of the magnitude of the approximation coefficients $\hat{\alpha}$. An interesting property of this method is that the convergence is fast. We have found empirically, also mentioned in Candes, Wakin, and Boyd (2008), that only two or three iterations are needed for convergence. Although the method introduces a normalization of the α, the relative amplitude of the MSTIDs is preserved.

This reweighted method is based on iteratively increase or decrease the influence of MSTID wave atoms from the estimated solution ℓ_1-ℓ_2 of the previous iteration weighted by the matrix W. Empirically the method converges after a few iterations.

In practice the weighting matrix at step j, $w_i^{(j)}$ is initialized at iteration $j = 0$, and for the other values j as follows,

$$w_i^{(j)} = \begin{cases} 1 & \text{, if } j = 0 \\ \frac{1}{|\hat{\alpha}_i^{(j-1)}|+\varepsilon_w} & \text{, if } j \geq 1 \end{cases} \tag{1.30}$$

The problem stated at equation 1.27, can be re-expressed in order to make use of the software that solves the LASSO problem, with a transformation that consists in a rescaling of the dictionary matrix D, as follows,

$$\hat{\alpha}_w^{(j)} = \arg\min_{\alpha_w} \frac{1}{2}\|V - D(W^{(j)})^{-1}\alpha_w\|_2^2 + \rho\|\alpha_w\|_1 \tag{1.31}$$

where the estimation $\hat{\alpha}^{(j)}$ can be recovered by $\hat{\alpha}^{(j)} = (W^{(j)})^{-1}\hat{\alpha}_w^{(j)}$.

1.6.8 MSTID Detection and Velocity Estimation

For a given snapshot, the solution to Equation 1.14, even if no MSTIDs are present, will always find a set of parameters α_t that minimize the approximation of the detrended VTEC map V in terms of the dictionary D. Therefore, to decide the presence of MSTIDs, we used two criteria, a) continuity of the parameters in a sliding window of 20 snapshots (600 sec) and b) the value of ρ.

The continuity of parameters was decided inside the window of 20 snapshots (i.e., 600 sec) to reduce the rate of false detections. Additionally, this allowed for having enough samples of phase φ for computing the velocity. The continuity criterion consisted of setting the variation of parameters between the snapshots within the following ranges: azimuth $\Delta\theta = \pm 5^\circ$ and wavelength $\Delta\lambda = \pm 10$ km. To decide that a MSTID was present, the length of continuity had to be greater than 600 sec. Thus, the tracking of the MSTID between consecutive snapshots allowed for a slow drift in the parameters with time.

The value of ρ is crucial for making the method work. A property of the LASSO that arises from the use of ℓ_1 in the regularization term of Equation 1.14, is that the number of elements in α_t that are different from zero is constant for a large margin of variation of ρ (see Hastie, Tibshirani, and Wainwright, 2015, chapter 1). Empirically, we have determined that values of ρ in the high margin are associated with the absence of MSTIDs. This was determined by visual inspection of the maps and by a lack of continuity of the parameters of the MSTID. The strategy that we followed for determining the number of distinct MSTIDs, was to solve Equation 1.14 for an initial value that detects no MSTIDs, and reduce the value of ρ iteratively by 0.8 at each step. Once a set of several MSTIDs were determined in a stable subrange of the margin, we applied the reweighting method, that determines an approximation to a ℓ_0 solution, i.e., minimizing explicitly the number of elements different from zero that yield the best approximation (see Section 1.6.7).

The estimation of the velocity is dependent on the continuity tracking of each MSTID, because it is derived from the slope of the phase φ (see Section 1.6.5). Note that the phase φ from each snapshot is in a different horizontal coordinate system, taking the center of mass of the pierce point set as the origin. This center of mass varies from one snapshot to the next (see section 1.3), therefore the phase φ has to be updated by changing into a unified coordinate system. Moreover, the noise estimation of the phase φ translates into higher uncertainty in the estimate of the slope. Also, when the continuity in the tracking is broken, even in small gaps, the error on the estimate

of the slope can be extremely high. Dealing with issues of the increase of the estimation errors and outliers is critical for the correct estimation of the velocity. Thus, the estimate of the velocity is performed from the slope of the phases φ of each MSTID, by means of the regression method that is robust to the presence of outliers, such as the RANdom SAmple Consensus (RANSAC) method (see Fischler and Bolles, 1981). The use of the RANSAC method is key for obtaining good estimates of the velocity.

The details of the implementation and design choices of the algorithm are discussed in Section 1.6.5–1.6.7. The details are important to be able to reproduce the experiments and also to understand some implementation choices that make the method more accurate and less computationally demanding.

1.7 Evaluation of the ADDTID Algorithm on a Simulated Scenario

In this section, we test the performance of the algorithm in a situation, simulated data in a realistic scenario, i.e., GNSS data, which are a superposition of several preset modeled MSTID waves and noise and distortions of different origins. To test the ADDTID algorithm, we simulated three simultaneous MSTIDs at real IPP locations, measured on the 80th day of 2011. The simulation was based on the measurements of the detrended VTEC maps in Hernández-Pajares, Juan, and Sanz (2006) and were generated following the model in Equation 1.8 in Section 1.6.1, using a realistic set of parameters.

1.7.1 MSTID Activities Simulation

TID Waves	Amplitude (TECU)	Wavelength (km)	Velocity (m/s)	Azimuth (deg)
$T_1(x, y)$	0.3	91.58	150.50	76
$T_2(x, y)$	0.6	156.71	90.77	275
$T_3(x, y)$	0.9	254.85	200.21	124

TABLE 1.1: Parameters of the MSTID in the simulated experiment.

The experiment consists of a temporal sequence of the detrended VTEC maps affected by three different MSTID waves which are occurring at the same height (250 km, to make the experiment compatible with the estimate with real data; for justification, see the beginning of section 2.3). The parameters of the three waves are summarized in Table 1.1. The values of the azimuths and amplitudes were selected to generate a pessimistic scenario, i.e. similar azimuths, one of them almost 180° with respect to the others, and a ratio of amplitudes of 1/3 between the main MSTID and the smallest. To simulate the parameter drift as a function of time in the real

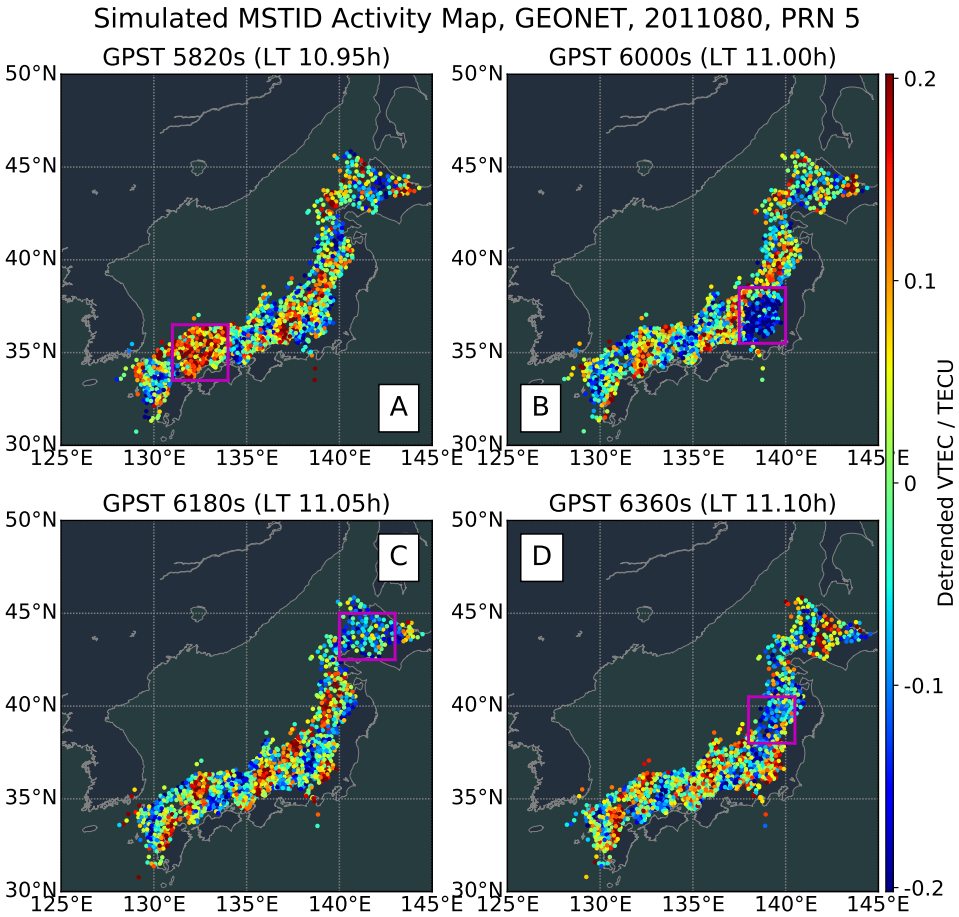

FIGURE 1.5: The simulated MSTIDs activity map in Figures A to D, the IPP locations come from GEONET on the day 80 of 2011, for GPS satellite PRN 5 (four sampling GPS time epochs 5820, 6000, 6180 and 6360 sec). The DC noise regions are marked in magenta.

waves, we fixed an initial value which was perturbed cumulatively by a random percentage at each snapshot, that is, we created Brownian motion of the parameters. This drift percentage was 0.1% for the wavelength, 0.5% for the velocity and 0.5% for the azimuth, and was selected following a subjective criterion of visual similarity between the simulated evolution of the maps and the real maps.

In addition, it should be remarked that the introduction of this drift allows for testing the performance of the system, when the parameters of the MSTID do not correspond exactly to the values of the elements of the dictionary. This last point should be emphasized for two reasons. The first is related with modeling realistic drifts in time in the features of the maps, while the second is related with the methodology. It

is highly improbable that the dictionary will contain parameters that match exactly the parameters of a real MSTID. This methodological aspect is important, because we have checked experimentally that when the parameters of the dictionary coincide with the values of the wave to be estimated, the ambiguity with the value of φ is much lower, which would show unrealistically good performance.

To simulate a multiplicative distortion, which could be related among other reasons to the elevation angle and loss of measurements from one station and cycle slips, we decided to take the most pessimistic approach, which consisted of the substitution of the value at the partial pierce points of a given satellite with Gaussian noise, as shown in Equation 1.32.

Therefore, using the same locations of the measured IPPs $I_{x,y}$ at each epoch t, the time series of the detrended VTEC $V_s(x,y)$ was created as follows,

$$V_s(x,y) = \begin{cases} \sum_{k=1}^{3} T_k(x,y) + n(x,y) & \text{, if } (x,y) \notin R_{x,y} \\ n(x,y) & \text{, if } (x,y) \in R_{x,y} \end{cases} \tag{1.32}$$

where $n(x,y)$ is the random Gaussian noise term set at $SNR = 0$ dB. In addition, 10% of the IPPs of each satellite (set denoted as $R_{x,y}$) is left with no MSTID activity to account for the above mentioned multiplicative distortion. The MSTID activity maps were constructed from the simulated GNSS data $V_s(x,y)$, and the estimation of the number of MSTIDs and the parameters of each MSTID at a given snapshot was done by means of the method presented in Section 1.6.5–1.6.7.

Figure 1.5 shows the snapshots of a simulated set of MSTID activity maps. The simulation is done by selecting observed (i.e. real) IPP positions of GEONET for GPS satellite PRN 5 in Figure 1.2, and over these locations generate the artificial TIDs. The parameters of the simulation are shown in table 1.1 and $SNR = 0$ dB. It consists of three different MSTIDs, with a predominant one. Note the multiplicative distortion, i.e. no MSTID activity, is simulated as the DC noise with randomly shape and location marked with magenta color.

These maps are visually similar real measured scenario compared to Figure 1.2, and at the same time hard in the sense that the azimuths are similar, the difference of amplitudes is significant, the multiplicative distortion is randomly generated, and the power of noise is equal to the sum of the powers of all the MSTIDs.

1.7.2 Detection of Simulated MSTIDs

The resulting scatter plot in polar coordinates (azimuth vs velocity) is shown in Figure 1.6. The simulation spanned a 24 hours period, using real IPPs of all satellites,

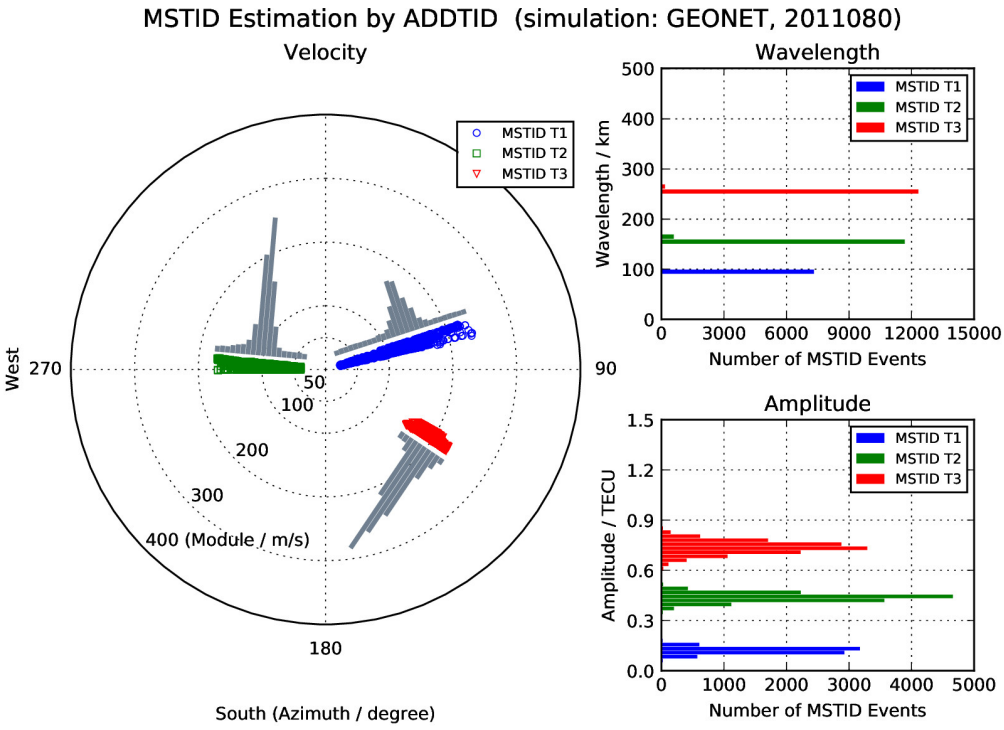

FIGURE 1.6: Polar plot (velocity vs azimuth) of the estimated MSTIDs (left, histogram of the velocity module superimposed on the plot), histograms of the estimated wavelengths (top right) and amplitudes (bottom right), the GNSS observation data were simulated from GEONET, for all the GPS satellite PRNs, on the 80th day of 2011.

i.e., comprising the same IPPs and elevations as the real data. Figure 1.6 shows that three MSTIDs are detected. The value of the azimuth corresponding to each MSTID is estimated almost exactly, nevertheless the velocity estimate has a higher variability. For the simulation we selected a SNR = 0 dB, which explains that the variability of the velocity is higher than that estimated from the real data. This SNR was selected to test the robustness of the method in adverse conditions. Also, the low SNR in the simulation affected all satellites equally, while for the real data, the SNR depends on the elevation of the satellite. In the same Figure 1.6, we present the histogram of the velocities, and the mode of the histograms is near the real value. Note that even though the $T_1(x, y)$ MSTID had the lowest amplitude and the angle was selected so that it was almost 180° with respect to the $T_2(x, y)$, its parameters could be estimated correctly. On the other hand, the estimation of the velocity of $T_3(x, y)$, presented much less variability.

The histograms of the wavelength and amplitude estimations are presented at the right of the same figure. The estimate of the wavelength was as accurate as the estimate of the azimuth. On the other hand, the value of the estimated amplitude

TID Waves	Amplitude (TECU)	Relative Intensity	Simulated Number	Detected Number	Recovery Ratio
$T_1(x, y)$	0.3	8.33%	13337	7432	55.73%
$T_2(x, y)$	0.6	16.67%	13337	12446	93.32%
$T_3(x, y)$	0.9	25.00%	13337	12677	95.05%

TABLE 1.2: Number of detected MSTID events from the simulated scenario.

presented a systematic downwards bias, preserving the relative ranking. This downwards bias on the estimation of the detrended VTEC is due to the regularization term in Equation 1.14, and is inherent to the algorithm. Note that in both cases, the variability of the estimation is small. The number of MSTIDs is determined correctly, in the sense there were no false MSTIDs. The determination of the number of MSTIDs present was conducted using the reweighted LASSO (see Section 1.6.7, for details and justification). The initial estimate of the LASSO gives several candidates that might be very similar, and the process of renormalization combines the candidates that are compatible with the hypothesis of a unique wave. Also, it should be emphasized that the number of MSTIDs to be detected is a free parameter, and the algorithm finds the total number of MSTIDs along with their parameters.

The number statistic of all the detected MSTIDs shown in Table 1.2, indicates that more than 50% MSTIDs can be detected and characterized by ADDTID in spite of about 8.33% of relative intensities in the detrended VTEC maps. In another phase, almost all the MSTIDs ($\geqslant$ 90%) can be correctly recovered if the their relative energies are over 15%.

1.8 Summary

We have presented the Atomic Decomposition Detector of TIDs, ADDTID, a comprehensive multi-TID detection technique, and successfully applied it in the simulated dense GNSS networks.

In next chapter, we will apply ADDTID to study the multi-MSTID characteristics on a spring equinox day of March 21, 2011, from GNSS observation data of GEONET network. As an extended application of ADDTID for detecting different scale TIDs, in particular, Large Scale TIDs (LSTIDs), in Chapter 3, we will study the behaviours of multi-scale TIDs during the US total solar eclipse of 21 August 2017, from another large and dense GNSS observation network of CORS in United States.

Chapter 2

Patterns of MSTIDs Propagation on the Spring Equinox Day of 21 March 2011

2.1 Introduction

In this chapter, we test the performance of the algorithm during the day of the Spring Equinox in Japan. We will describe different phenomena, including a pattern of circular waves compatible in time and space with two possible earthquakes of magnitude 4.6 and 4.9. Note that the ADDTID allows for the automatic detection of phenomena, which afterwards can be checked by the naked eye over the detrended VTEC maps, which was the case of the phenomena shown in this section. We selected for testing the algorithm, the 80th day of 2011 (March 21, the spring equinox day of 2011 in Japan), and collected dual-frequency carrier phase GNSS measurements of that day for all the stations, i.e., GNSS data from GEONET. For comparison purposes, we present as the benchmark, the MSTIDs characterized by a tested technique, the comprehensive GNSS Ionospheric Interferometry (hereinafter cGII, see Hernández-Pajares et al., 2012b). That is, we will describe the estimated MSTID propagation parameters by ADDTID from the same GNSS data, and compare the similarities and differences with cGII. Finally we will discuss findings related to MSTIDs corresponding to the natural events.

2.2 Description of Dual-Frequency Carrier Phase GNSS Observation Data

To test the ADDTID method, we use data from a dense network of receivers for constructing a time series of detrended VTEC maps. The data come from the GEONET

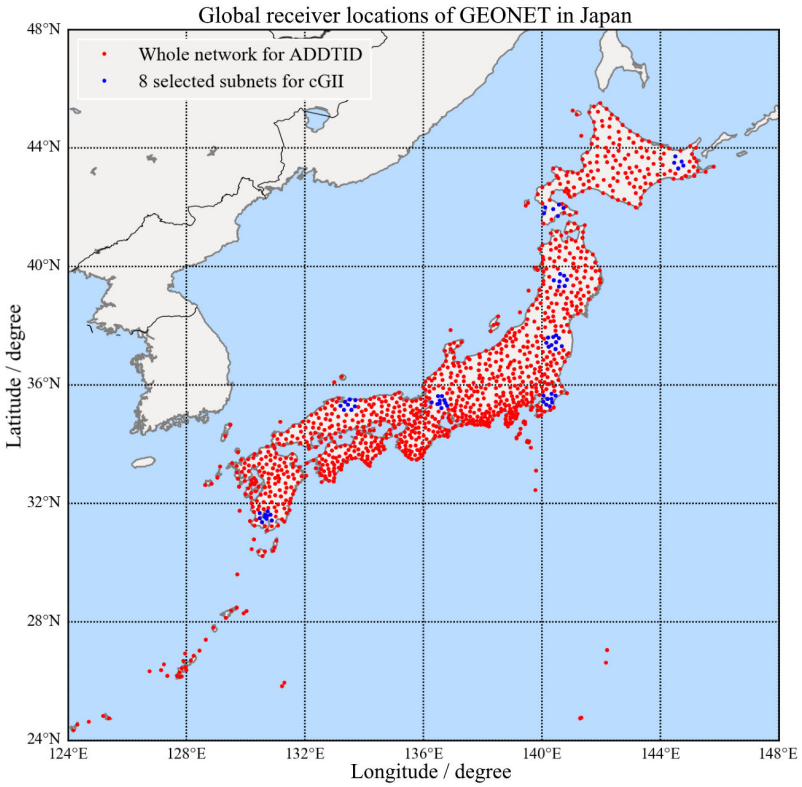

FIGURE 2.1: Distribution of GPS receivers in the Japan GEONET network.

network, which consists of over 1200 GPS stations densely distributed in Japan, see Figure 2.1 and Sagiya (2004).

2.3 Description of Space Weather and Selection of IPP Height

We selected the 80th day of 2011 (i.e., March 21, the first day after the vernal equinox), because it exhibits a rich typology of MSTIDs that might show the frequent winter-like daytime characteristics (Kotake et al., 2007), nighttime propagation excited by solar terminator (Afraimovich et al., 2009), and summer-like propagation in the whole day (Oinats, Kurkin, and Nishitani, 2015).

In principle there were no disturbances originated by phenomena such as significant earthquakes and tsunamis, see the reports of no corresponding ionospheric disturbances in the GEONET-observing region from U.S. NOAA National Centers for Environmental Information (2011b,c). In Figure 2.2, the redundant geomagnetic activity indices on the 80th day of 2011, i.e. the planetary 3-hour-range (Kp), the geomagnetic auroral electrojet (AE) and geomagnetic equatorial disturbance storm

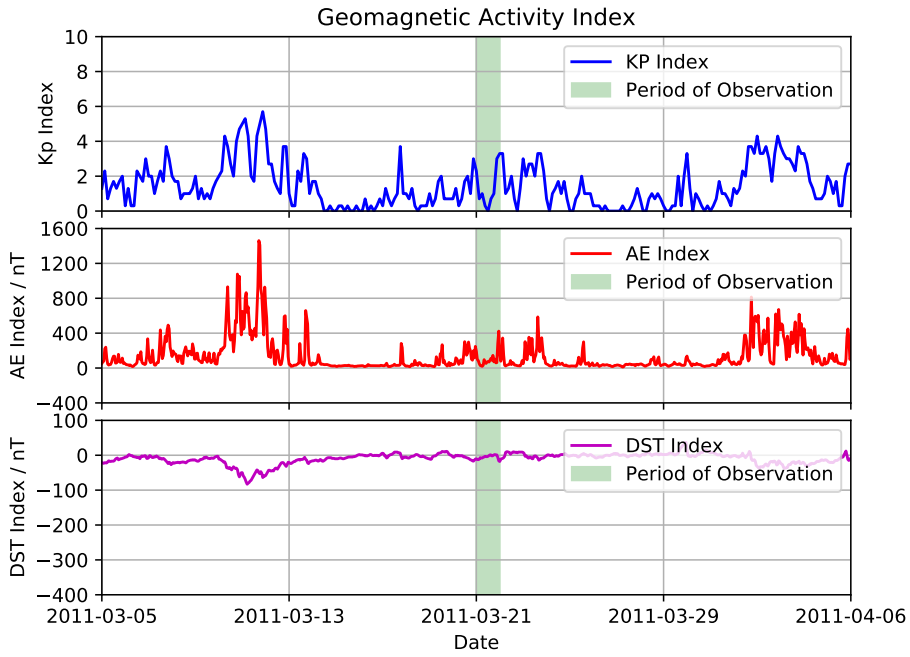

FIGURE 2.2: Geomagnetic Activity Indices, blue line for planetary 3-hour range index (Kp), red line for Geomagnetic Auroral Electrojet (AE) index, magenta line for Geomagnetic Equatorial Disturbance Storm Time (DST) index.

time (DST) indices, indicate that no major geomagnetic storms or strong geomagnetic activities are observed, see U.S. NOAA National Centers for Environmental Information (2011a). Also the indicators of solar activity, the sunspot number and the solar radio flux at 10.7 cm (2800 MHz) in Figure 2.3, shows the quiet solar activity, see U.S. NOAA National Centers for Environmental Information (2011d).

Moreover, Figure 2.4 shows the hourly height distribution of peak electron density (hmF2) on this day was from about 250 km to 350 km. The hmF2 climatic values are provided by the International Reference Ionosphere 2016 model (IRI-2016) (see Bilitza et al., 2017), obtained from U.S. NASA Goddard Space Flight Center (2016). According to Hernández-Pajares, Juan, and Sanz (2006), the maximum MSTID generation occurs at the height below hmF2 because the MSTIDs are generated by the interaction between the neutral and ion particles. We assumed that the most frequent dominant MSTIDs are generated below hmF2, so we took 250 km as the mean effective height of the MSTIDs, which is lower than the average hmF2 of 290 km.

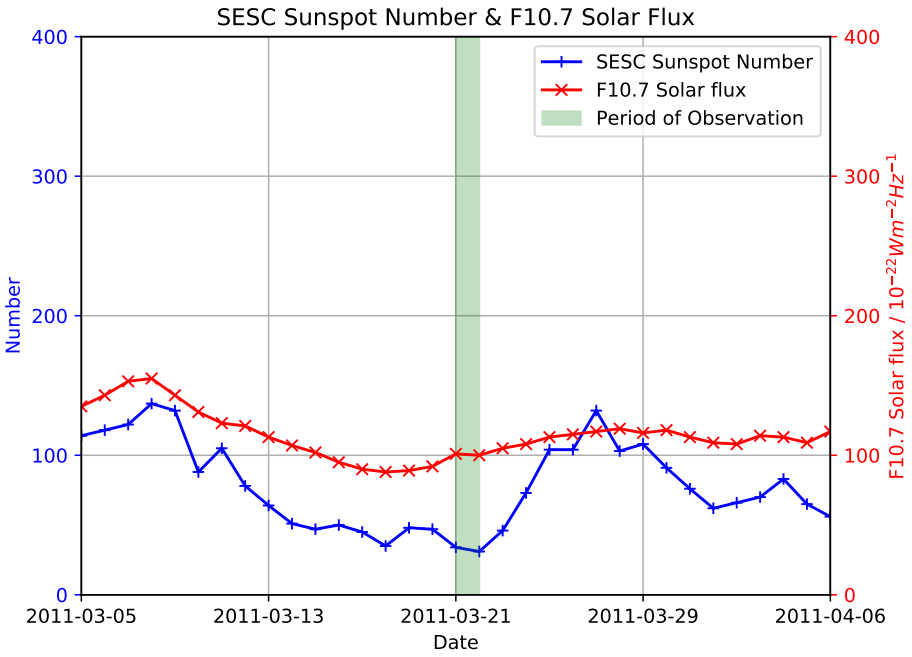

FIGURE 2.3: Observation of Solar Activity Indices, blue line for SESC Sunspot Number, red line for F10.7 Solar Flux index.

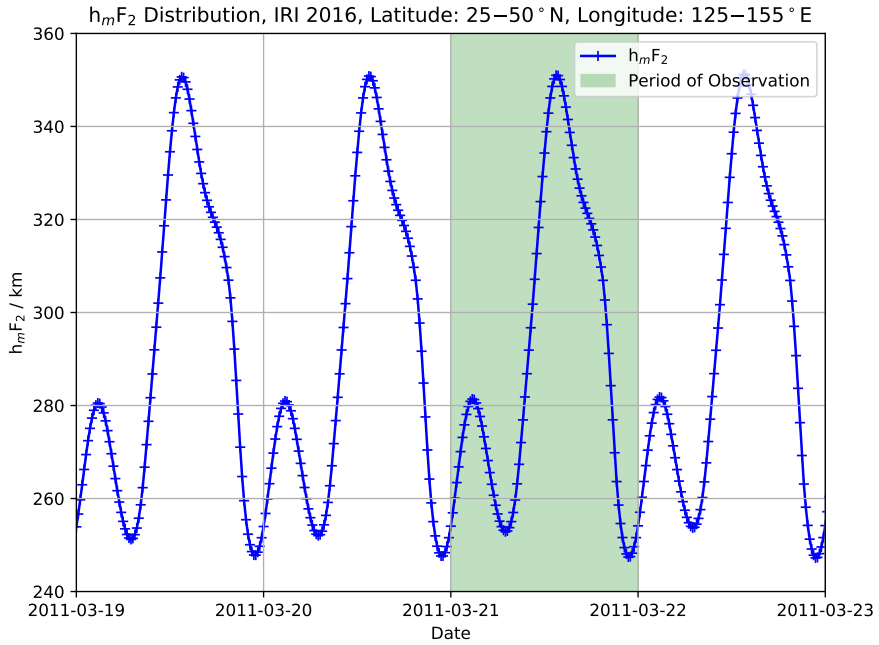

FIGURE 2.4: Climatic hmF2 at the region of 25–55°N & 125–155°E, based the International Reference Ionosphere (IRI) 2016 model.

2.4 Benchmark of MSTID Determination

In this section we use the cGII as the benchmark for detecting and characterizing the MSTIDs, see details of the algorithm introduced in Hernández-Pajares, Juan, and Sanz (2006) and Hernández-Pajares et al. (2012b, 2017).

2.4.1 Introduction of cGII

By means of a local GNSS network consisting of pairs of ground-based GNSS receivers, cGII assumes MSTIDs in form of planar waves propagate across the line-of-sight paths from an assigned receiver (assumed as the reference) to others, see detailed model in Figure 2.5.

In the first phase, cGII estimates the MSTID occurrences by computing the Single Receiver MSTID (SRMTID) index, i.e., the root mean squared of the detrended VTEC for all observable GNSS satellites of the receivers. Secondly, for the determination of the MSTID propagation parameters (i.e. velocity, azimuth, and wavelength), cGII estimates the MSTID propagation delay from the detrended VTEC time series of reference receiver to the given one, by computing the difference between the complex phases of their predominant frequency components. cGII estimates the propagation parameters by means of three typical steps, as follows,

1. VTEC preprocessing: detrending, and frequency spectrum analysis;
2. MSTID propagation delay estimation;
3. MSTID wave parameters computation.

It should be taken into account, that the application of cGII would require a small number but densely distributed receivers in the local GNSS network within the distance between reference and others less than half of typical MSTID wavelength.

2.4.2 MSTID Estimation by cGII

From the output of cGII algorithm, the MSTIDs estimated from a small number of GNSS receivers in a local network, might not be enough to represent the detailed MSTIDs of large regions, i.e. of the order of many hundreds even thousands of kilometers, as is the case of the Japan GEONET network, that we are studying in this chapter. Therefore, eight subsets are selected to estimate the MSTIDs of the whole Japan region, which are widely distributed in the GEONET network, see the blue dots indicated in the map of Figure 2.1.

Figures 2.6–2.9 depict the estimated MSTID azimuth, wavelength, velocity and period respectively, by collecting all the detected MSTID from the eight subnets of

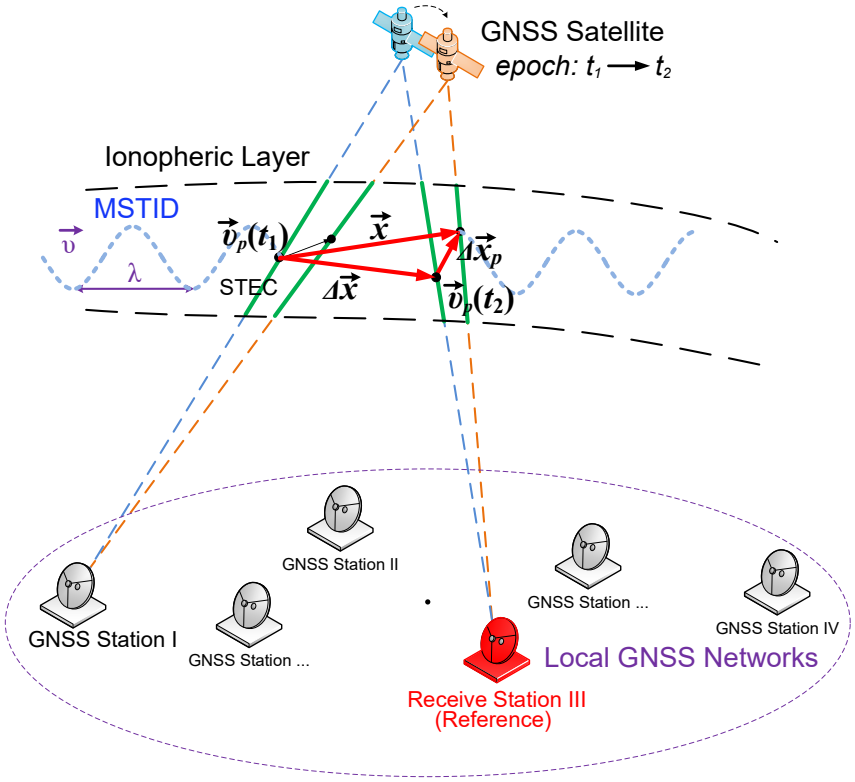

FIGURE 2.5: cGII MSTID detection and characterization model from GNSS receiver network, reproduce from Hernández-Pajares et al. (2017). $\Delta\vec{x}$ is the distance vector between the reference GNSS receiver and other receivers, $\vec{v}_p(t)$ and $\Delta\vec{x}_p$ are the velocity and movement of IPP from epoch t_1 to t_2, respectively.

GNSS network that we have defined. The analysis period encompasses the whole 80th day of 2011. A small number of MSTIDs were detected at nighttime, while the occurrence of MSTID were more frequent during daytime. Figure 2.6 shows the two kinds of MSTIDs with different azimuths at times of the whole day, propagating towards equatorward / equatoreast in the daytime and westward / polewestward in the nighttime. And also Figure 2.7–2.9 indicate that most of the MSTIDs wavelengths, velocity and period of this day are respectively concentrated in the ranges of 125–300 km, 100–300 m/s, and 750–1300 sec. In an alternative way to visualize the results, Figure 2.10 shows the evolution of MSTID propagation parameters by hourly polar plots of velocity vs. azimuth for the whole day. The MSTID intensities presented by the color bar in the figure, indicates that the MSTIDs at the daytime, in particular at the local noon, occurs with the strong activities of the day, whereas a number of MSTIDs with weaker intensity shows at nighttime following a mixed winter-summer MSTID season climatology as it was indicated above. Note that MSTIDs show very few and weak activities during the periods of the morning

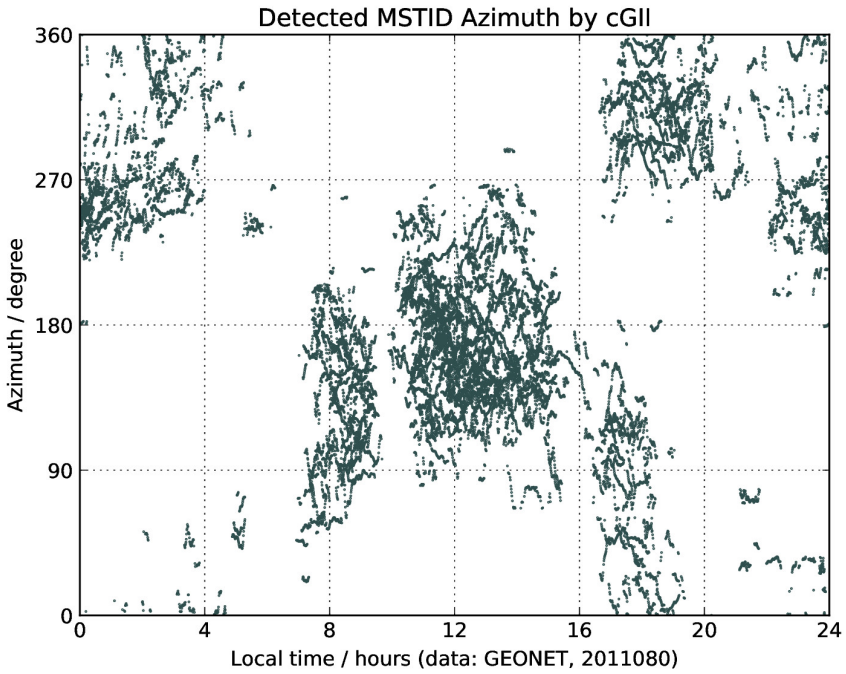

FIGURE 2.6: Time evolution (00:00–24:00 LT) of MSTID azimuths estimated by cGII, from eight subnets of GEONET network, for all GPS satellites, on the 80th day of 2011.

solar terminator (04:00–07:00 LT) and disperse behaviour at the evening solar terminator moment (16:00–19:00 LT).

2.5 MSTID Determination by ADDTID

In this section, we test the method on real GNSS data from the GEONET in Japan, which the same data cGII estimates. In the following sections, applying the ADDTID algorithm, for the March equinox, we present the following results: a) the global description of MSTIDs behaviour and comparison with the benchmark (see subsection 2.5.1), b) the detection and estimation of the parameters of simultaneous MSTIDs at daytime and nighttime (see subsection 2.5.2), c) the detection of several MSTIDs that propagate in the same direction, but with different wavelengths and velocities (see subsection 2.5.3), d) the detection of several MSTIDs that propagate in opposite directions (see subsection 2.5.4), and e) the detection of circular waves (see subsection 2.5.5).

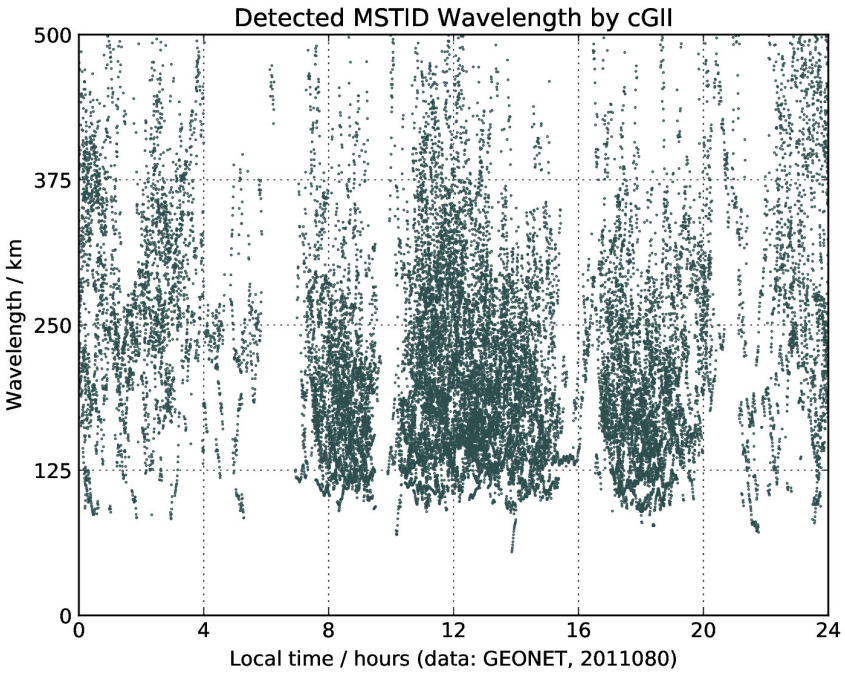

FIGURE 2.7: Time evolution (0:00–24:00 LT) of MSTID wavelengths estimated by cGII, organized as Figure 2.6.

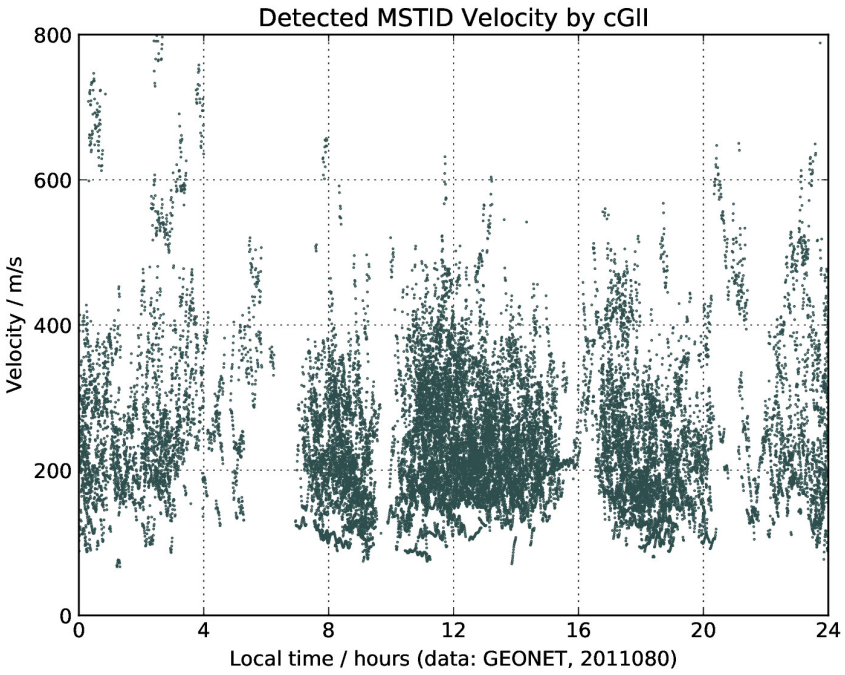

FIGURE 2.8: Time evolution (0:00–24:00 LT) of MSTID velocities estimated by cGII, organized as Figure 2.6.

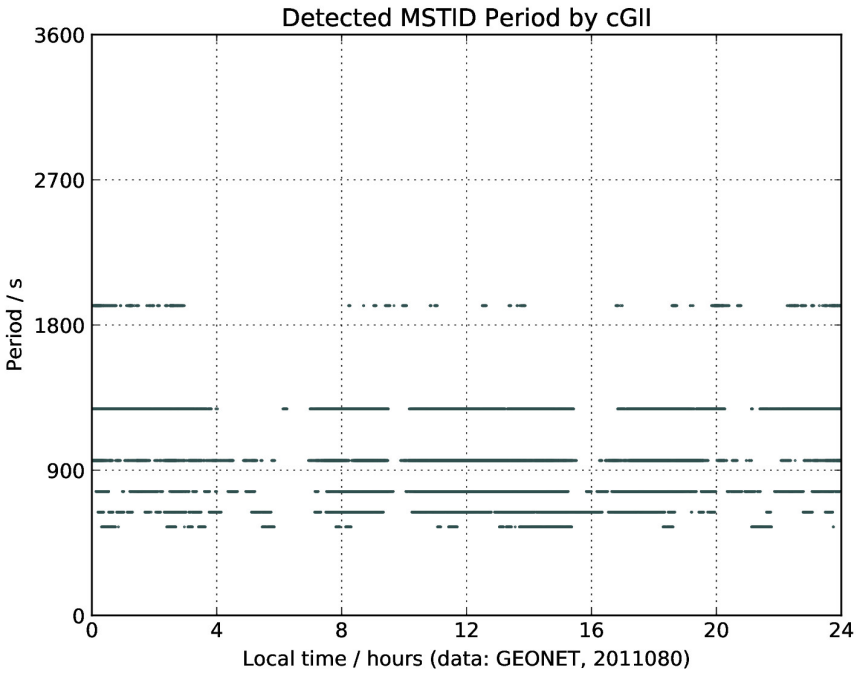

FIGURE 2.9: Time evolution (0:00–24:00 LT) of MSTID periods estimated by cGII, organized as Figure 2.6.

2.5.1 Global Description and Comparison of MSTIDs Behaviour

In this subsection, we present the estimation of MSTID characteristics throughout the day, in intervals of 24 hour, for all the satellites. This scenario is summarized in Figure 2.11, 2.12, 2.13 and 2.14, where we show the time evolution (0:00–24:00 LT) of the MSTID parameters: azimuth, wavelength, velocity and period, estimated by the ADDTID method. Each MSTID is identified by a different color code, and the amplitude is coded by the size of the points (i.e., the larger the size, the higher the amplitude). In Figure 2.13 we show the time evolution of the velocity of each MSTID. The algorithm is able to track the slow changes of the velocity with continuity. Likewise, the period of the MSTIDs shows also a slow continuous change for each individual MSTID, but during nighttime the different MSTIDs show a collective high variability in the range of 500–2,700 sec.

In Figure 2.11 and 2.6 we compare the results of the ADDTID method with the cGII method for the case of the azimuth. Note that the ADDTID method allows the detection of individual MSTIDs by introducing continuity constraints, which greatly reduces the estimation noise. The MSTIDs time series can also be characterized by means of the azimuth vs velocity polar plots at intervals of one hour, as shown in Figures 2.15 (ADDTID) and 2.10 (cGII). The results of both models are consistent in

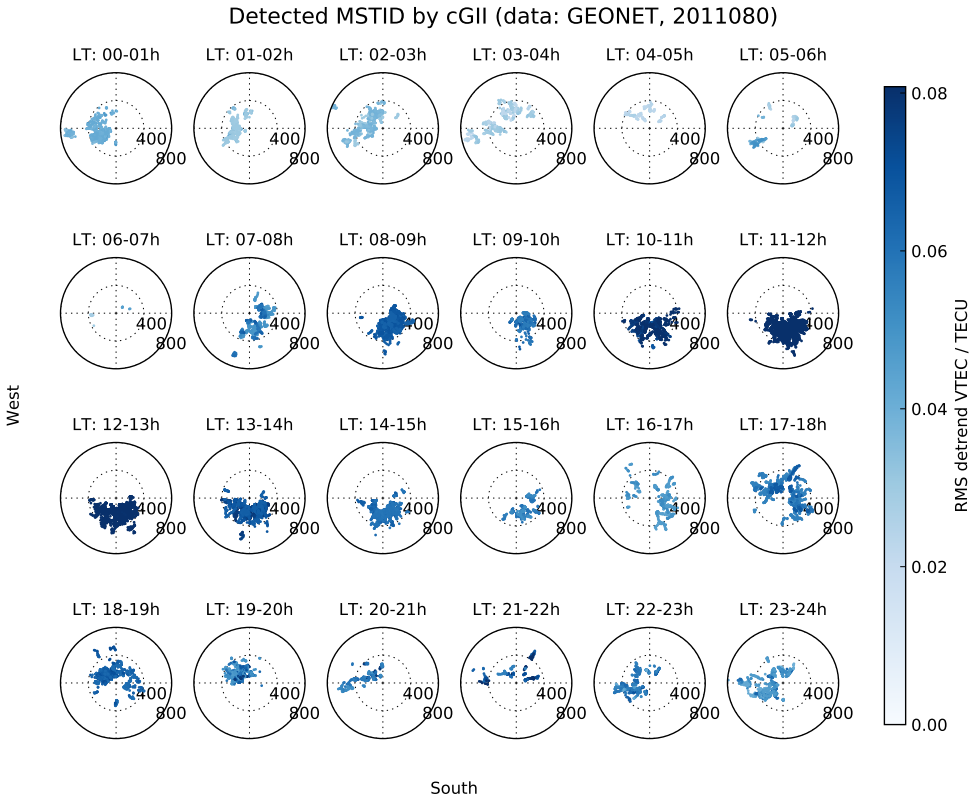

FIGURE 2.10: Intensity polar plots of the MSTIDs, velocities (in m/s) and azimuths (in degree) for the whole day detected by cGII, the color intensity is weighted by the RMS detrended VTEC (in TECUs) from the visible satellites, by local hour, from the GEONET network for all GPS satellites, on 80th day of 2011.

terms of directions and intensities. The main difference was that the ADDTID detects the azimuths of each MSTID with a much lower dispersion, and that MSTIDs with similar azimuths can now be distinguished. A difference between the intensities shown in the figures resides in the fact that the ADDTID estimates individual amplitudes, which are coded by the color intensity of the dots. In the case of cGII, the information related to the intensity of the MSTID is the root mean square of the detrended VTEC of all satellites, i.e., Single Receiver Medium scale Traveling Ionospheric Disturbance (SRMTID) index, see for details in Hernández-Pajares et al. (2012b), which is coded by the color intensity of the dots. The apparent dispersion of velocity seen in the two figures is due to the fact that the velocity of the MSTIDs changes in a continuous way during the time interval corresponding to the plots.

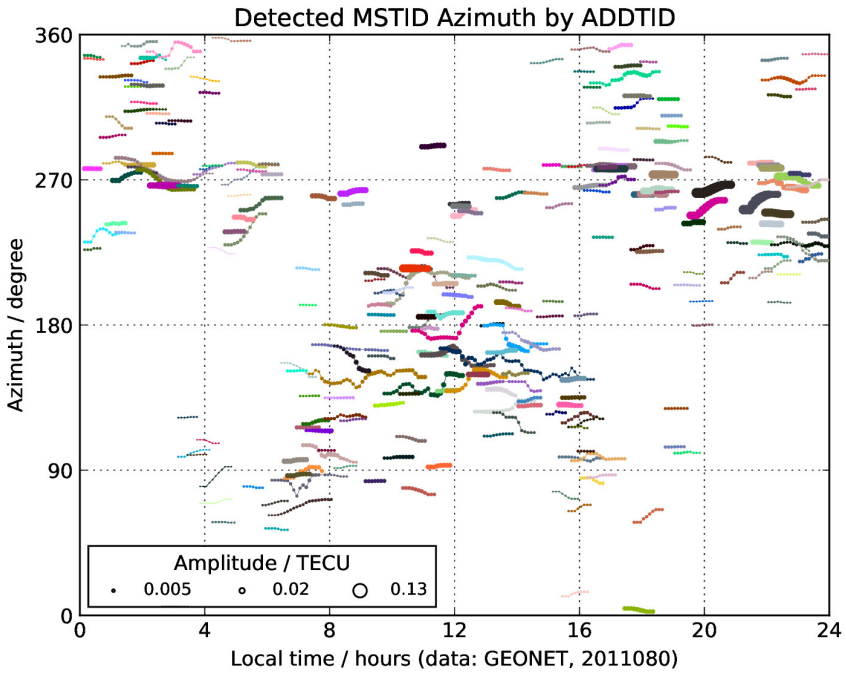

FIGURE 2.11: Time evolution (0:00–24:00 LT) of MSTID azimuths estimated by ADDTID. The individual MSTIDs are color coded and the amplitude is represented by the size of the points, from the GEONET network for all GPS satellites, on the 80th day of 2011.

2.5.2 Characterization of Multiple MSTIDs at Daytime and Nighttime

In this subsection, we present the estimated performance of the ADDTID method at noon, and at midnight for a single satellite. We examine the performance for two periods of the day, namely, between 10:00–12:00 LT (for GPS satellite PRN 5) and 1:00–3:00 LT (for GPS satellite PRN 7). GPS satellite PRN 5 was selected because it presented several simultaneous MSTIDs with similar amplitudes, while GPS satellite PRN 7 was selected to illustrate the case of the detection of simultaneous MSTIDs when one MSTID had an amplitude significantly higher than the other.

By visual inspection, one can see in Figure 1.2, that the maps (at around 11:00 LT for satellite PRN 5), shows the interference pattern of several simultaneous 2D MSTID waves. In these maps, one can measure two dominant MSTIDs that propagate in the equator-east and equator-west directions, with wavelengths of about 135 km and 180 km, and velocities of 150–200 m/s and 200–250 m/s, respectively. The maps in Figure 1.3 shows a predominant MSTID wave that propagates in the northwest direction in nighttime with wavelength between 250–300 km and a velocity between 125–200 m/s.

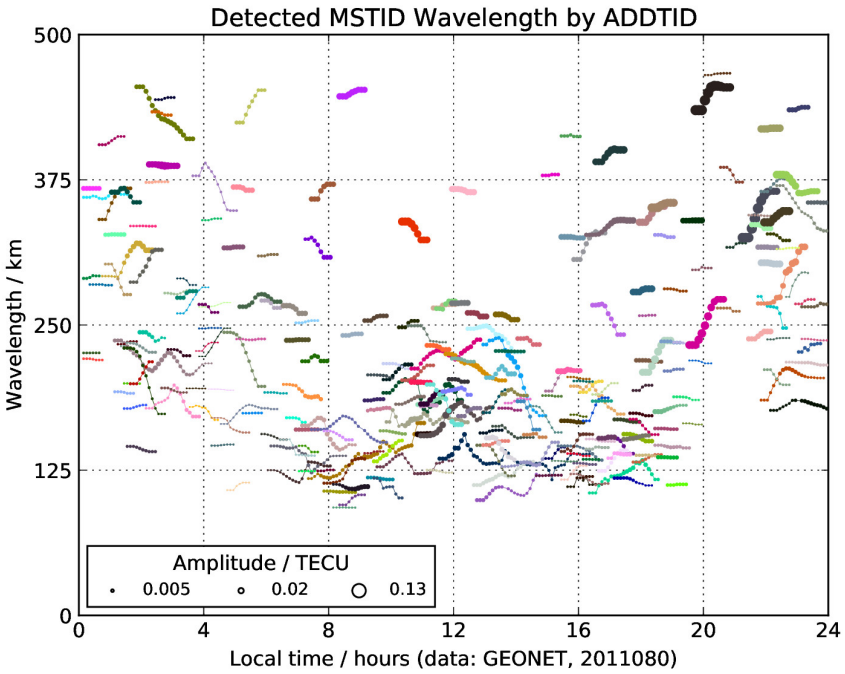

FIGURE 2.12: Time evolution (0:00–24:00 LT) of MSTID wavelengths estimated by ADDTID, organized as Figure 2.11.

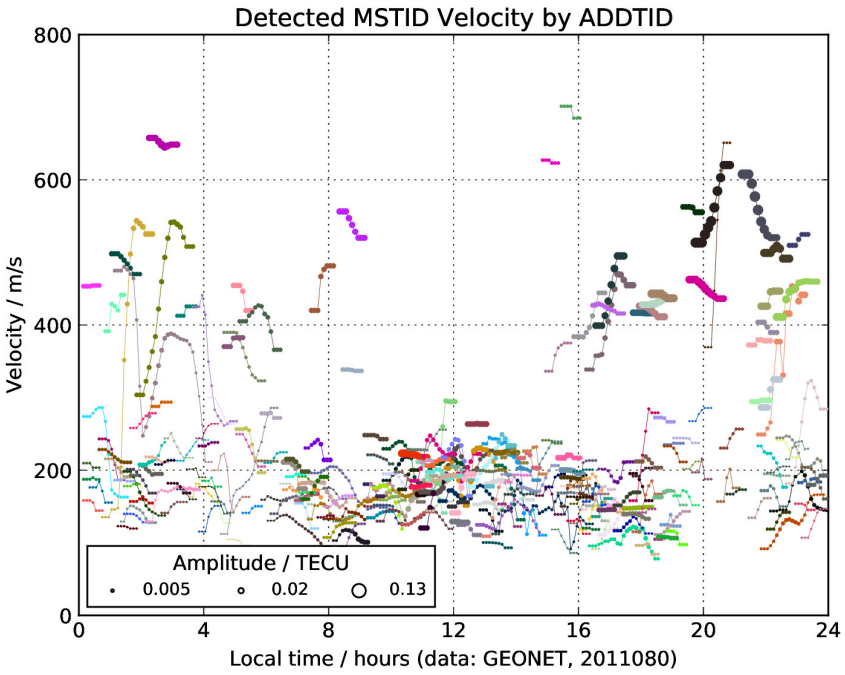

FIGURE 2.13: Time evolution (0:00–24:00 LT) of MSTID velocities estimated by ADDTID, organized as Figure 2.11.

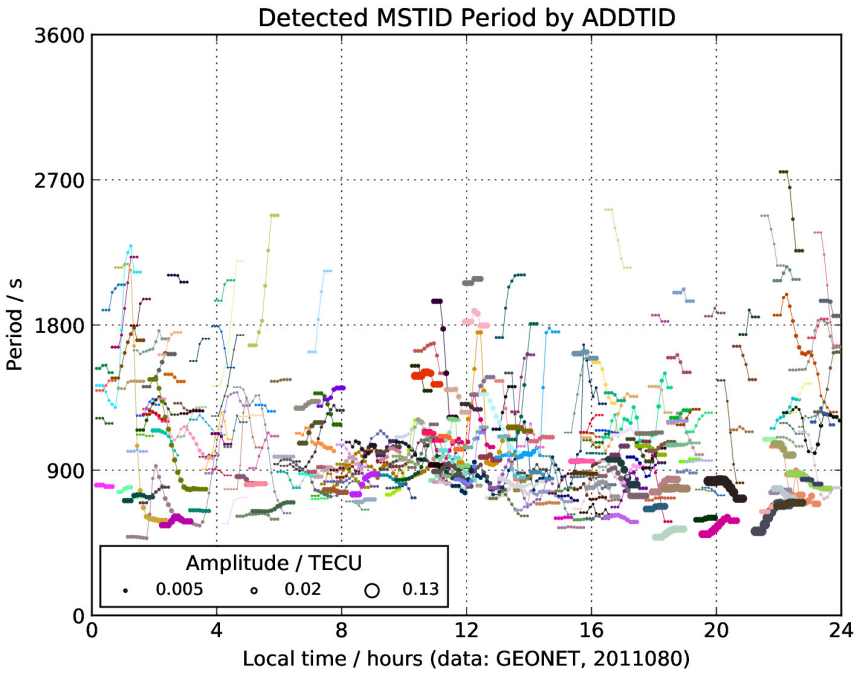

FIGURE 2.14: Time evolution (0:00–24:00 LT) of MSTID periods estimated by ADDTID, organized as Figure 2.11.

In the daytime case, the MSTID waves had similar amplitudes, which gave rise to the interference pattern, but in the nighttime case, at a given time one MSTID had an amplitude significantly higher than the others. The results given by the ADDTID algorithm are compatible with the visual analysis. In Figure 2.16 and 2.17, we show the time evolution of the estimates by means of the ADDTID algorithm of the MSTID parameters for satellite PRN 5 (Figure 2.16) and satellite PRN 7 (Figure 2.17). Each individual MSTID is identified by a color code. Figure 2.16 shows the evolution of several MSTIDs during the time interval from 10:00–12:00 LT. The azimuth time series shows the overlap and continuity of different MSTIDs, having up to three different MSTIDs at different moments. Figure 2.17 shows the evolution at nighttime for satellite PRN 7. The ADDTID algorithm, in addition to detecting the predominant MSTIDs, also detects at times two or three different MSTIDs. The predominant MSTIDs is consistent with the azimuth seen visually at Figure 1.3. Also, note that the algorithm is able to follow drifts in the parameters of the MSTIDs as a function of time.

Discussion: The distribution of the MSTID estimates follow typical daytime and nighttime pattern of the March equinox. During the daytime, especially near local noon (8:00–16:00 LT, see Figures 1.2, 2.11, and 2.15), the ionospheric activity is at the maximum level. More than ten simultaneous MSTIDs were detected by the ADDTID

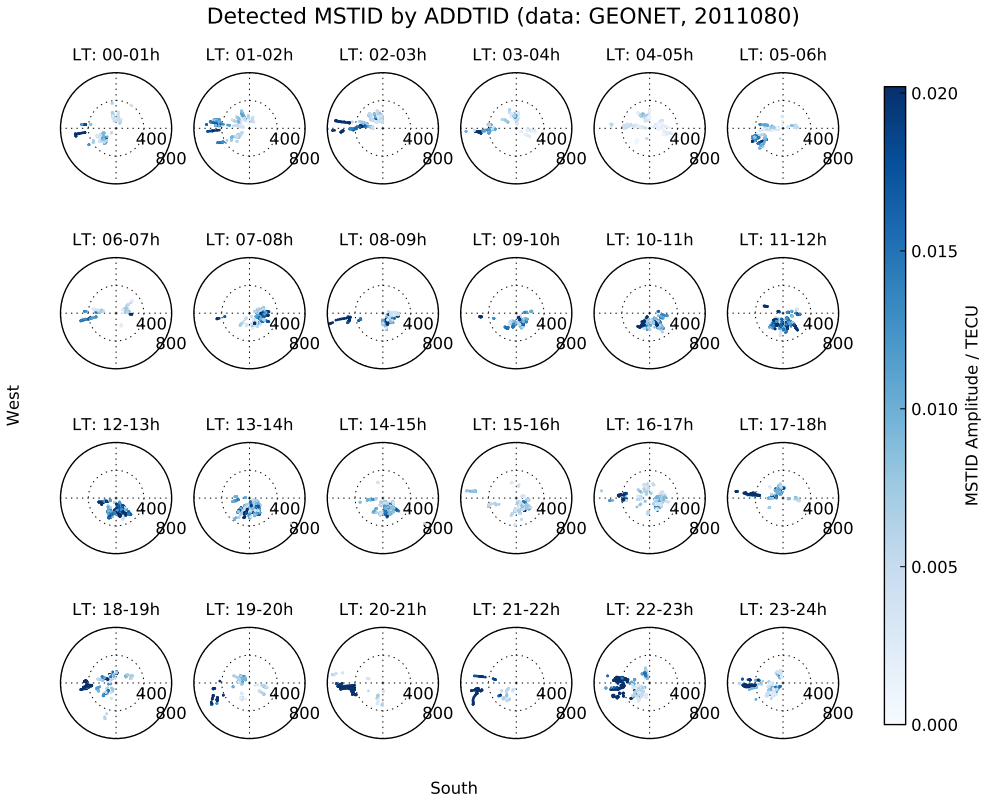

FIGURE 2.15: Intensity polar plots of the MSTIDs, velocities (in m/s) and azimuths (in degree) for the whole day detected by ADDTID, the color intensity is weighted by the MSTID amplitude (in TECUs), by local hour, from the GEONET network for all GPS satellites, on 80th day of 2011.

method. These MSTIDs presented amplitudes in the range of 0.02–0.1 TECU, with azimuth directions from north to the equator/equator-east, velocities in the range from 100 m/s to 300 m/s, the wavelengths in the range of 120–250 km, and periods in the range of 600–2,000 sec. The daytime behaviour of the MSTIDs in the March equinox agree with the daytime MSTID behavior in the winter, as mentioned in Hernández-Pajares et al. (2012b). These similarities are also mentioned in Otsuka et al. (2011) (GEONET) and Kotake et al. (2007) (California GPS network).

In contrast with the daytime, the MSTID activity is weaker and more irregular during the rest of the day. This is due to the smaller overall intensity of the MSTIDs at nighttime and during the morning/evening solar terminator as shown in Figure 2.11. During nighttime (i.e., 00:00–04:00 LT and 20:00–24:00 LT), the amplitudes of the dominant MSTIDs are in the range of 0.005–0.13 TECU. From the features of the distribution of the parameters of the MSTID shown in Figures 2.11–2.14, one

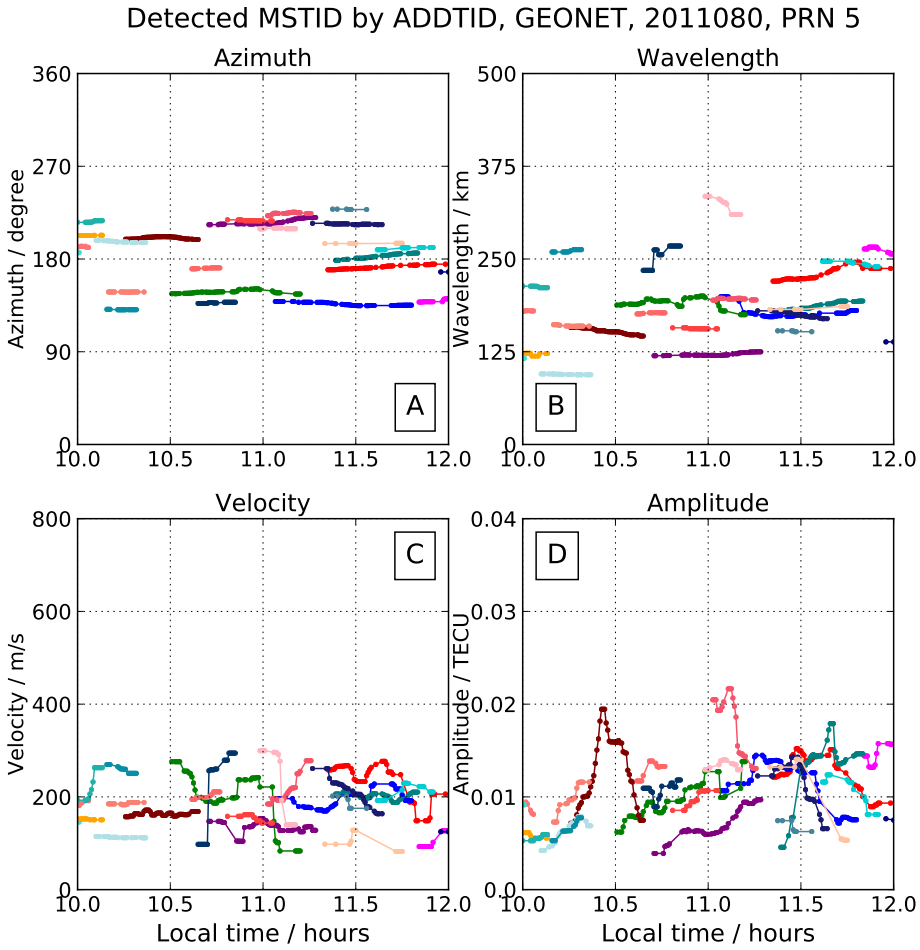

FIGURE 2.16: Time evolution of the MSTID estimates of azimuths, wavelengths, velocities, and amplitudes at local noon and midnight from the GEONET network, for GPS satellite PRN 5, on the 80th day of 2011. Figures A to D show the time evolution of the MSTID estimates at the local noon (10:00–12:00 LT).

can categorize the nighttime MSTIDs into two types: the weak nighttime MSTIDs with amplitude in the range 0.005–0.02 TECU, and the strong nighttime MSTIDs in the range of 0.02–0.13 TECU. The weak nighttime MSTIDs, accounting for 80% of the total estimated nighttime MSTIDs, propagate all westward direction (southwestward/westward/northwestward), with velocities in the range of 100–250 m/s. This is consistent with the nighttime MSTID behaviour in summer (see Hernández-Pajares et al., 2012b). The wavelengths were in the range of 150–450 km and show much higher variability than in summer (50–250 km) of Hernández-Pajares et al.

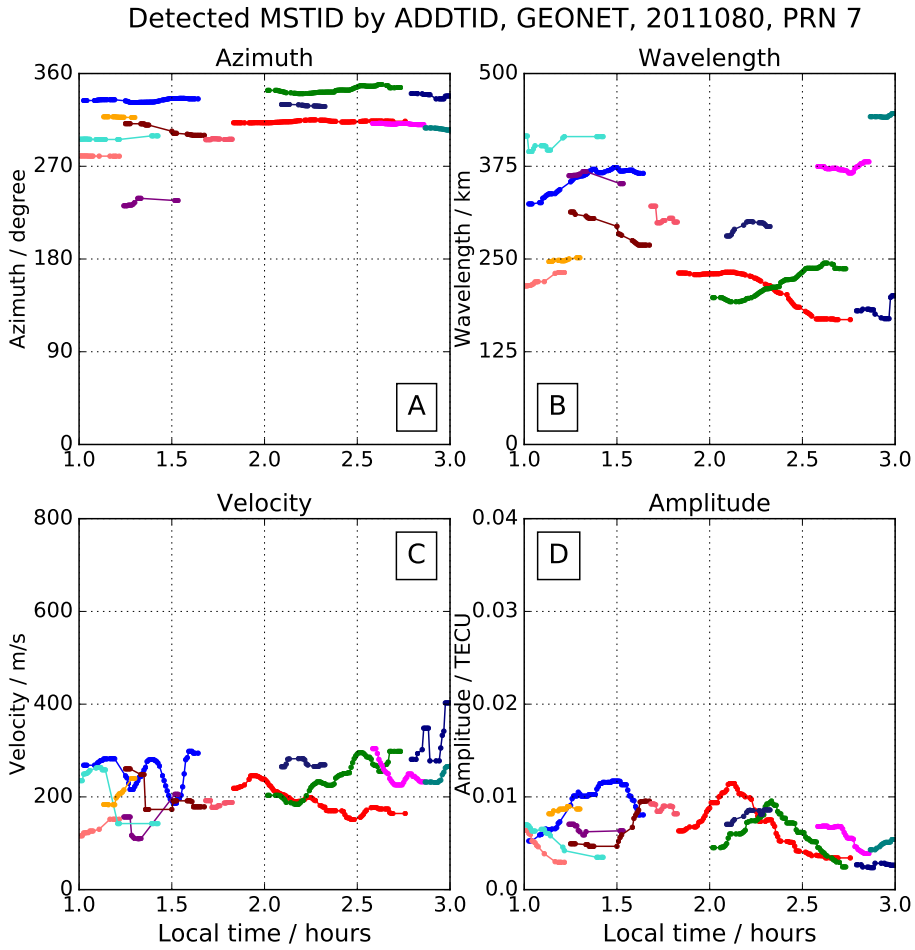

FIGURE 2.17: Time evolution of the MSTID estimates of azimuths, wavelengths, velocities, and amplitudes at local noon and midnight from the GEONET network, for GPS satellite PRN 7, on the 80th day of 2011. Figures A to D show the time evolution of the MSTID estimates at the local midnight (1:00–3:00 LT).

(2012b). The range of the estimated wavelengths are consistent with the range 150–500 km in winter/summer as mention by Tsugawa et al. (2007b). The characteristics of weak nighttime MSTID propagation is compatible with the case study of nighttime MSTIDs in equinoxes for midlatitude mentioned in Oinats, Kurkin, and Nishitani (2015) and Otsuka et al. (2011). The above mentioned properties are summarized in the detrended VTEC maps in Figure 1.3 and in the estimates as shown in Figures 2.11–2.14 and 2.15 (see Hernández-Pajares et al., 2012b).

The strong nighttime MSTIDs have higher velocities and shorter periods than their weaker counterparts. The strong nighttime MSTIDs have a higher amplitude up

to 0.13 TECU. The wavelengths have a much higher mean and dispersion, and the velocities present in the range of 400–600 m/s as it can be seen in Figures 2.11–2.14. This feature of the velocity component appears in the results of both methods, ADDTID and cGII. See for instance Figures 2.15 and 2.10. Figure 2.19 shows the time interval between 20:00–21:00 LT, where two MSTIDs are found with velocities over 400 m/s. This range of velocities is compatible with Deng et al. (2013), where they report a fast MSTID in the local morning (about 8:00 LT) propagating from east to west across Germany with a velocity of about 700 m/s, a period of 420 sec, and a wavelength of 302 km.

During the morning and evening solar terminators (04:00–08:00 and 16:00–20:00 LT), the MSTIDs occur simultaneously in both directions (equator-eastward and westward, respectively), as shown in Figures 2.11–2.14. During the morning terminator, the westward MSTIDs are weaker while the MSTIDs towards equator-east are stronger. The evening pattern shows the opposite behavior. These features are also mentioned by Kotake et al. (2007) and Otsuka et al. (2011) for dominant MSTIDs propagation during the morning/evening solar terminator introduced in the California GPS network. The explanation is the MSTIDs of the morning/evening solar terminator propagate in the direction contrary to the direction of the neutral winds, which always blow from day-side to the night-side. Another compatible observation of the equinox MSTIDs (see Afraimovich et al., 2009) are of magneto-hydrodynamic (MHD) nature and are produced immediately after evening solar terminator.

2.5.3 Different MSTIDs Propagation in Almost Identical Azimuths

Figure 2.18 shows the presence of two different MSTIDs with the same azimuth and different wavelengths and velocities. In order to show more clearly the superposition of both waves, we projected the detrended VTEC in the direction given by the estimated azimuth, which is plotted in purple superimposed on the figure.

Discussion: Both MSTIDs (20:00–21:00 LT) propagate in the west / equator-west direction, with a similar velocity of about 500 m/s but with wavelengths of about 450 km and 250 km. From these figures, one can see that the dominant MSTID marked by red color has a wavelength of about 450 km. The resulting projected waveform follows the form of the superposition of two sinusoids of different amplitudes (One is up to 0.06 TECU and the other is up to 0.09 TECU). Note also that the amplitude plot indicates that the MSTID associated with the longer wavelength was the dominant MSTID, which is compatible with the projected waveform and visually corresponds to the sum of a large amplitude, long wavelength sinusoid with that of a lower amplitude, shorter wavelength sinusoid. Note these two MSTIDs were found from the examination of the time series given by the ADDTID method (i.e.,

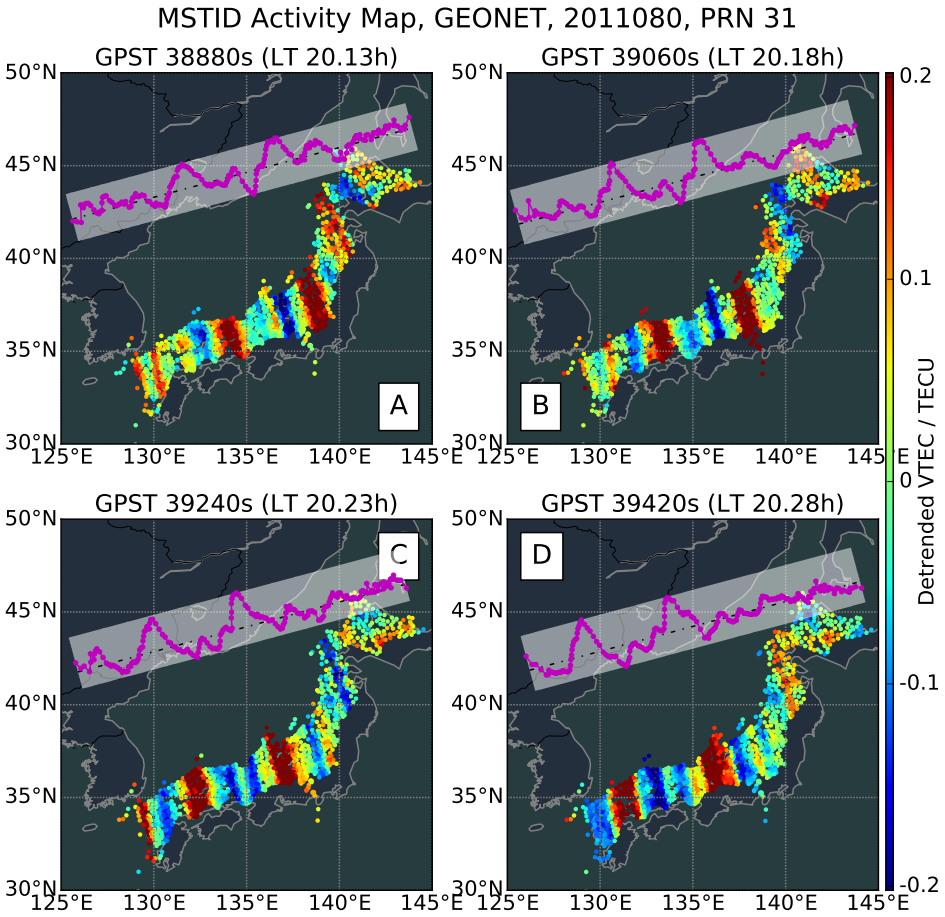

FIGURE 2.18: Two MSTIDs with different wavelengths that propagate in almost identical azimuths at nighttime, from GEONET network, for GPS satellite PRN 31, on the 80th day of 2011. Figures A to D show two MSTID propagations of different wavelengths, as detrended VTEC maps along with the detrended VTEC projection onto the propagation azimuth coded in purple (in TECUs). At nighttime, 20:08–20:17 LT, for four snapshots at GPS time 38880, 39060, 39240 and 39420 sec.

see Figure 2.19). The detection of this type of phenomena can be automated using simple rules on the temporal evolution of the parameters.

2.5.4 Different MSTIDs Propagation in Almost Opposite Azimuths

Figure 2.20 and 2.21 show the event where two MSTIDs propagate in opposite azimuths and are characterized by distinct parameters. The two wavefronts moving

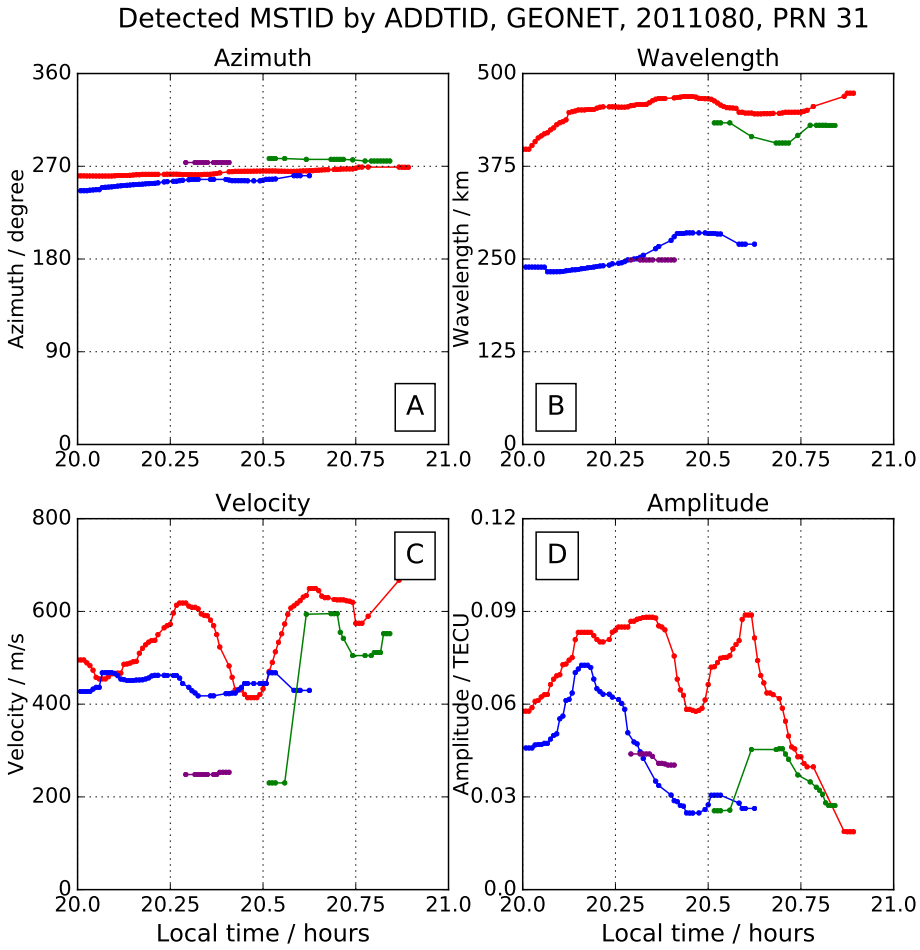

FIGURE 2.19: Two MSTIDs with different wavelengths that propagate in almost identical azimuths at nighttime, from GEONET network, for GPS satellite PRN 31, on the 80th day of 2011. Figures A to D show the corresponding time evolution of the two MSTIDs at nighttime (20:00–21:00 LT) by azimuth, wavelength, velocity, and amplitude.

oppositely appear just before the morning solar terminator (about 5:00 LT) and can be clearly observed from the detrended VTEC maps (Figure 2.20).

Discussion: These two MSTIDs with similar amplitudes about 0.005 TECU are observed before the morning solar terminator (4:30–5:30 LT). The first MSTID propagates in the northeast direction and is located at the northeast corner of the map. This MSTID can be distinguished because it consists of a narrow wavefront occurring with a wavelength of about 140 km. The second MSTID can be distinguished

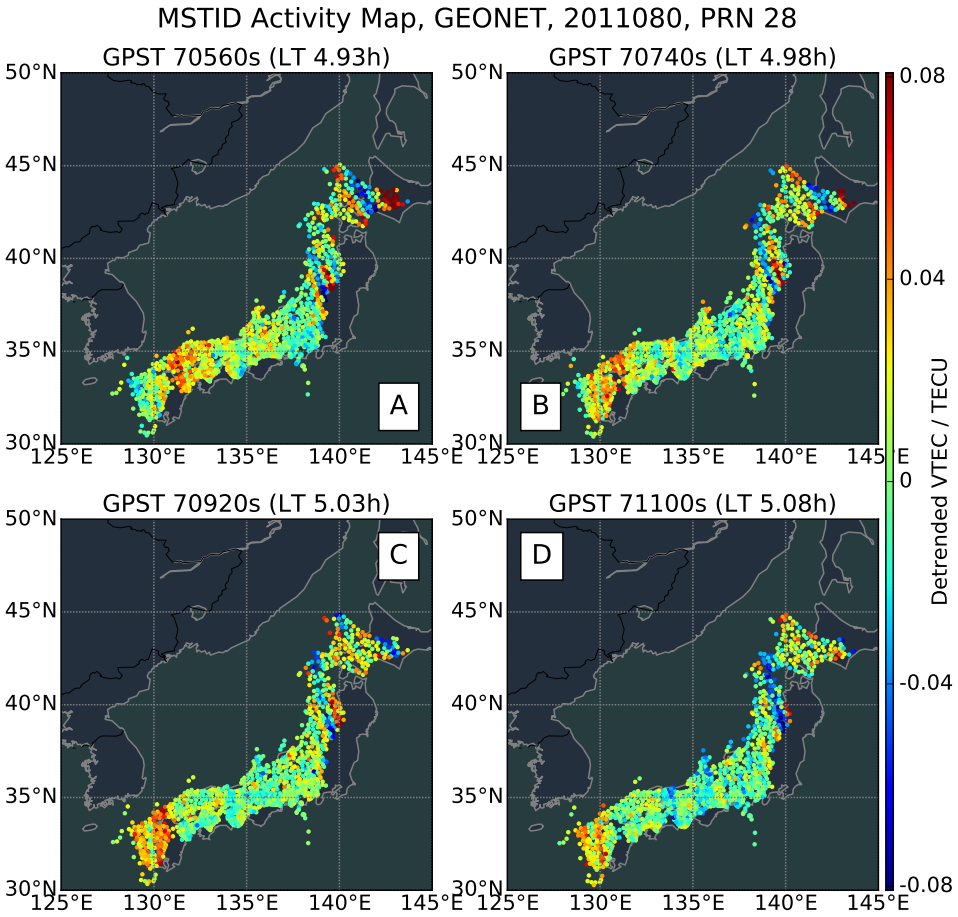

FIGURE 2.20: Two MSTIDs propagate in almost opposite directions during the morning solar terminator about 5:00 LT, from GEONET network, for GPS satellite PRN 28, on the 80th day of 2011. Figures A to D show the propagation pattern of two MSTIDs with opposite azimuth as detrended VTEC maps (in TECUs) at local morning (4:56–5:05 LT), for four snapshots at GPS time 70560, 70740, 70920, and 71100 sec.

because it consists of a flat and wide wavefront that propagates in the west/equator-west direction. This MSTID is in the southwest corner of the map, with a wavelengths of about 200 km. These two MSTIDs were found from the examination of the time series given by the ADDTID method in Figure 2.21, by searching for MSTIDs with azimuth paths separated by 180°, and afterwards confirming the findings on the VTEC maps.

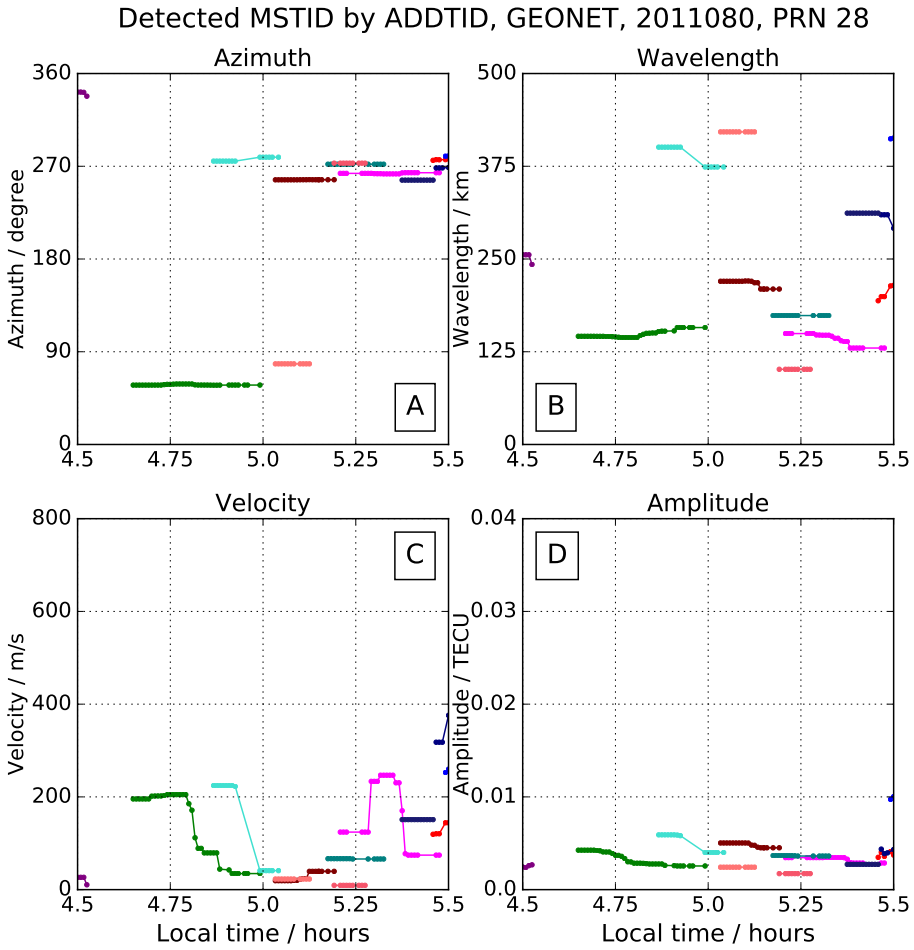

FIGURE 2.21: Two MSTIDs propagate in almost opposite directions during the morning solar terminator about 5:00 LT, from GEONET network, for GPS satellite PRN 28, on the 80th day of 2011. Figures A to D show the corresponding time evolution of the parameters at local morning (4:30–5:30 LT) by azimuth, wavelength, velocity, and amplitude.

2.5.5 Circular Waves on a Day without Special Ionospheric Events

Next, we present the detection of circular waves on a day without special ionospheric events (see explanation at the beginning of Section 2.3). In Figure 2.22, we show the correspondence between the visual appearance of the detrended VTEC maps (Figure 2.22) and the temporal sequence of the estimated parameters (Figure 2.23).

Discussion: Although the algorithm is designed to detect plane waves, by looking at the time evolution of the parameters, we observe that the algorithm detects several

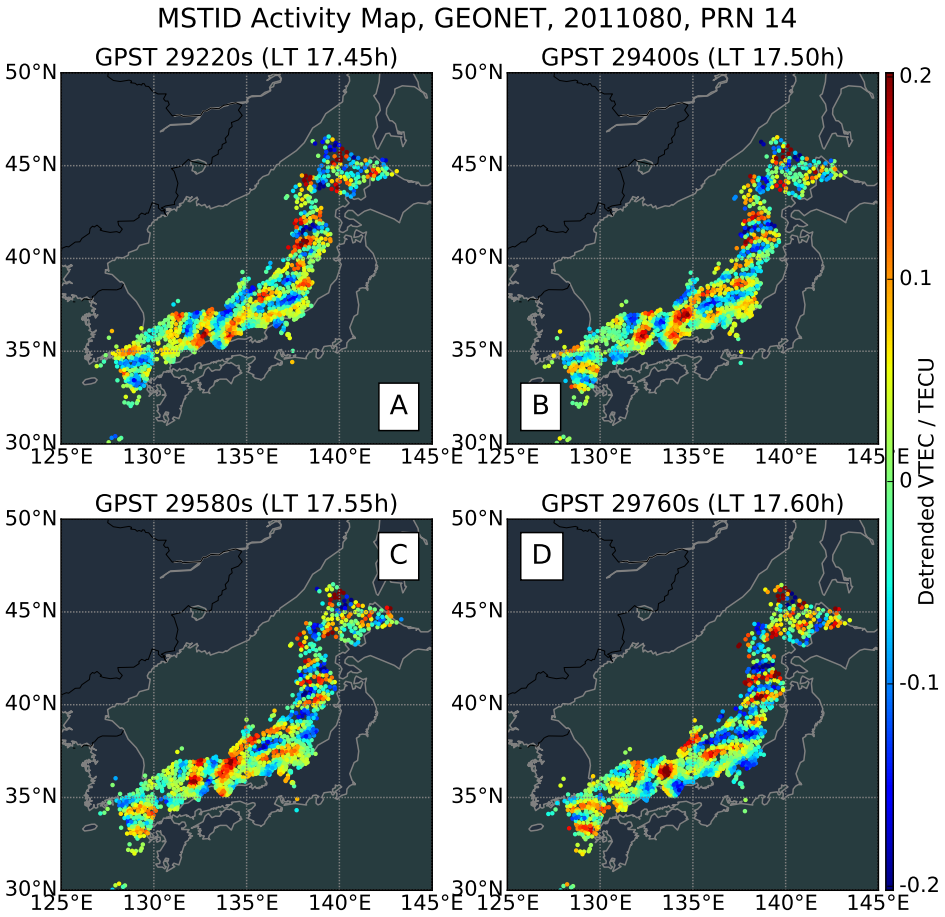

FIGURE 2.22: Circular-like MSTIDs during the evening solar terminator about 17:30 LT, from GEONET network, for GPS satellite PRN 14, on the 80th day of 2011. Figures A to D show circular MSTID in the detrended VTEC maps (in TECUs) at local evening (17:27–17:36 LT), for four snapshots at GPS time 29220, 29400, 29580 and 29760 sec.

MSTIDs that have azimuths compatible with the local plane approximations of the waveform of the circular waves observed in Figure 2.22. Previously, circular waves of the ionospheric disturbances have been reported, see Tsugawa et al. (2011), where the circular waves appear locally in the form of planar waves for each set of IPPs of a given GPS satellite. This is consistent with our findings. A manual estimation by means of a ruler on the maps gives results that are almost equal to the parameters shown on Figure 2.23. This estimation is done from the local slope of the waves at different regions of the map at a given time, for instance at 17:30 LT. These local

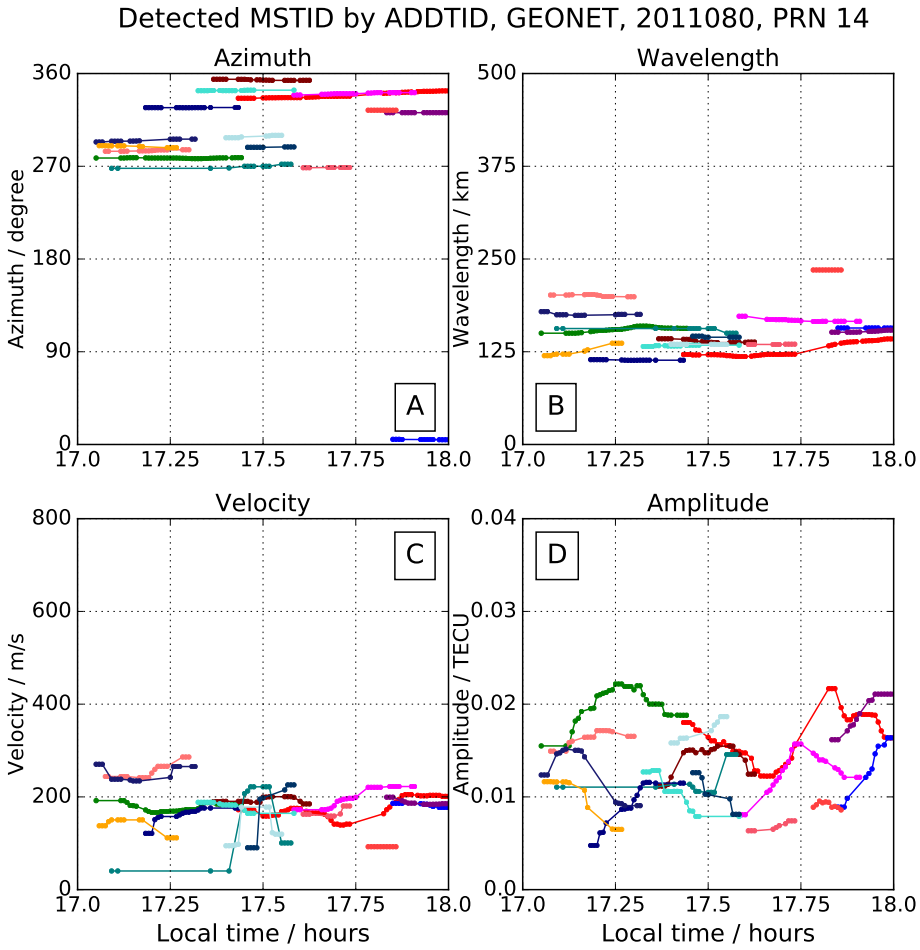

FIGURE 2.23: Circular-like MSTIDs during the evening solar terminator about 17:30 LT, from GEONET network, for GPS satellite PRN 14, on the 80th day of 2011. Figures A to D show the time evolution of the estimated parameters at local evening (17:00–18:00 LT), by azimuth, wavelength, velocity, and amplitude.

approximations to planar waves propagate in the north-west direction, with common values of the other parameters, such as wavelength about 100–200 km, velocity about 120–200 m/s and the period about 1000 sec. Note also the low variability of the wavelengths and velocities associated with each MSTID. In addition, the amplitude of the planar waves alternates, which hints at the fact that they all have almost the same energy. Note that the differences in the values of the wavelength and velocity arise because of the different widths of Japan. The difference in the precision is because in the center, more cycles are measured, while at the north or south there is a lower number of cycles. Note that an automatic detection of the candidates for

circular waves can be done from the temporal evolution of the parameters by means of simple rules.

This finding, obtained thanks to the extreme sensitivity of the new ADDTID technique, might be generated by two earthquakes of magnitude Mw 4.9 and Mw 4.6 in a 3 min interval, recorded at respectively 17:26 LT and 17:29 LT in U.S. Geological Survey (2011a,b). These earthquakes occurred a few hundreds seconds before the detected waves and are compatible with the center of the circular ionospheric wave. A similar precedent of a delay between occurrence of the 2011 Japan Tohoku Earthquake and the circular wave disturbances detected over Japan is reported in Tsugawa et al. (2011). In this case the delay was of about 7 min after the earthquake. The novelty of this finding, regarding previous works performed on major earthquakes (with magnitudes greater than 6), is the detection by the perturbation on the ionosphere despite the relative low magnitude of the earthquake.

2.6 Summary

We have applied the Atomic Decomposition Detector of TIDs (ADDTID), a comprehensive multi-MSTID detection technique in wide and dense networks of GNSS permanent receivers, such as GEONET in Japan. The method that we have presented improves the previous cGII method (see Hernández-Pajares et al., 2012b) in the sense that it can simultaneously detect different MSTID planar waves and estimate their parameters. The new method is compared with the cGII method as a benchmark. The general properties are consistent with results of previous studies, e.g. Hernández-Pajares, Juan, and Sanz (2006), Hernández-Pajares et al. (2012b), Jacobson et al. (1995), Otsuka et al. (2013), and Tsugawa et al. (2007a,b). The main contribution of the method for the study of MSTIDs can be summarized as follows: a) The distribution and tracking of simultaneous MSTID, i.e., temporal variation of the azimuth, velocity, amplitude and wavelength, and the determination of the number of MSTIDs present at a given moment, b) the observation of MSTIDs with velocities much higher than 400–600 m/s during nighttime and the solar terminator, c) the detection of different simultaneous MSTIDs with the same azimuth, or differences of azimuth of 180 degrees, d) the detection of circular waves that are compatible (in time and space) with the occurrence of two consecutive earthquakes of low magnitude, and e) the possibility of creating rules for automatically finding special distributions of the MSTIDs without a visual inspection of the VTEC maps.

In next chapter, we will apply the ADDTID algorithm to study the multi-TID characteristics with different scales, in particular the Large Scale TIDs (LSTIDs), on a total

solar eclipse day of Aug 21, 2017, from another large and dense GNSS observation network in United States.

Chapter 3

Detection and Description of Different TIDs during the Solar Eclipse of 21 August 2017

3.1 Introduction

Solar eclipses provide a unique opportunity to study the ionospheric response to the fast and transitory variation of the solar radiation. The effect of the eclipse is the generation of disturbances with different characteristics and behaviour, caused by the interaction of the heat balance in the shaded regions at different heights. The perturbations can be attributed to different phenomena, which have been described theoretically and experimentally in many studies. Typically, the ionospheric response to the eclipse can be studied by means of various observations techniques, such as the incoherent scatter radar (Salah et al., 1986), radiosonde measurement (Stankov et al., 2017), GNSS ionospheric sounding with double-frequency measurements (Coster et al., 2017), and either with single-frequency data (Hernández-Pajares et al., 2018) among others. Le et al. (2008) and Salah et al. (1986) observe the consistently remarkable depletion of the electron density in F region as a direct consequence of the decreased ionizing radiation in the ionosphere. Chimonas and Hines (1970a) point out that gravity waves generated in middle neutral atmosphere by the eclipse-induced radiative cooling, should build up a bow wave propagating up to E-F region of ionosphere and forming TIDs when the moon's shadow sweeps at supersonic speed. Furthermore, Chimonas (1970), Eckermann et al. (2007), and Fritts and Luo (1993) model and analyse the occurrence, structure and characteristics of the bow wave of atmospheric gravity waves. Cheng, Huang, and Chen (1992), Davis and Da Rosa (1970), and Zerefos et al. (2007) observe the wavelike ionospheric disturbances of atmospheric gravity waves at the D-F1 region during the solar occultation by the moon, but show weak and ambiguous correlations with the bow

wave characteristics due to the difficult observation conditions and the existence of other factors that have a greater influence, such as geomagnetic activity, regular solar terminator, etc. In particular, the large dense ground-based GNSS observation network can be used as global ionospheric sensor network to detect and characterize the time-varying and space-varying electron density fluctuations of the ionosphere. The GNSS observation network in particular can be used to measure the disturbances in the ionosphere generated by the transit of the moon's shadow. Liu et al. (2011b) presented the observations of bow and stern waves in the ionosphere induced by the solar eclipse of 22 July 2009, nevertheless the observations were to a certain extend incomplete because the GNSS network only partially covered the affected region.

In the case of the 2017 solar eclipse, which crossed the United States, the contribution of this work is to provide a detailed characterization of the ionosphere's response to the eclipse's transit. This is due to the fact that the eclipse passed through an area densely covered by the GNSS observation singular network in the United States. As previous works, we can mention, for example, Hernández-Pajares et al. (2018), where the authors show the footprint of TEC decrease in the global TEC map during the eclipse, and in Coster et al. (2017) the authors noted a consistent and significant TEC depletion above US and also the presence of large scale traveling ionospheric disturbances in detail during the eclipse transit. In Zhang et al. (2017) the authors show three different patterns of eclipse-induced ionospheric perturbations and their approximate characteristics such as the bow-shaped TEC depletion along the totality, the clear behaviour of ionospheric bow waves of atmospheric gravity waves and large scale ionospheric waves. In Nayak and Yiğit (2018) the authors show two kinds of traveling ionospheric disturbances of atmospheric gravity waves in different intensities, the stronger ones occurring along the totality and the other in the region with lower eclipse magnitude. Finally, the authors in Sun et al. (2018) describe the occurrence and characteristics of the large scale V-shaped wavefront as a shock wave in F region of the ionosphere. These observations done by means of a dense GNSS network are consistent with the TEC variation prediction by Huba and Drob (2017), the simulation of atmosphere-ionosphere response (see McInerney et al., 2018; Wu et al., 2018) and the ionosphere observations by other techniques such as Bullett and Mabie (2018) and Reinisch et al. (2018). This indicates the ability of ground-based dense GNSS networks to accurately detect eclipse-induced disturbances.

In the above mentioned literature, most of the authors analysed the disturbances created by the eclipse based on maps by means of visual inspection. In contrast, in this work we will use an algorithm that automatically detects TIDs from a large number of measurements from a GNSS network. These measures include observable fluctuations along the lines at all heights of the ionosphere. Also the bow-shaped gravitational waves. In particular, in this work, we will compare each of the estimated

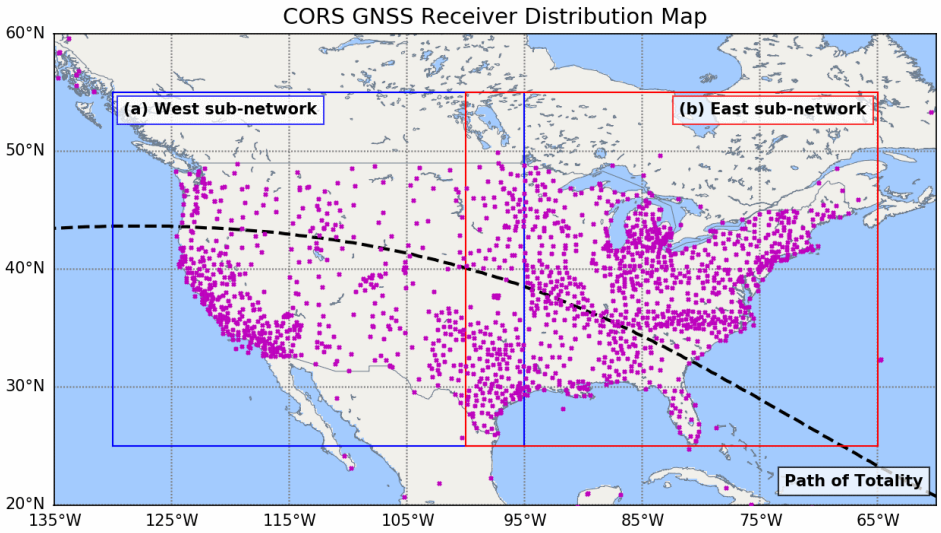

FIGURE 3.1: GNSS receivers distribution of CORS in United States and the path of totality for the solar eclipse in August 2017. Magenta dots denote the location of the GNSS receivers, the black dashed line the path of totality, the blue rectangular frame the West sub-network of CORS and the red the East subnetwork.

disturbances by means of the ADDTID algorithm with a visual representations of the maps where the associated phenomenon is observed.

In summary, the contribution of this work will be the temporal characterization of the ionospheric disturbances associated with the eclipse of 21 August 2017, by means of an algorithm capable of quickly detecting the temporal variation of the characteristics of multiple simultaneous TIDs. For this, we have used the ADDTID algorithm (see details of the theoretical background and implementation in Yang, Monte-Moreno, and Hernández-Pajares, 2017), which detects several simultaneous TIDs and yields the changes in wavelength, azimuth and velocity of each wave as a time series.

3.2 Observation Data and Space Weather

In order to describe the effects of the eclipse on the ionosphere above the United States, we used data from GNSS receivers. The source of the GNSS data is provided by the Continuously Operating Reference Stations (CORS) network of the National Geodetic Survey (NGS). This network consists of almost 2000 ground-based continuous GNSS stations densely distributed in the United States, see Figure 3.1 and Snay and Soler (2008).

During the duration of the eclipse, the geomagnetic activity was very weak (the planetary 3-hour-range indices $Kp \leq 3$, see Figure 3.2, U.S. NOAA National Centers

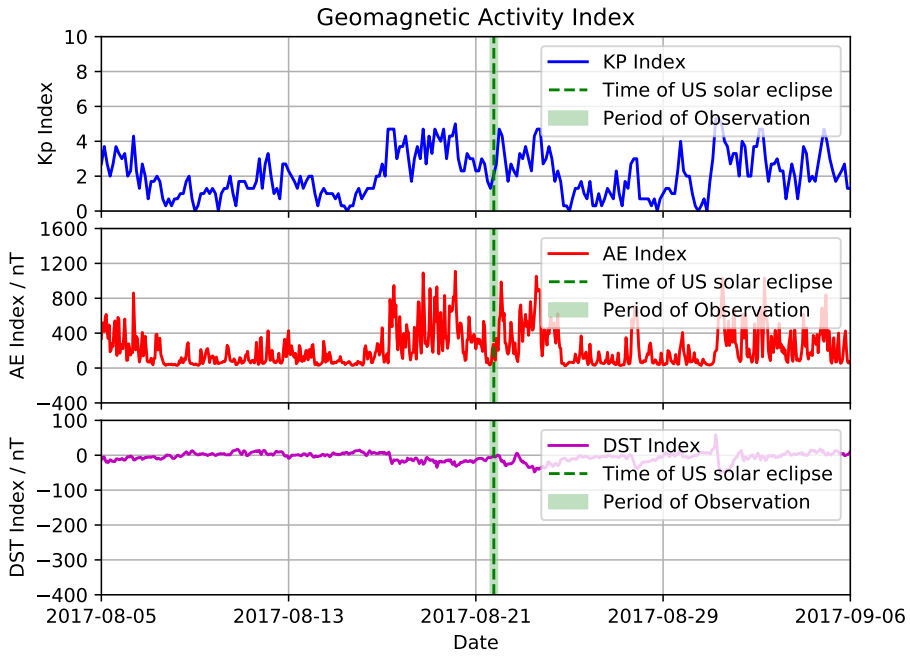

FIGURE 3.2: Geomagnetic Activity Indices, blue line for planetary 3-hour range index (Kp), red line for Geomagnetic AE index, magenta line for Geomagnetic Equatorial DST index.

for Environmental Information, 2017a), the auroral electrojet activity was moderate (the AE index $\leq$500 nT, see Figure 3.2, Japan World Data Center for Geomagnetism, 2018), and the quiet solar activities recorded in Figure 3.3, see U.S. NOAA National Centers for Environmental Information (2017d). Also there were no significant disturbances originated by natural hazard phenomena such as significant earthquakes or tsunamis, that is, no corresponding ionospheric disturbances in the CORS observing region recorded in U.S. NOAA National Centers for Environmental Information (2017b,c).

3.3 Preliminary Analysis of GNSS Ionospheric Perturbation

In this section, we present a first analysis of the ionospheric perturbations during the solar eclipse. The section is structured in two parts: (a) The GNSS data preprocessing, where we present a summary the method for obtaining the ionospheric combination from the dual frequency carrier phase data, and the detrended TEC data to construct the detrended VTEC maps (Section 3.3.1); and (b) the global overview of ionospheric disturbances by means of visual inspection of the maps (Section 3.3.2).

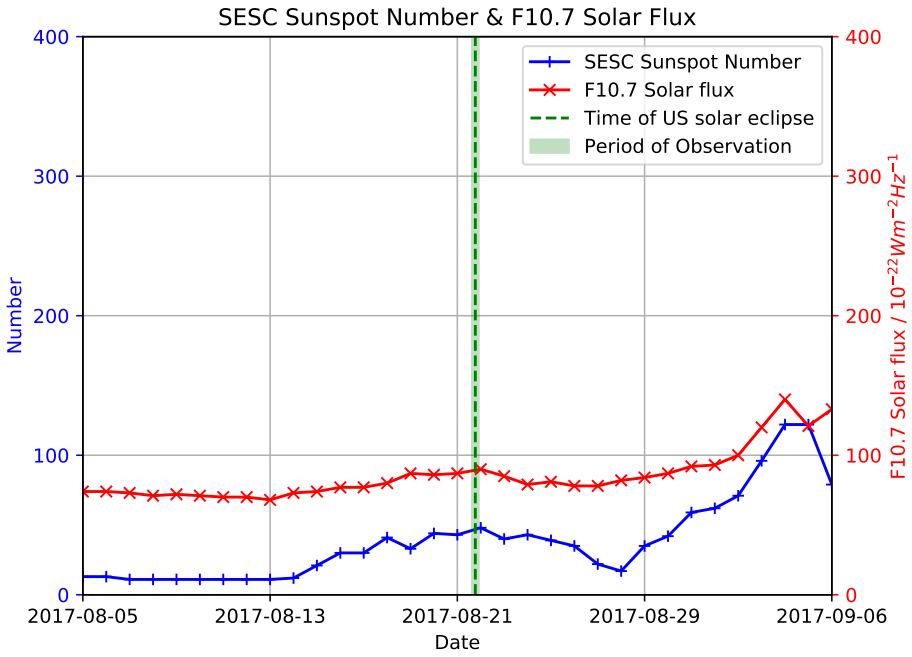

FIGURE 3.3: Observation of Solar Activity Indices, blue line for SESC Sunspot Number, red line for F10.7 Solar Flux index.

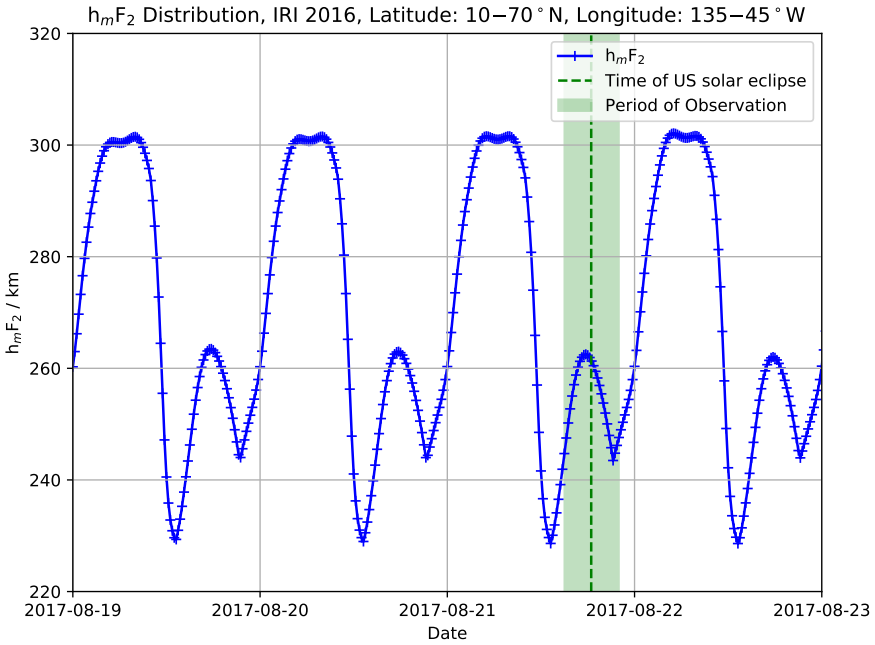

FIGURE 3.4: Climatic hmF2 at the region of 10–70°N & 135–45°W, based the International Reference Ionosphere (IRI) 2016 model.

3.3.1 GNSS Preprocessing and Detrending

The preprocessing of the GNSS data was carried out in the same way as in the introduction in section 1.2. A reminder is given next: first we obtained the ionospheric combination (also called geometry-free combination) $L_I(t)$ from the dual frequency carrier phases $L_1(t)$ and $L_2(t)$, as the difference $L_I(t) = L_1(t) - L_2(t)$ (in length units). The $L_I(t)$ is an affine function of the STEC, which we will denote as $S(t)$. This affine function consists of a linear coefficient and an intercept, which takes into account the carrier phase ambiguity and wind-up term. The main components of $S(t)$ are the TEC trends such as diurnal variations and elevation angle variation with low frequency and high energy, which we will denote as background component. Besides, another component of $S(t)$ of interest that has different frequency properties are the ionospheric fluctuations, such as the TIDs.

A method for separating the TID component from the background component, consists of computing the double difference (i.e., bandpass filter) of the time-series of measured $L_I(t)$. We will denote this double difference as $\tilde{S}(t)$ (see Hernández-Pajares, Juan, and Sanz, 2006). Taking into account the almost constant intercept in $L_I(t)$ when no new losses of lock (cycle slips) occur, we group the time series $L_I(t)$ into independent sub-series defined by the cycle-slips. In each sub-series, the intercepts can be considered constant, and thus can be eliminated by the double time difference divided by -2, see Eq. 1.2. Note that the time interval of the difference determines the enhanced frequency bands of the TIDs in $\tilde{S}(t)$. Although there is no definite agreement about the characteristics of bow waves generated by the eclipse (see the previous studies Chimonas and Hines, 1970a; Nayak and Yiğit, 2018; Zhang et al., 2017), these studies suggest a periodicity of TIDs of 20–60 min. Therefore, we selected $\Delta t = 600$ sec for the band pass filter in order to emphasize the eclipse-induced TIDs and also to greatly limit the effect of typical medium scale TIDs with 10 min of periods (see Hernández-Pajares et al., 2012b). This value allows high sensibility to the TIDs with periods of 12–60 min, attenuating the waves of other periods with a factor lower than $1/2$, whereas being relatively flat in this band.

The time evolution of the TIDs at different elevation angles is estimated from the detrended VTEC $\tilde{V}(t)$ which in turn is the projection of the detrended STEC $\tilde{S}(t)$ by means of a mapping function $M(t)$, i.e., $\tilde{V}(t) = \frac{\tilde{S}(t)}{M(t)}$, see Hernández-Pajares et al. (2011). This method assumes that $\tilde{S}(t)$ occurs at the ionospheric pierce points (IPPs). These IPPs are located on a shell with the mean effective height corresponding to the height where we assume that the TIDs commonly occur. We discarded observations with an elevation angle of less than 15° as a compromise between obtaining enough TIDs information and the effect of the angle on the mapping function errors.

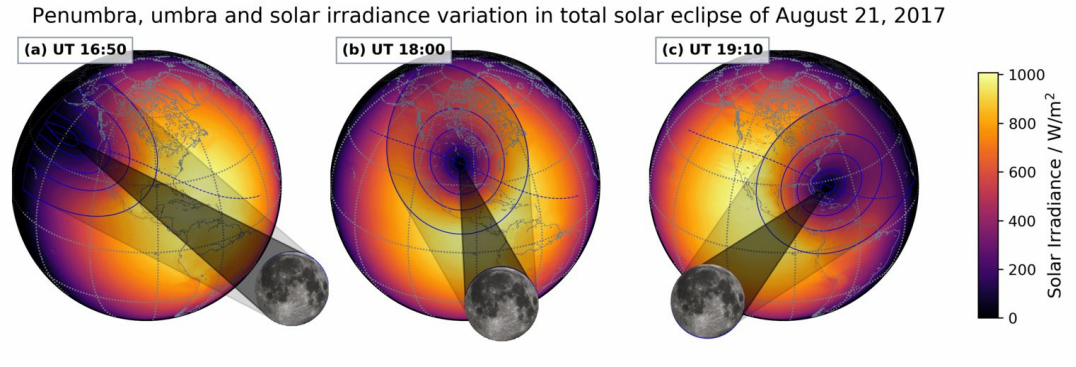

FIGURE 3.5: Variations of penumbra, umbra and solar irradiance at three moments of the eclipse, blue solid-line circles denote the penumbra in 0%, 25%, 50%, 75%, 90% of obscurations and the umbra, blue dashed line represents the eclipse totality, the color map shows the global horizontal irradiance at the height of 250 km.

We took 250 km as the mean effective height to detect these ionospheric disturbances. This is justified by the following reasons: (a) Hernández-Pajares, Juan, and Sanz (2006) point out that the maximum MSTID generation occurs at the height below hmF2 because the MSTIDs are generated by the interaction between the neutral and ion particles. (b) In the case of this eclipse, Huba and Drob (2017) predict the electron density would decrease in E-F region between 150 and 350 km. (c) Nayak and Yiğit (2018) and Zhang et al. (2017) point out that during the eclipse the height where the ionosphere shows the maximum perturbation typically in the E-F1 region below hmF2, as the response to the atmospheric gravity waves induced by the solar eclipse, which is consistent with the typical TIDs. (d) Sun et al. (2018) and Zhang et al. (2017) show the eclipse-induced large scale TIDs should be generated at the F region. (e) The regular hourly height distribution of peak electron density (hmF2) on this day ranged from 240 km to 310 km, in particular 240–270 km during the lunar shadow in U.S, see in Figure 3.4, obtained from U.S. NASA Goddard Space Flight Center (2016), see Bilitza et al. (2017).

In addition, the TID detection was performed independently for each GPS satellite, because TID activity measured from the detrended VTEC maps could occur at different heights. The analysis was performed taking this aspect into account.

3.3.2 Ionospheric Perturbation Description during the Solar Eclipse

In this work, the variation and movement of the moon shadow at the height of 250 km has been studied, in particular the area of umbra, and the iso-penumbra lines with different obsuration of 0%, 25%, 50%, 75% and 90%, see computation details in Montenbruck and Pfleger (2013). Also the global horizontal irradiance variation

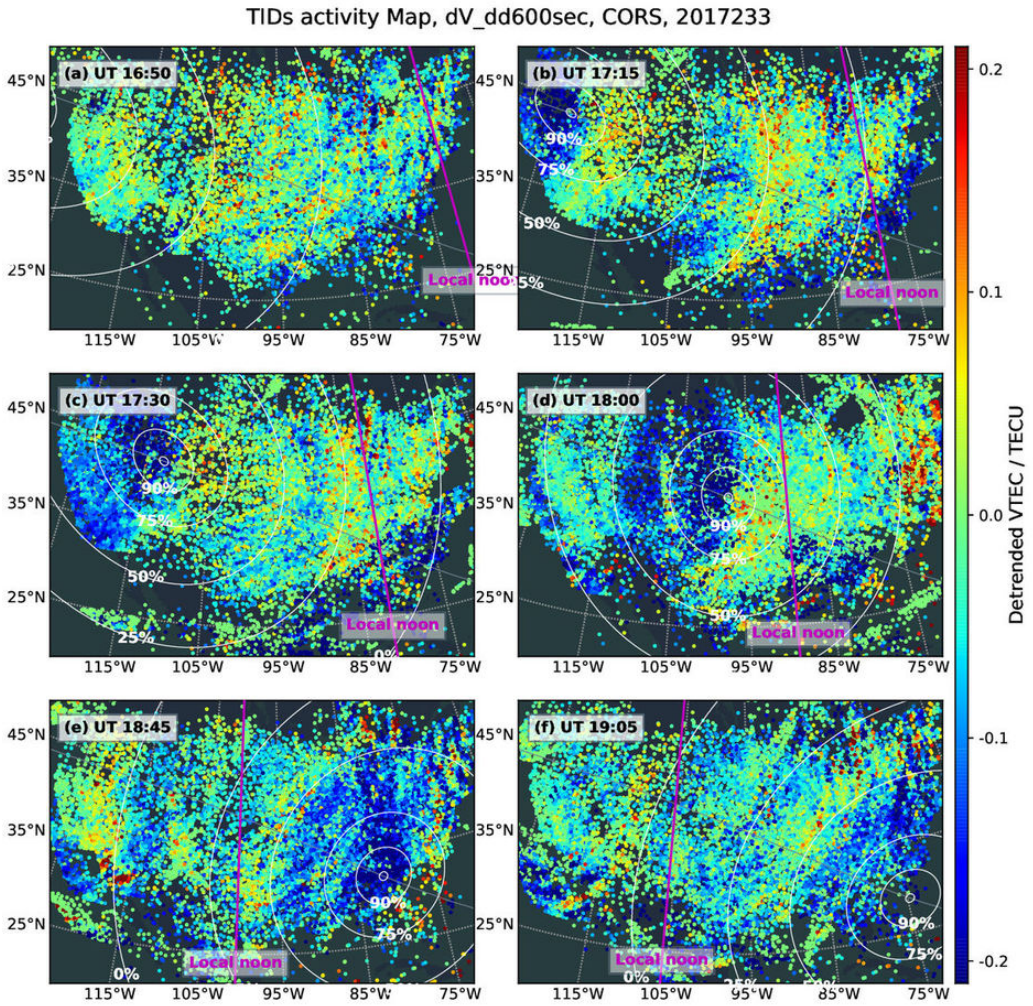

FIGURE 3.6: Ionospheric perturbation evolution during the solar eclipse, by means of TID maps (**a**–**f**): at 16:50, 17:15, 17:30, 18:00, 18:45, and 19:05 UT. White arcs denote the penumbra in 25%, 50%, 75%, 90% of obscurations and the umbra at the height of 250 km. The magenta line marks the local noon at the same altitude.

during the solar eclipse has been modeled, see simulation details in Andrews et al. (2014). As it is shown in Figure 3.5, where the lines of iso-penumbra and umbra, are superimposed with the simulated global horizontal irradiance color map.

In Figure 3.6, we show the ionospheric perturbations during the complete transit of the solar eclipse over the U.S. The maps were created by means of the GNSS sounding technique, described in subsection 3.3.1. In this figure we depict the detrended VTEC maps for all the GPS satellites at 6 representative moments of the eclipse period, namely, at 16:50, 17:15, 17:30, 18:00, 18:45 and 19:05 UT. Along with this

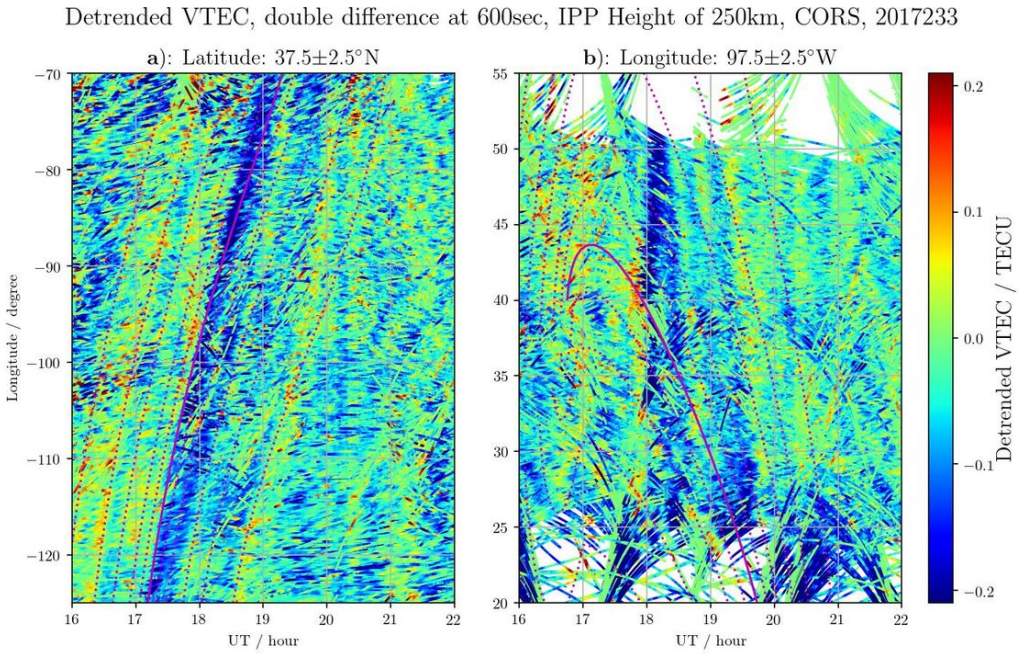

FIGURE 3.7: Ionospheric perturbation evolution during the solar eclipse from 16:00-22:00 UT, by means of along-longitude/along-latitude keograms with the bin of ±2.5°, for **a**) a fixed latitude 37.5°N and **b**) a fixed longitude 97.5°W. The magenta solid line denotes the zonal (**a**) / meridional (**b**) location of the umbra center, and the pairs of magenta dash lines around the magenta solid line show the zonal (**a**) / meridional (**b**) limits of the penumbra, where the obscuration is 90%, 75%, 50%, 25%, 0% respectively.

information, we display the location of the umbra and the different obscuration levels of penumbra. Superimposed over these maps, we show the iso-penumbra lines from 90% to 0% of obscuration when the umbra is over the Pacific ocean. Note the lines of iso-penumbra are computed at the height of 250 km, see Figure 3.5. At first glance, a large scale ionospheric disturbance propagates from northwest to southeast along the trajectory followed by the umbra, which is also known as the VTEC depletion as the response to the cooling effect, see Coster et al. (2017) and Zhang et al. (2017). In addition, several large scale ionospheric disturbances can be observed clearly before/after the umbra arrives, simultaneously a large number of medium scale ionospheric disturbances appear in the regions of the penumbra and umbra.

To make the ionospheric disturbances patterns more clear, in Figures 3.7–3.9 we plot three keograms for different bins of the detrended VTEC maps. Figure 3.7 shows the whole evolution of ionospheric disturbances during the eclipse at: a) the zonal band for the fixed latitude of 37.5°N with the width of 5 degrees and b) the meridional band for the fixed longitude of 97.5°W with the same width, with the zonal /

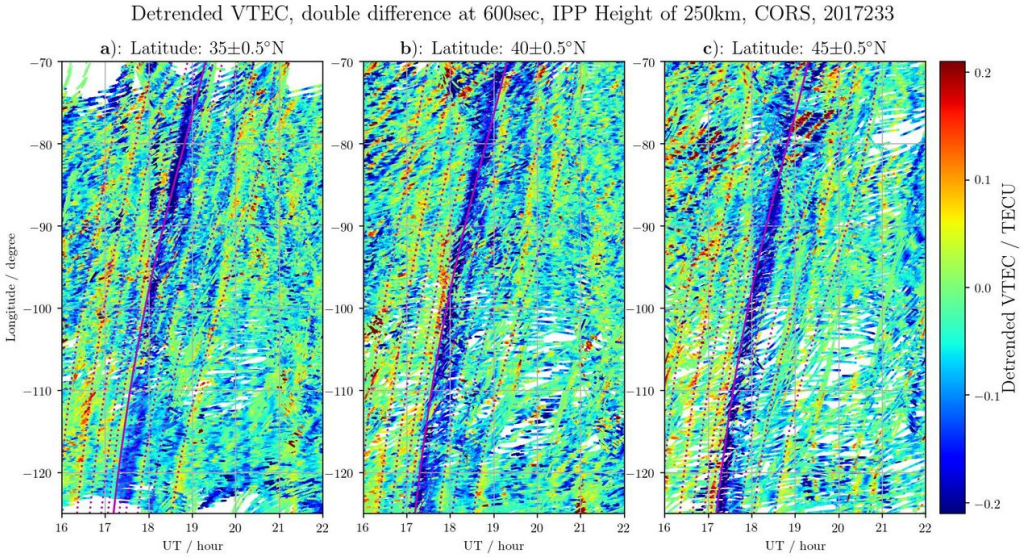

FIGURE 3.8: Ionospheric perturbation evolution during the solar eclipse from 16:00-22:00 UT, by means of along-longitude keograms with the bin of ±0.5°, for three fixed latitudes (**a**–**c**): 35°N, 40°N and 45°N. The color line scheme is organized as in Figure 3.7a.

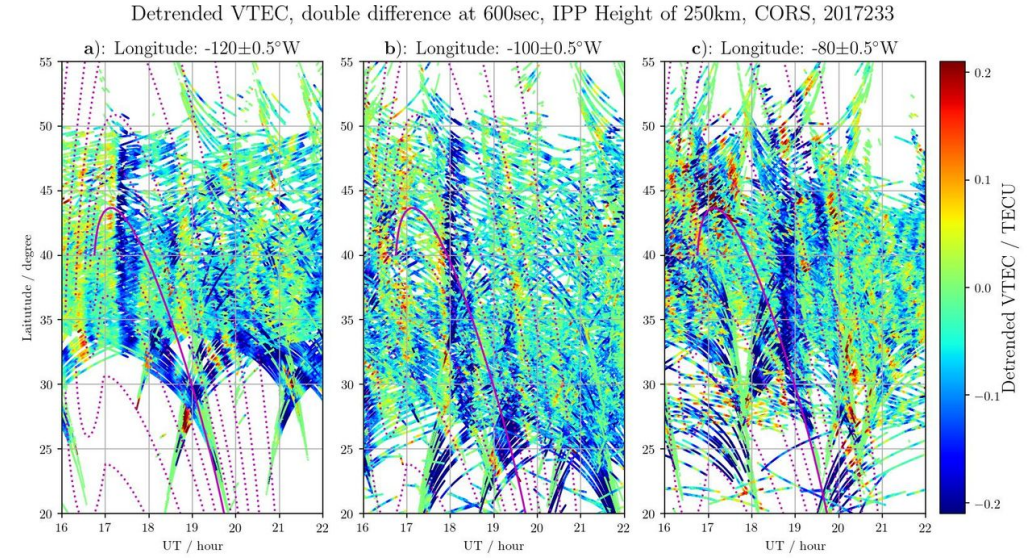

FIGURE 3.9: Ionospheric perturbation evolution during the solar eclipse from 16:00-22:00 UT, by means of along-latitude keograms with the bin of ±0.5° for three fixed longitudes (**a**–**c**): 120°W, 100°W and 80°W. The color line scheme is organized as in Figure 3.7b.

meridional limit lines of the penumbra with different obscuration. Similarly in Figure 3.6, the large scale disturbances clear shown in figures 3.7a and 3.7b propagate towards south and east, and across the two bands at about 17:10 and 18:00 UT, respectively. From Figure 3.7a, one can observe that the time delay, i.e. the difference between the location of disturbance and the umbra, is positive and small before the

umbra movement with a much lower speed at about 18:20 UT. The disturbance occurs with the scale larger than 15° latitude, when the umbra sweeps the meridional band at 17:55–18:05 UT in Figure 3.7b. Also the occurrence is shown in Figure 3.8, where three zonal bins at different latitudes (35, 40 and 45 °N) draw the behavior of the same disturbance evolution. As a supplementary illustration, the three meridional bins in Figure 3.9 (at 120, 100 and 80 °W) show the occurrence of the same disturbance sequentially. In another phase, beginning at around 16:40 UT before the umbra arrival, a large scale disturbance appears at the location where the penumbra with the 50% obscuration arrives, as shown in Figures 3.7a, 3.8 and 3.9. And another large scale disturbance is also found in the 50–75% obscuration penumbra after the umbra left, starting at about 18:00 UT. This large scale disturbance could be the ionospheric response directly originating from the thermosphere, see the compatible reports in Coster et al. (2017), Sun et al. (2018), and Yang, Monte Moreno, and Hernández-Pajares (2018). Note that medium scale disturbances are shown in more than 4 space-time locations from these figures, which appear often during the eclipse transit, for instance the disturbances occurring before the umbra arrival, particularly during the region of 70–100°W longitude, i.e. in the east subnetwork of the U.S., see Figure 3.8 and compatible behavior in Figure 3.6. Moreover, the disturbances located in the penumbra after the umbra are also clearly shown in these Figures. The observation of the medium scale distrubances also shows the consistent occurrence with the precedents in Nayak and Yiğit (2018), Yang, Monte Moreno, and Hernández-Pajares (2018), and Zhang et al. (2017).

Figures 3.6–3.9 show the complicated and varied behaviour of the multi-scale ionospheric disturbances during the transit of the shadow of the moon over the ionosphere above the North America. Nevertheless, as the parameters related to the propagation of the ionospheric disturbances are extremely hard to be determined from measurements done by visual inspection, we will use the the ADDTID algorithm (described in section 3.4), which can simultaneously detect properties and parameters of multi-TIDs.

3.4 Methodology of TIDs Determination

In the introduction, we presented a summary of the possible explanations of the different types of disturbances produced by the eclipse transit over the continent. These include bow waves and other related disturbances. These bow waves consist of several simultaneous TIDs induced by different causes, among them, the upward atmospheric gravity waves (Chimonas and Hines, 1970a). In addition we detected early perturbations, and perturbations that persist after the transit.

In this study, the detection of several simultaneous TIDs was implemented in the following two steps: (a) the TIDs characterization by means of the ADDTID algorithm that automatically detects them and estimates their parameters from the detrended VTEC maps (Section 3.4.1); (b) The details of subdivision criterion of the network for improving the performance of the ADDTID algorithm (Section 3.4.2).

3.4.1 Summary of ADDTID

The analysis of the data was done by means of the Atomic Decomposition Detector of Traveling Ionospheric Disturbances algorithm (ADDTID, see details in chapter 1, Yang, Monte-Moreno, and Hernández-Pajares, 2017). This algorithm uses data from a dense GNSS receiver network, and can detect and characterize TIDs from the ionospheric piercing points (IPPs). The algorithm creates a dictionary of possible waves that encompass the geographical area under study. The estimation is done using only the IPP samples, and solving a convex optimization problem with a regularization term. This algorithm determines the TIDs as the elements of the dictionary that best approximate the observations at the IPPs. Stating the problem in this way has several advantages, mainly, that the number of possible waves to be detected does not have to be stated beforehand. Also, and perhaps the most challenging aspect of the estimation problem, the algorithm can work with non uniform spatial sampling, including the presence of directions with higher density of sensors, or regions of the network lacking sensors.

3.4.2 Justification of the Network Subdivision Criterion to Enhance the ADDTID Performance

The model ADDTID, assumes that the TIDs propagate in the form of plane waves. In practice, the TIDs, as is shown in the Figure 3.6, show a propagation pattern that follows the shape of the eclipse iso-penumbra lines (shown in white). These iso-penumbra lines for different elevations show a shape similar to an ellipse. In this case the equivalent to the eccentricity of an ellipse, depends on the inclination of the eclipse's shadow. These ellipse-shaped shadow gradually decreases the amount of solar irradiance incident on the atmosphere. For the physical intuition of the inclinations and obscurations see Figure 3.5. This gradual obscuration in space and time, causes the electron density oscillations, that follow a complex and complicated response at different scales. An example of the wealth of phenomena is shown in Figure 3.6, which shows the disturbances follow the iso-penumbra lines for different inclinations. The disturbances include: bow-shaped wavefronts, partial circular wavefronts, receding ripples and planar wavefronts in different scales. As a precedent, in which similar phenomena are observed see Sun et al. (2018) and Zhang et al.

(2017). This suggests that a natural model for the dictionary matrix D of the ADDTID algorithm, should include all possible quadratic patterns of wave propagation. Nevertheless, this is prohibitive from the computational point of view because the size of the dictionary grows by a polynomial of the number of parameters.

As mentioned in Section 3.4.1, the ADDTID algorithm can approximately estimate these circular waves as compositions of local planar waves. This means, for instance, that a given wave front of a bow wave, would be detected as two planar waves propagating in symmetric directions at each side of the main direction of propagation. In Figures 3.6a and 3.12, we show a visual example of the validity of the plane wave approximation. At this moment, the detrended VTEC maps over the local net of California show a near plane wave structure, which corresponds to the detected waves at the scatter plot (Figure 3.12b and 3.12c). This scatter plot at 17:15–17:45 UT, shows that the detected planar TIDs are distributed along two main directions that are symmetric with the main propagation azimuth that is approximately 90 degrees. At simple glance, we can see on the map measured at the same moment, there are two flat fronts, with the same azimuths detected by the algorithm. (Note in the subplots at Figure 3.12e–3.12h, the alignment of dots of same intensity distributed following lines).

This indicates that the size of the measuring network has to be such that the curvature of the wavefront should be small. As it is shown in Figure 3.1, we divided the CORS GNSS network that covers the US into several smaller subnetworks, each covering an area where the resulting TIDs can be locally approximated by a planar wave. The partition into subnetworks was done taking into account the different scale bow waves reported in Sun et al. (2018) and Zhang et al. (2017), the scheme of division is two sub-networks, the West Coast and the East Coast. This is because the ADDTID algorithm that was used for detecting the TIDs assumes that the waves to be detected are planar and cover a significant part of the stations. This hypothesis is approximately true if the whole net is partitioned into subnets. A feature of the algorithm that is relevant for this study, is that the estimation is robust to non uniform sampling and the geographical orientation of the set of stations.

In a more detailed way, the division of the network is justified because of the following reasons. (a) The disturbances that are generated by the eclipse can be approximated locally as plane waves, but at the scale of the whole network the curvature can be significant (see for instance Figure 3.6). Thus, the size of the partition of the network was such that inside a partition, the wave front can be approximated as planar, and corresponding parts away from the umbra, which exhibit a greater curvature, are included in the neighbouring partition. (b) As can be seen in Figure 3.1, the central part of the network has a lower density of stations, which has an effect

in the accuracy of the estimation. Therefore it is a natural region for deciding the border between partitions. (c) We allowed for an overlap of about 10% between subnetworks, in order to be able to check the consistency of the estimates between them. (d) Finally, the partition is also justified because the disturbances caused by the eclipse were different from one geographical area to another.

An additional benefit is the fact that the propagation of the waves at either coast follow similar azimuths and wavelengths, but the velocities may sometimes have a different sign. As an example of this see the TID maps in Figures 3.6a and 3.6f, particularly in Figure 3.10d for GPS satellite PRN 2 and Figure 3.11d for GPS satellite PRN 12, where the wavefronts in the west and east parts have differences in their azimuth and wavelength. Another benefit of the geographical partition into subnets is that this allows for explaining phenomena that are qualitatively different and might appear mixed if the analysis were done with the entire network.

For instance in Figure 3.6, we show a measurement done with all the satellites and stations. From visual inspection, one can see that the wave forms follow the curvature of the umbra, and that the wavelengths are not uniform. In addition, in the east section of network (about 100°W to 80°W of longitude, and 28°N to 50°N of latitude) a set of ripple waves can be observed, that have a much shorter wavelengths compared with the main ones that cover the whole continent. This idea of partitioning the network as a function of the scale of the disturbances allows for analyzing the ripples as medium scale TIDs, by dividing CORS into subnetworks with the geographic scale of $10^\circ \times 10^\circ$ (latitude vs. longitude), see details in Section 3.5.5.

3.5 Results and Discussion

In this section, we will analyze the diverse types of ionospheric disturbances generated during the eclipse transit at a height of 250 km. The analysis will be done by means of the ADDTID algorithm and by visual inspection of the maps. The TIDs that we detected (and visually verified) show a wide range of features that depend on the elevation angle change, the footprint, size, azimuth and velocity of the umbra. We have structured the analysis of the generated TIDs, first following the temporal evolution of the eclipse and finally a global summary:

1. Time-varying TIDs analysis of the early and final moments of the eclipse observed from California in Section 3.5.1.

2. Simultaneous TIDs with multi-scale wavelengths presented during the middle stage of the eclipse observed from California in Section 3.5.2.

3. In Section 3.5.3, we summarize the detected multi-scale TIDs during the whole transit of the eclipse.
4. In Section 3.5.4, we show in detail the features of bow waves consisting of large scale TIDs, and in particular the estimated opening angles.
5. The medium scale TIDs in the penumbra are described in Section 3.5.5, such as partial circular waves, apparition of receding ripples among others.
6. In Section 3.5.6, a set of early MSTIDs at the east coast is detected before the arrival of penumbra.

3.5.1 Time Varying TIDs Wavelengths in the Early and Final Stages of Eclipse Transit

In this section, we will describe the temporal evolution of the TIDs in the early and final stages of the eclipse. The description will be carried out simultaneously, by means of the parameters detected with the ADDTID algorithm and by visual observation of the maps for verification purposes.

The disturbances that appear in the early and final stages of the eclipse, coincide with the distribution of the TIDs when the umbra is either about to enter the continent or to leave it. The eclipse-induced ionospheric perturbations would primarily be the consequences of the atmospheric cooling effect at all heights. However, the response of the ionosphere to the cooling due to the rapid variation of the penumbra is not well understood. The consequence is that the movement of the shadow generates fast space-varying and time-varying cooling effects in the atmosphere, see Figure 3.5. This movement is in part due to change in the grazing angle at the different stages of eclipse. The main feature is that for grazing angles of the umbra, the penumbra creates elliptic-like shadows of gradual obscuration. On the other hand, for vertical angles the shadows of the penumbra show less eccentricity. The geometry of the problem gives rise to a changing velocity of the penumbra shadows. That is, while the angle increases steadily, the velocity of change of the elliptical shadow of the penumbra will be high during the transition from grazing angles to medium angles.

As reported in Sun et al. (2018) and Zhang et al. (2017), the eclipse-induced ionospheric disturbances can be classified into two categories with distinct scales: (a) bow-shaped large scale TIDs and (b) medium scale TIDs of bow waves, originated respectively by in situ and not in situ gravity wave effects. In this subsection we will study both kinds of the disturbances in a separate subnetwork centered at California, (see in Figure 3.1). The California network is defined as a more restricted geographical area, which covers a smaller region, with a high density of stations allowing a

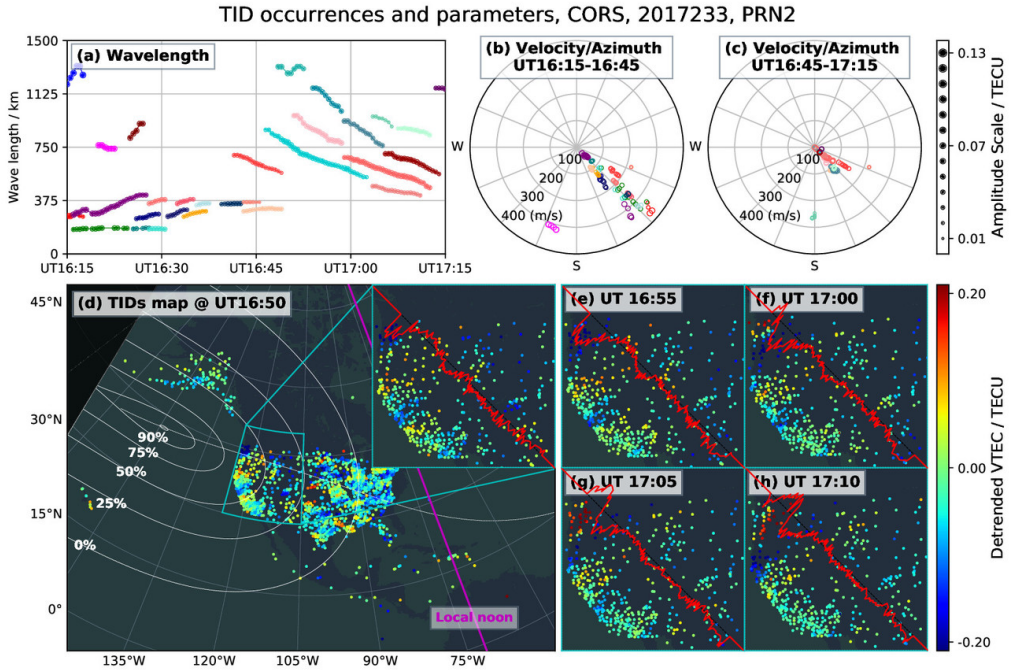

FIGURE 3.10: Time-variation plots of the TID parameters, when the penumbra of about 50% obscuration covers the west part of CORS GNSS network, estimated from GPS satellite PRN2. (**a**): time evolution of the TIDs wavelengths, (**b**,**c**): velocity vs. azimuth polar plots at intervals of half an hour, the continuity and amplitude of TIDs are coded by colors and the dot sizes respectively. (**d**–**h**): TIDs activity maps at 16:50 UT, 16:55 UT, 17:00 UT, 17:05 UT and 17:10 UT, the white arcs marked with percentages are the iso-penumbra lines on the IPPs at the altitude of 250 km. The diagonal white line is the trajectory of the umbra's center and the magenta line marks the local noon at the altitude of 250 km. The red curves denote the projection of detrended VTEC in the NW-SE direction.

more clear detection and modelling of the TIDs, because they can be locally approximated by a planar wave. Another reason we limit ourselves to this subnet is that for grazing angles, the distribution of TIDs will be very different across the continent, which could result in a mixture of different effects. The result of this change in angle, is the emergence of a set of TIDs, with a wavelength time evolution that follows a parabolic shape. This parabolic shape of the evolution in time of the wavelength is common to the entering and departing phases of the umbra and penumbra.

3.5.1.1 The Early Stage of Eclipse Transit

Figure 3.10 (GNSS observation of GPS satellite PRN2) shows the entry phase of the eclipse. Figure 3.10d to 3.10h show TEC maps of the west coast between 16:50 UT

and 17:10 UT. Superimposed over these maps, we show the iso-penumbra lines from 90% to 0% of obscuration, when the umbra is over the Pacific ocean. By means of the algorithm presented in Montenbruck and Pfleger (2013), the lines of iso-penumbra are depicted at an altitude of 250 km, as far as the measurements over the set of stations over the continent. The lower right part shows a zoom of the TEC evolution at time intervals of 5 min. The upper part of the figure shows the time evolution of the TID wavelengths (Figure 3.10a) and the two polar plots of azimuth vs velocity (Figure 3.10b, 3.10c). Wavelengths, azimuth, velocity and amplitude are all estimated by the ADDTID algorithm. Please note that the azimuths and wavelengths given by the ADDTID coincide with the values that can be estimated at glance from Figure 3.10d–3.10h. In addition, we have overlaid on the maps, the projection of the detected points to a straight line with an inclination equal to the most common azimuth of the detected TIDs. Please note that the projection allows the visual inspection to determine the approximate wavelength of the disturbances and the propagation azimuth. As a supplement to Figure 3.10, we have posted on the Internet VTEC variation films during the eclipse in Yang (2018c).

Next, we will describe the evolution of the TID estimated by means of the ADDTID algorithm, and we will contrast it with the measured maps. Beginning at 15:55 UT, the penumbra contacts the ionosphere over west US region, and, from then on, increasingly covers this region. The time evolution of the TIDs in the early 30 min, show Medium Scale TIDs (MSTIDs) with a wavelength in the range of 250 to 300 km, a propagation following an azimuth towards the southeast. Please note that although the distribution of velocities is broad, most of the observations (75%) are concentrated in the range 150–300 m/s. The amplitudes during this time interval decreased from 0.08 to 0.02 TECU. The color-coding convention we have followed assigns a different color to each continuously detected TID sequence. The same colors have been assigned to the wavelength paths and points in the azimuth vs. velocity diagram. The MSTIDs detected during local morning hours show the typical daytime pattern in summer, mostly driven by solar terminator, see similar reports in Hernández-Pajares et al. (2012b). At about 16:45 UT, the MSTIDs suddenly disappear, and a set of long wavelength TIDs emerge, which show a downward trend starting at a value of 1125 km. This change coincides with the arrival of the penumbra at a level of obscuration of 50–75%, as can be seen from the geographical distribution of the iso-penumbra lines in Figure 3.10d. The azimuth of the long wavelength TIDs moves 10 degrees to the east, the velocity, as seen in Figure 3.10c decreases from 150 to 50 m/s, and the period decreases from 3 to 0.75 h. This can be confirmed by visual inspection of Figures 3.10d to 3.10h. Meanwhile, the umbra above the Pacific ocean moves towards east at a speed of about 3000 m/s. Around 17:15 UT, 55 min after the onset of the penumbra reaches the network, the penumbra

reaches a 50% obscuration, and the wavelength of the TIDs converges to a value of 400 km. As shown in Figure 3.12, this occurs a few minutes after the umbra contacts the California network.

The phenomena that we have described can be explained from the physical point of view in several ways (see discussion of the literature on this topic in the introduction). Zhang et al. (2017) observed the penumbra-induced TIDs and recognized as the partial bow waves which should originate from the neutral atmosphere when the ground shadow is of about 50% magnitude. The time interval between the onset of TIDs and the time when the penumbra first arrives in California is compatible with the 0.5–1 h delay range of the onset of TIDs according to Liu et al. (2011b) and Nayak and Yiğit (2018). Another phenomena that are observed in this paper are the bow waves and related disturbances, and the different delays in the apparition of the ionospheric disturbances. Shock waves are believed to originate from gravity waves in the middle atmosphere, due to the umbra moving at supersonic speeds. On the other hand, the penumbra that partially covers the solar radiation produces a cooling mechanism different from the umbra. This effect encompasses several frequency bands. Huba and Drob (2017) indicate that the moon blocks the irradiance of ultraviolet (UV) light (uniform in the solar disk) in a similar way to light in the visual spectrum. In Kazadzis et al. (2007), it is observed that a significant part of the ozone column decreases when the obscuration associated with darkness exceeds 70%. As the column variation in the ozone layer absorbs most part of UV radiation, the cooling effects by the low obscuration penumbra become insufficient to break the heat balance in the middle atmosphere. Therefore, these TIDs, observed tens of minutes prior to the coverage by the 50% obscuration penumbra, might have a different origin. The global horizontal irradiance of the region covered by the umbra and penumbra is depicted in the diagram of Figure 3.5. The decreasing intensity of the irradiance from center outwards, generates different cooling effects, similar to a solar terminator, with a very fast diurnal variation. For instance, the irradiance of X-ray and Extreme UV (EUV) is the primary source of photoionization in the ionosphere, Huba and Drob (2017) reported their delayed variation when the solar disk is occluded by the moon. This is because 10–20% contribution in these bands is generated at the solar corona, which is not covered by the moon. On the other hand, Coster et al. (2017) observed the TEC depletion follow with a short time delay the radiation distribution induced by the shadow, and reported the penumbra-induced large scale TIDs activities could be originated in situ with the thermosphere. This explains the above mentioned set of long wavelength TIDs, that appeared suddenly when the coverage of the penumbra reached the 50% of obscuration, and the following convergence of the TIDs about a few minutes after the umbra reaches the network. It is also compatible with the ionospheric disturbances reported by Le et

al. (2008), Müller-Wodarg, Aylward, and Lockwood (1998), and Sun et al. (2018), which would be directly generated in the thermosphere.

Figure 3.10 shows that the wavelength trajectory of long wavelength TIDs follows a descending parallel parabolic shape. This path is compatible with decreasing the distance between the iso-penumbra lines. That is to say, the solar irradiance gradient increases as the angle of the shadow increases from 6 degrees to 40 degrees, with the consequent reduction in the rate of variation of the iso-penumbra lines. At the same time, the direction of propagation (southeastbound) of TIDs is perpendicular to the iso-penumbra lines over the California network. The cooling effect on the California area increases considerably as the angle and speed increases. This speed is supersonic at the heights where disturbances occur. In conclusion, this shows that the deceleration of the rate of change of the area of the penumbra and the decrease of the such area, is associated with a decrease of the wavelength of the TIDs. This happens in spite of the fact that the speed of the TIDs is slower than that of the umbra.

As for bow waves, the shape of the TIDs induced by the penumbra is consistent with bow waves of variable aperture in the south direction. One aspect to note is that the geomagnetic lines give rise to a slight deviation towards the equator due to the low geomagnetic activity, as mentioned in Section 3.2, see Coster et al. (2017).

3.5.1.2 The Final Stage of Eclipse Transit

In Figure 3.11 we show the departing phase of the eclipse, for more details see the movie in Yang (2018b). The measurement has been made in the California subnetwork when the umbra is over the Atlantic Ocean, which results in a varying grazing angle of the penumbra. The parameters shown in the figure were estimated on the west part of CORS GNSS network, using the GPS satellite PRN12. The temporal evolution of the wavelength shows, for the departing phase, a complementary behaviour to that observed in the entering phase of the eclipse. The differences are due to the fact that the decrease rate of change of the elevation angle of the moon is not exactly the opposite of the entering phase of the eclipse (see Figure 3.5). On the other hand, the azimuth of the detected wavefronts is compatible with the direction of the iso-penumbra lines over the network.

At about 19:35 UT, the TIDs with increasing wavelength get weaker and finally disappear when the wavelength is over 1200 km. Subsequently, the activity of the disturbances decreases significantly, after which only very low intensity TIDs are detected. These disturbances have an azimuth opposite to that of the typical disturbances of this time of year.

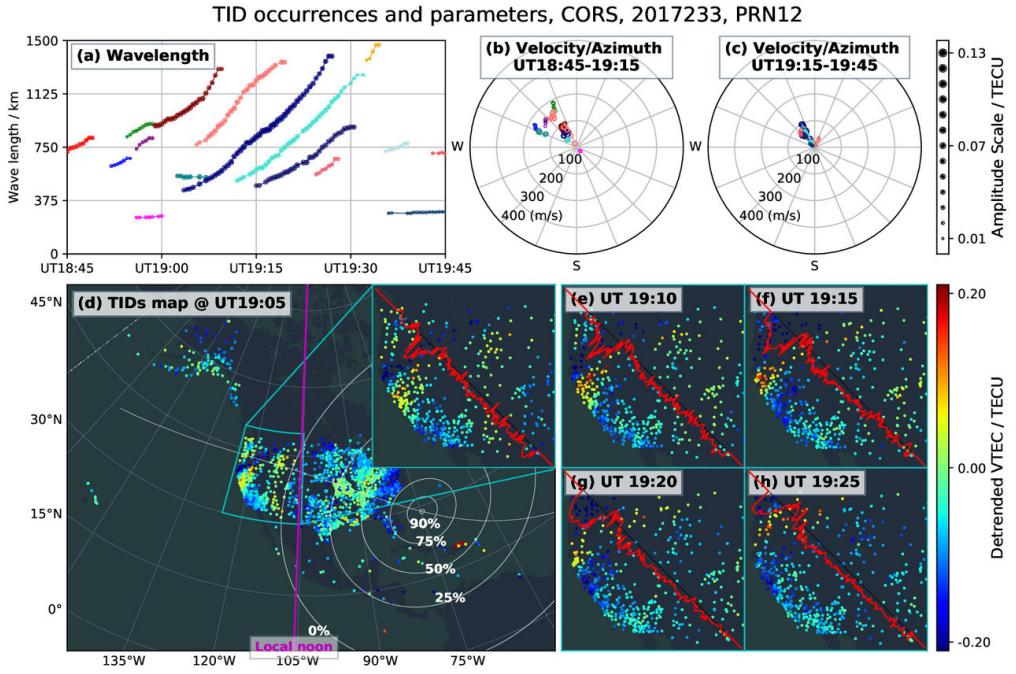

FIGURE 3.11: Time-variation plots of the TIDs parameters, when the penumbra of about 0% obscuration in the west part of CORS GNSS network, estimated from GPS satellite PRN12, organized as in Figure 3.10. (**a**–**c**): Wavelength and velocity/azimuth plots. (**d**–**h**): TIDs activity maps at 19:05 UT, 19:10 UT, 19:15 UT, 19:20 UT and 19:25 UT.

.

The TIDs that have been detected show similarities with those of the initial stage, in the sense that the direction of propagation is perpendicular to the iso-penumbra lines, the range of velocities is similar, and they are not significantly affected by the geomagnetic fields. A difference with respect to the TIDs of the initial stage of the eclipse is that the propagation is in the opposite direction to the movement of the shadow, which indicates that there may be no relation with the variation of the penumbra. In addition, these TIDs occur at the time when the shade is at its lowest, i.e., when the shadow leaves the California region, about 105 min after the umbra and about 85 min after the iso-penumbra level of 50% leaves the subnetwork. This suggests that the fluctuations of the ionosphere are not due to the direct cooling effect in the thermosphere, but are upward gravity wave disturbances originating in the neutral atmosphere. Nevertheless, the behavior of the TIDs differs from Coster et al. (2017) and Zhang et al. (2017). Chimonas and Hines (1970a) explains the above-mentioned behavior of disturbances by stating that long period atmospheric gravity waves cannot ascend from the point of generation at a sufficiently steep angle. From theoretical considerations, they conclude that the period of the disturbances is 3 to

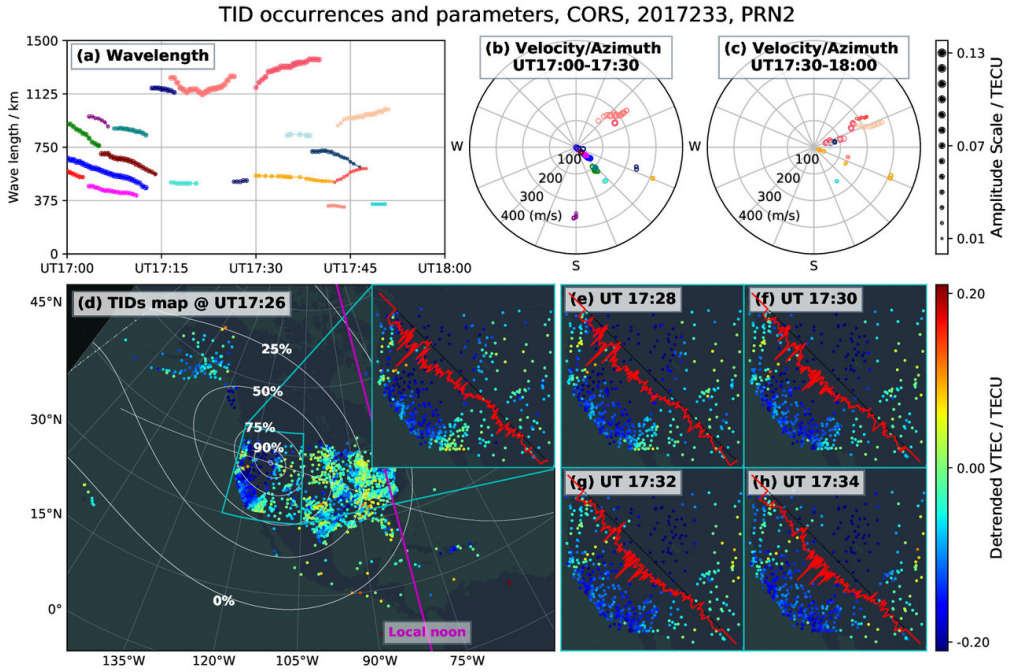

FIGURE 3.12: Time-variation plots of the TIDs parameters, when the umbra covers the west part of CORS GNSS network, estimated from GPS satellite PRN2, organized as Figure 3.10. (**a**–**c**): Wavelength and velocity/azimuth plots. (**d**–**h**): TIDs activity maps at 17:26 UT, 17:28 UT, 17:30 UT, 17:32 UT and 17:34 UT.

4 h, which is in line with the results of the estimate we have made. The period of the TIDs detected in the F region increases gradually from 1 to 5 h. Similarly, in a study related to the 7 March 1970 eclipse, Davis and Da Rosa (1970), in synchrony when the penumbra boundary (i.e., 0% area) left the network, observed westward TIDs in the form of decreasing amplitude shock waves with gradually increasing periods. However, the period of the TIDs estimated was of about 25 min, which was not consistent with the predicted long period in Chimonas and Hines (1970a).

3.5.2 General Description of Multi-Scale TIDs in the Middle Stage of Eclipse Transit

In this subsection, we show the presence of the multi-scale TIDs, i.e., medium and large, measured from the California subnetwork.

Figure 3.12 shows the characteristics of ionospheric perturbations when the umbra crosses the California subnetwork. For more details see the movie in Yang (2018c). The umbra contacts the atmosphere above this region at a height of 250 km at about 17:11 UT and leaves the subnetwork at about 17:42 UT. As mentioned in Section 3.5.1,

during the early stage, the set of parallel wavelength-varying TIDs from 17:00 UT follow a downwards trajectory, converging towards a medium scale wavelength TID of about 400 km, 4 min after the arrival of the umbra. Almost simultaneously, with a slight delay due to the response of the ionosphere (see Figure 3.12a), a disturbance suddenly appears with a wavelength of 1125 km at about 45 degrees of azimuth, nearly 90 degree to the north of the medium scale TID azimuth. This perturbation corresponds to the three segments of the trajectory observed at Figure 3.12a. Please note that the trajectories of large-scale disturbances are reflected on the projection (in red) in Figure 3.12e–3.12h, as almost two cycles of a sine wave with a wavelength compatible with 1200 km.

Both disturbances persist between 17:15 UT and 17:45 UT, the long scale disturbance with an amplitude of about 0.11 TECU and the medium scale of about 0.05 TECU for other. The spread in terms of azimuth of both perturbations shifts several degrees towards the east, which is compatible with the lines of equal penumbra and perturbations shown in Figure 3.10. The disturbance of longer wavelength can be found by visual inspection in Figure 3.12.

Although the observed velocities of both sets of TIDs are lower than the typical velocities for large and medium scale TIDs, there is a consistency, in the sense that the large scale TIDs propagate at a double speed compared to the medium scale waves.

Note also that the area spanned by the stations is smaller than the area covered by the bow wave, therefore only one of the branches of the bow wave is detected in the figure. Another effect that can be observed in the maps and the wavelength vs. time figure (Figure 3.12), is that the amplitude of the large scale TIDs is greater than in the case of the medium scale TIDs (note that the amplitude is coded by the size of the dots). An additional observation from this Figure, is that the azimuth of the TIDs does not coincide with the trajectory of the eclipse on the maps. This might be related to the movement of the bow wave fronts both in large and medium scales. In the figure there are also disturbances that appear in advance of the umbra.

These medium scale TIDs are the response of the ionosphere to the transition from the penumbra to the umbra, which generates the ionospheric wave in situ. Although long scale TIDs are also due to the effect of the umbra on the ionosphere, with delay appearing after the umbra has already moved away (Sun et al., 2018), such TIDs originate in part due to the cooling effect of the umbra's shadow, creating gravity waves in the thermosphere.

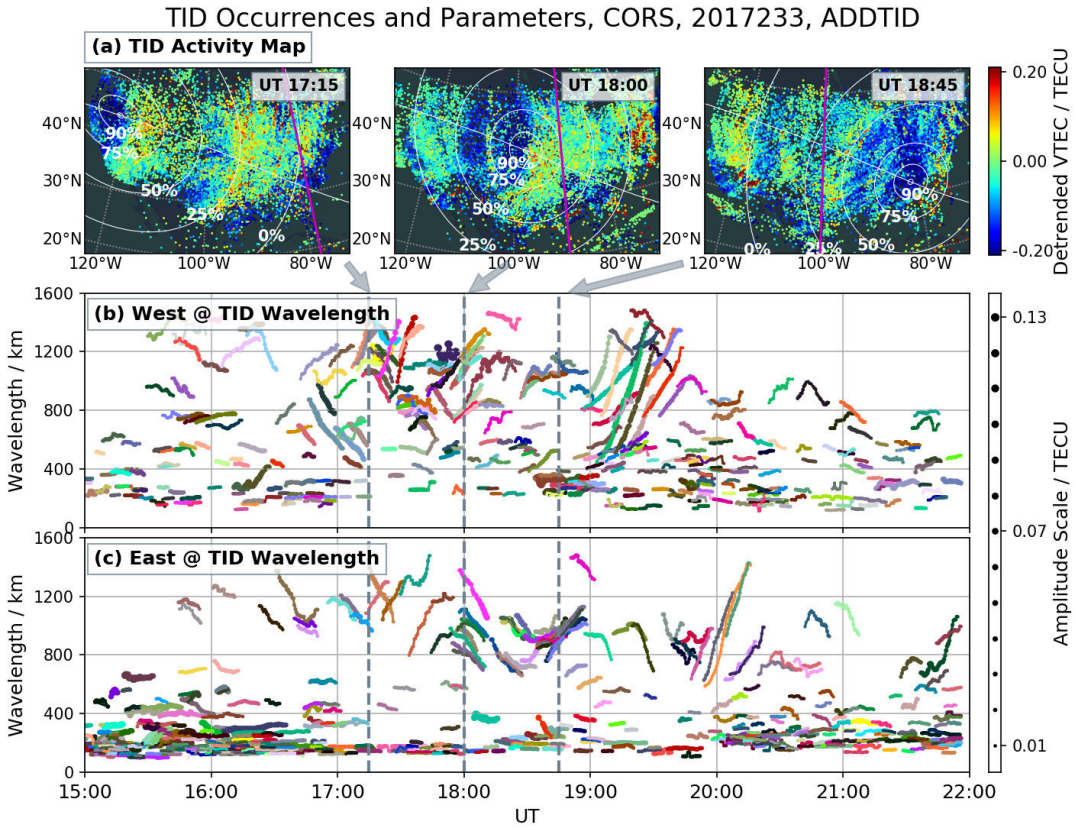

FIGURE 3.13: (**a**): TIDs activity maps at 17:15 UT, 18:00 UT and 18:45 UT, similar display scheme with the TIDs map in Figure 3.10. (**b**,**c**): Wavelength time evolution for the west subnetwork (b) and east subnetwork (c), point color and size code organized as Figure 3.10. The grey arrows pointing to dashed vertical grey lines indicate observation time.

3.5.3 Description of Ionospheric Disturbances during the Eclipse

In this section we will characterize and describe the ionospheric disturbances related to the bow waves during the transit of the eclipse.

By visual inspection, in the maps plotted at Figure 3.13a, one can see a bow wave that varies gradually throughout the eclipse (see more details in Yang, 2018a). In the three maps, in addition to the bow wave, it is also possible to observe disturbances in advance of the umbra, and in the wake of the umbra (see similar observations in Zhang et al., 2017). The shape of the waveforms of the disturbances are akin to the lines of iso-penumbra in Figure 3.5. That is, the disturbances in advance of the umbra follow the shape of the lines of iso-penumbra. The disturbances in the wake of the umbra show an elliptical curvature following the shape of the lines of iso-penumbra, and also ripples (Figure 3.13a at 18:45 UT) of lower wavelength with a complementary curvature.

In Sections 3.5.1 and 3.5.2, we show, on the west coast, the occurrence of disturbances at medium and large scales, ranging from a few hundred to more than a thousand kilometers. This phenomenon can be seen on the maps in Figure 3.13a. In Figure 3.13c, we also show that the measurements on the east coast follow, with a delay, the shape of the wavelength evolution on the west coast. The occurrences of these disturbances are compatible with the visual description in section 3.3.2.

These ionospheric disturbances during the eclipse appear as patches of 2D non-concentric near circular wave patterns, moving horizontally. Since the curvature of the TIDs over the region of each network is small enough, the ADDTID algorithm will be able to correctly detect the disturbances and estimate their characteristics. To better understand the spatial-temporal characteristics of large-scale ionospheric disturbances and their relationship to the eclipse, the estimation has been made with the entire CORS network. That is, the GNSS data used in the ADDTID algorithm correspond to the two subnetworks into which we have divided the CORS network (see Section 3.2). Please note that the size of area of each subnetwork is at least twice the maximum wavelength. Figures 3.13b and 3.13c show the time evolutions of the TID wavelengths respectively detected from west and east subnetworks of the CORS network.

The disturbance in advance of the umbra can be understood as an early bow wave. The origin is due to the changes in temperature generated by the increasing penumbra, giving rise to disturbances of lower intensity in comparison with the one that was generated by the umbra (Le et al., 2008; Müller-Wodarg, Aylward, and Lockwood, 1998). As the penumbra moves at a higher speed for grazing angles, the perturbation due to the eclipse appears some time before the umbra reaches the region covered by the stations. Also, the perturbation follows a distribution similar to concentric ellipses, which is due the change on the angle of the umbra over a sphere (see for instance the diagram in Figure 3.5 and the previous discussion in Section 3.5.1). These disturbances in advance to the bow wave can be observed clearly in Figure 3.13a at 17:15 UT.

The measures done at the stations over the west subnetwork show that the typical pattern of MSTID at this time of the year disappear completely, while on the east subnetwork, which is at the other side of the continent, they are reduced in number. In both cases the behaviour of the large scale TID (LSTID) changes, in case of the west subnetwork there is a noticeably decrease in the wavelengths of these disturbances. With a delay of about half an hour, the same phenomenon appears on the east subnetwork. A remarkable aspect is the continuity between the MSTIDs and the LSTIDs, which can be seen in Figure 3.13a or zoomed in Figure 3.10. Also it can be seen in Figure 3.14(c,d) from the azimuth vs. velocity plot that the direction of the

large scale disturbances is consistent with the direction of propagation of the umbra. This continuity of the transition between MSTIDs and the LSTIDs and vice versa can be observed in both networks. As for the LSTIDs propagation (Figure 3.13a at 17:15 UT), the disturbances follow the lines of iso-penumbra and propagate in the direction of the movement of the eclipse, except at the east edge of the continent, where the angle varies slightly, perhaps due to propagation delay. Around 18:00 LSTIDs with similar behavior appear, with a greater opening angle (i.e. the angle between two branches of the bow wave), and a direction that follows the movement of the umbra, see the more details in Section 3.5.4.

The complementary behaviour is shown in Figure 3.13a at 18:45 UT, where we observe the disturbances that appear when the umbra is over the west coast. In this case we observe LSTIDs to the west of the umbra that follow the shape of the lines of iso-penumbra, with wavelengths that increase slowly from 700 km to 1300 km. In addition, at the same time, MSTIDs of less wavelengths, propagate with a front waves with a curvature of opposite sign. These MSTIDs have a wavelength of about 200 km, and on the map appear as ripples that can be observed at the west of the umbra. This transition can be seen more clearly in the zoom in Figure 3.11a, and the azimuth vs. velocity plot of Figure 3.11(b,c), shows that the perturbations propagate in opposite direction to the propagation of the umbra. In Section 3.5.5 the MSTIDs which correspond to the ripples are explained in detail.

3.5.4 Description of the Large Scale Ionospheric Perturbations Related to Variable Angle Bow Waves

In this section we extend the characterization done in Section 3.5.3 of the behaviour of the large scale ionospheric disturbances (i.e., LSTIDs) during the eclipse transit. The behaviour of the LSTIDs during the eclipse is summarized in Figure 3.14, in which we show time-aligned: (a) wavelength path (Figure 3.14a, 3.14b) and (b) velocity vs. azimuth polar plots (Figure 3.14c, 3.14d). This diagram will allow us to understand the relationships between these characteristics throughout the eclipse transit.

The LSTIDs shown at Figure 3.14(a,b) have similar wavelengths and velocities as the typical large scale TIDs (Tsugawa, Saito, and Otsuka, 2004). However, the directions as shown at Figure 3.14(c,d) are different, following the azimuth of the umbra percent, which is denoted in the polar plots with red stars.

Before the arrival of the eclipse to the continent, the LSTIDs exhibited a quiet behaviour, characterized by low amplitude and propagation mainly in the equator-east direction. The duration of the disturbances was less than 15 min, the speed was low, about 100–200 m/s, and with long periods in the order of 1.5–2 h. At about 15:56

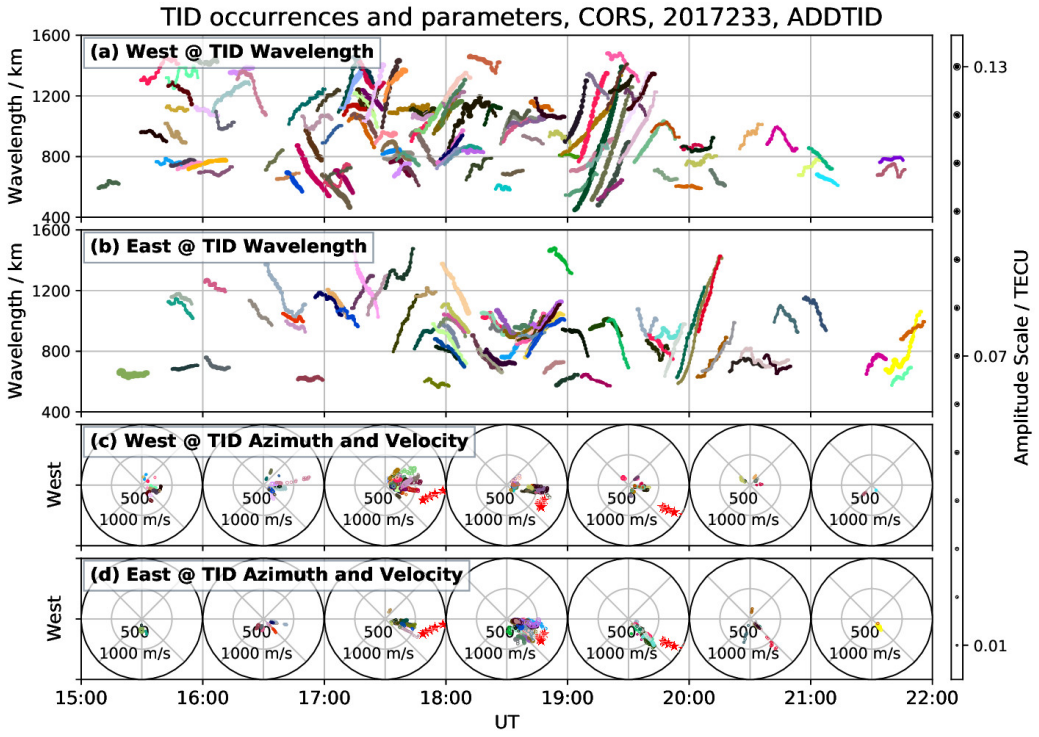

FIGURE 3.14: Behavior of the LSTIDs during the transit of the eclipse (Time aligned). (**a**,**b**): time evolution of the wavelength of the LSTIDs, (**c**,**d**): Azimuth vs. velocity polar plots at intervals of one hour, red stars for the azimuth vs. velocity of umbra. The dot color and size (right bar) coding follows the convention in Figure 3.10.

UT, the penumbra arrives first at the ionosphere 250 km above the west coast of US. From then on, the penumbra increasingly covers this region. At the same time the number of LSTIDs increases. During the time interval 16:10–17:15 UT, when the 10% iso-penumbra line reaches the western US, the properties of the TIDs change. The LSTIDs now head eastwards, with a marked increase in the speed (over 500 m/s). The wavelengths of the LSTIDs, decrease from about 1500 km to 800 km, and then increase above 1200 km. Please note that the delay between the west and east US, in terms of the evolution of LSTIDs, is approximately half an hour, which is consistent with the delay due to shadow propagation. This delay was computed from the shape of the wavelength trajectory observed in the figure, in particular from the position of the minimum of the parabola that is repeated at each coast.

At about 17:15 UT, a large number of LSTIDs suddenly appear, a couple of minutes after the umbra arrives the west US. In the west network between 17:15 UT and 18:05 UT (about 18:05 UT, the umbra leaves to the west part of US), the wavelength path of the LSTIDs shows a parabolic shape. The edges of this trajectory are determined

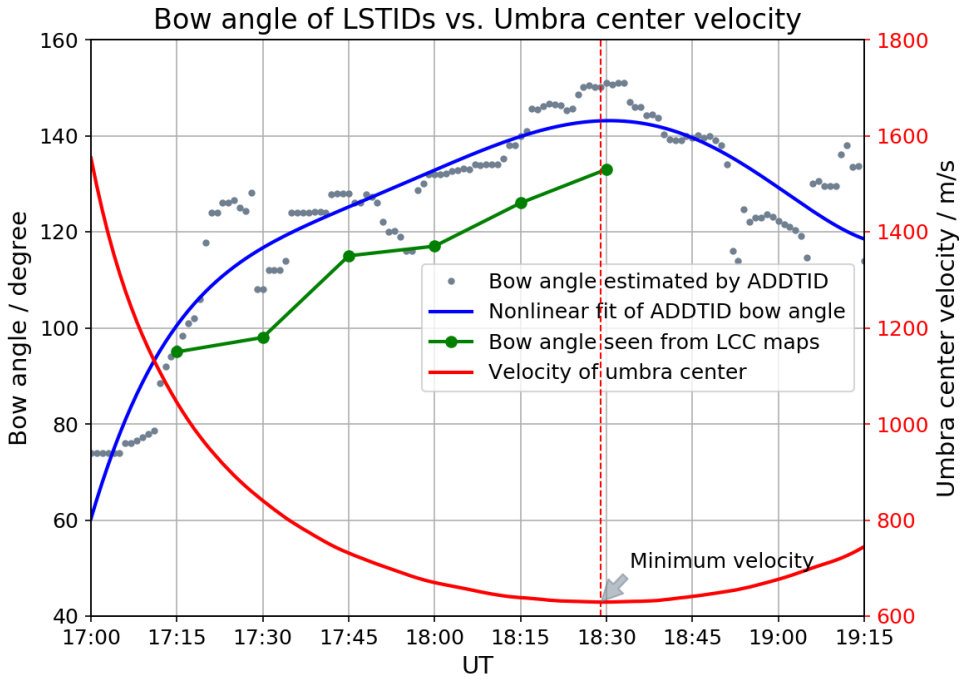

FIGURE 3.15: Time evolution of bow opening angle vs. the velocity of the umbra. Grey dots represent the estimated opening angle by ADDTID. The blue line is the nonlinear fit of the estimated opening angle. The green line for visual estimation of the opening angle from the Lambert Conformal Conic projection (LCC) maps, and red line for the velocity of umbra. Red dashed line pointing the time when the umbra velocity reaches minimum.

by the entering and leaving phase of the penumbra (see comments in Section 3.5.1). The disturbances show an eastward propagation, with an azimuth scattering of 60 degrees and a speed range between 300 and 700 m/s.

In the velocity-azimuth diagram, the points associated with the bow wave are distributed in a fan shape, which corresponds to an opening angle of the bow of 120 degrees, and a propagation with an azimuth of 10 degrees. This fan also indicates the speed of each of the branches of the bow. The bow wave follows the path of the umbra, which at this moment has an azimuth of roughly 10 degrees south east and a velocity in the range of 1500–670 m/s in Figure 3.14c.

After leaving the western network, the activity of the LSTIDs gradually weakens until they disappear. A similar behaviour with a time delay is visible in the eastern network. However, there are differences in the distribution and properties of LSTIDs on the east coast compared to those on the west coast. When the umbra covers part of the eastern subnetwork between the 18:05–18:50 UT, the angle of opening of the bow wave increases to about 135 degrees, while the umbra speed decreases to 650 m/s. At this time, the bow wave in the eastern subnetwork shows a global

deviation of 30 degrees south, which is compatible with the azimuth changes of the umbra movement. Please note that the direction of propagation of the bow wave, along with the two branches of the bow, follows the movement of the umbra, with a deviation in azimuth. This deviation is about 10 degrees north east at 17:00–18:00 UT, and about 5 degrees south east at 19:00–20:00 UT. The low activity of the geomagnetic field has little influence on the movement of the ions, so the deviation may be due to the variation in the eccentricity of the ellipses resulting from the penumbra, and to the rotation of the ellipse axes. The deviation and lines of equal obscuration can also be seen on the TID activity maps.

In Figure 3.15, we show the relationship between the opening angle of bow wave with the velocity of the umbra. The figure shows in green the measurement made by visual inspection on the maps and in grey the estimation using the ADDTID algorithm, and also in blue a nonlinear fit of the ADDTID opening angle to smooth the estimation errors. The manual measurement on the maps was performed prior to the measurement obtained from the ADDTID algorithm. This confirms that the ADDTID algorithm can detect wavefronts and matches the approximate measurements manually estimated. The order of the measurements is methodologically correct, as it avoids biases due to having observed first the output from the algorithm. This order is justified, was because once the manual measurement was performed, a posteriori check by means of the ADDTID was made to confirm whether the manual measurement was correct. The velocity of the umbra is computed by the algorithm of Montenbruck and Pfleger (2013), and the time evolution follows a concave up parabolic shape. During the transit over the CORS network, the part corresponding to the highest acceleration of the umbra was located outside the network. Please note that, as the velocity slows, the degree of opening of the bow wave increases for both two measurements. The moment when the umbra velocity reaches a minimum is about 18:29 UT (see the mark in Figure 3.15), which coincides with the moment when the iso-penumbra line of 0% is completely within the territory of the United States. The decrease in the opening angle of the bow wave observed with about 3–5 min delay, is due to the increase in the speed of the umbra. The estimated opening angle shows a higher noise from 19:00 UT on, when the umbra has already left the continent and is now on the Atlantic Ocean, and thus the two arms of bow waves of LSTIDs are not completely observed by CORS network any more, as shown in Figure 3.11. Therefore the measurement by means of visual inspection is reliable only until 18:30 UT. The LSTIDs corresponding to the measurements in Figure 3.15 show the small delay with respect to the umbra, and propagate at a speed greater than the speed of sound in the middle atmosphere. Both these two characteristics are consistent with the findings in Coster et al. (2017) and Zhang et al. (2017). This behaviour does not correspond to the gravity waves induced by the eclipse in the

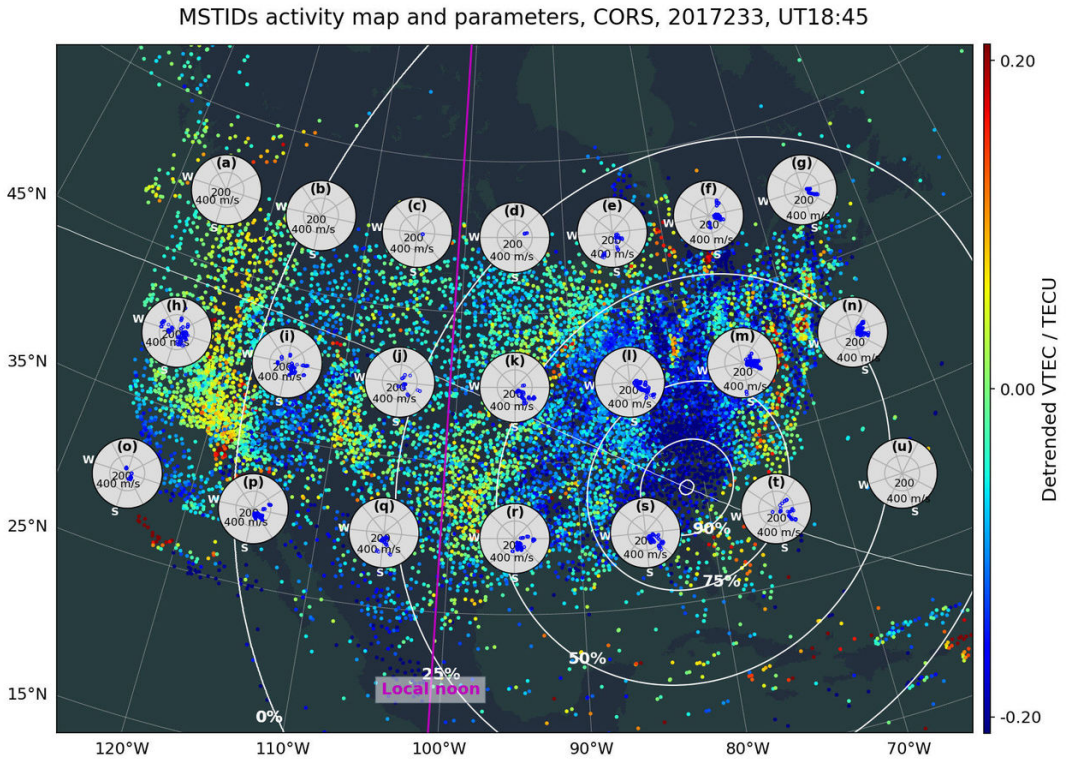

FIGURE 3.16: TID activity at 18:45 UT. Grid of the azimuths (in degree) vs velocities (in m/s) of TID estimated inside subnetworks of $10^\circ \times 10^\circ$ longitude - latitude. Each subplot is labelled with a letter at the top. In white, iso-penumbra lines at percentages that range from 0% to 100%. The magenta line shows the local noon meridian at height of 250 km.

middle atmosphere (Chimonas and Hines, 1970a), but to the shock waves generated in the thermosphere, with a speed compatible with the acoustic velocity (Sun et al., 2018).

3.5.5 Variable Angle Bow Wave Consisting of MSTIDs Induced by Eclipse

As mentioned in the previously, at around 17:15 UT, several large-scale disturbances cover the entire continent, and the large-scale disturbances are present during the whole transit, including an overlap with different local MSTIDs. This can be seen in Figure 3.13a, which shows the fluctuation of the detrended VTEC. As it can be seen in Figure 3.13(b, c), TID wavelengths range from hundreds to thousands of kilometres. From the maps measured between 17:15 UT and 18:00 UT, the wavefront near the umbra displays a V-shaped wedge shape, with an opening angle that increases with time. Also large-scale disturbances can be seen in advance of the umbra. The distribution over time of the disturbances on the continent can be regarded as the superposition of non-concentric circular waves of different radii. In addition,

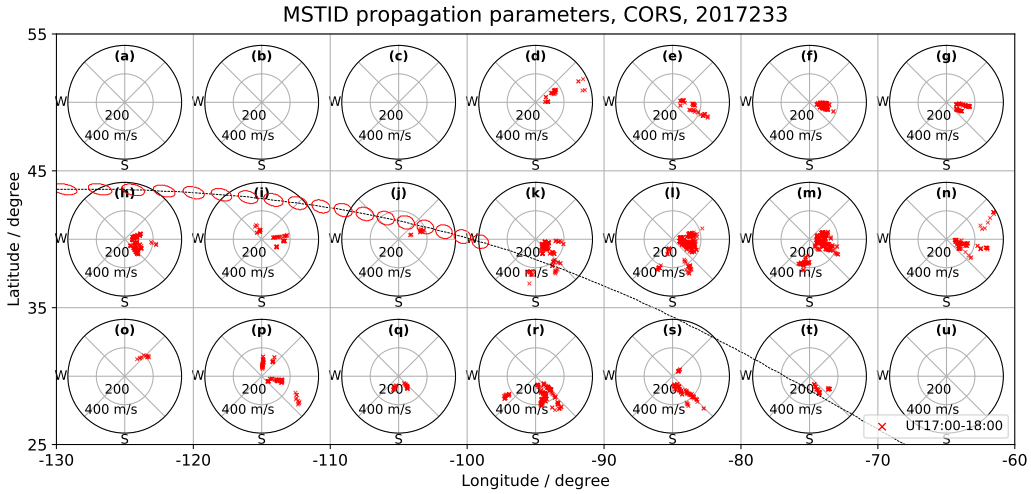

FIGURE 3.17: Grid of polar plots of MSTIDs in 17:00–18:00 UT (in red color) superimposed over the US CORS network. The network is divided into $10^\circ \times 10^\circ$ longitude-latitude cells. The trajectory of the umbra is marked by a series of ellipses, one every three minutes.

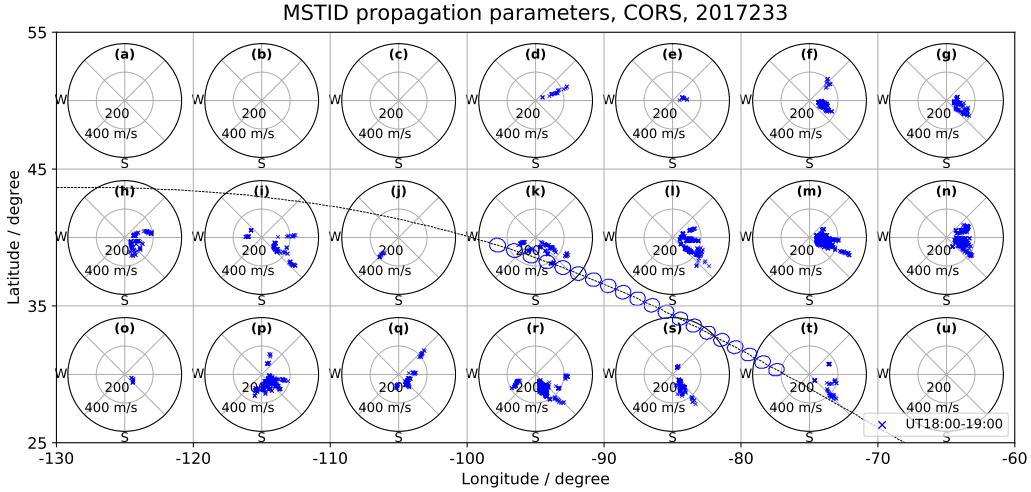

FIGURE 3.18: Grid of polar plots of MSTIDs in 18:00–19:00 UT (in blue color), organized as in Figure 3.17.

the ripples are observed to the left of the umbra in the 18:45 UT map (see Figure 3.13a). These ripples were detected automatically by the ADDTID algorithm and the wavelength (see Figures 3.13b and 3.13c) and azimuth estimation coincide with the measurements made over the map.

To give a more complete description of the bow wave and the ripples at the west of the bow, we will introduce geodetic information by overlaying, on top of the map, local azimuth vs velocity plots computed at $10^\circ \times 10^\circ$ grids of latitude-longitude. The size of the grids is more than two times larger than the typical wavelengths of

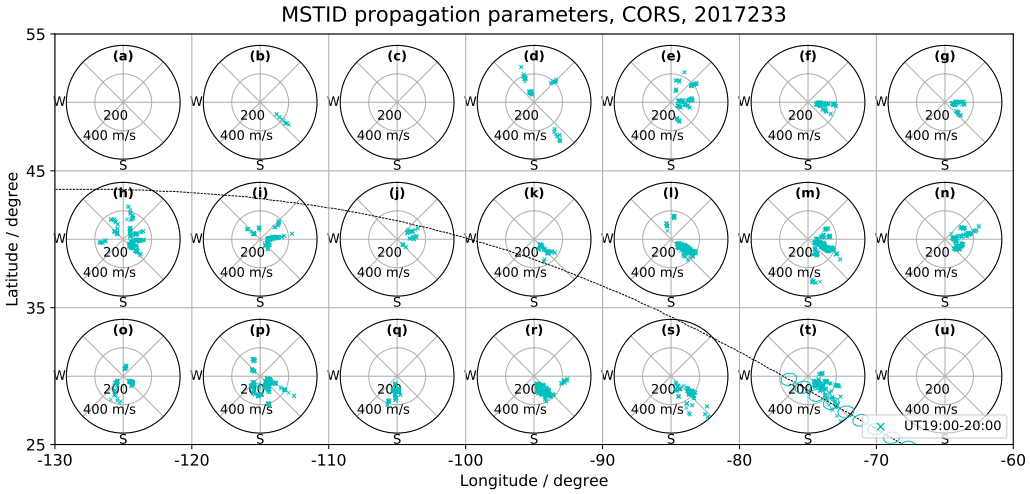

FIGURE 3.19: Grid of polar plots of MSTIDs in 19:00–20:00 UT (in cyan color), organized as in Figure 3.17.

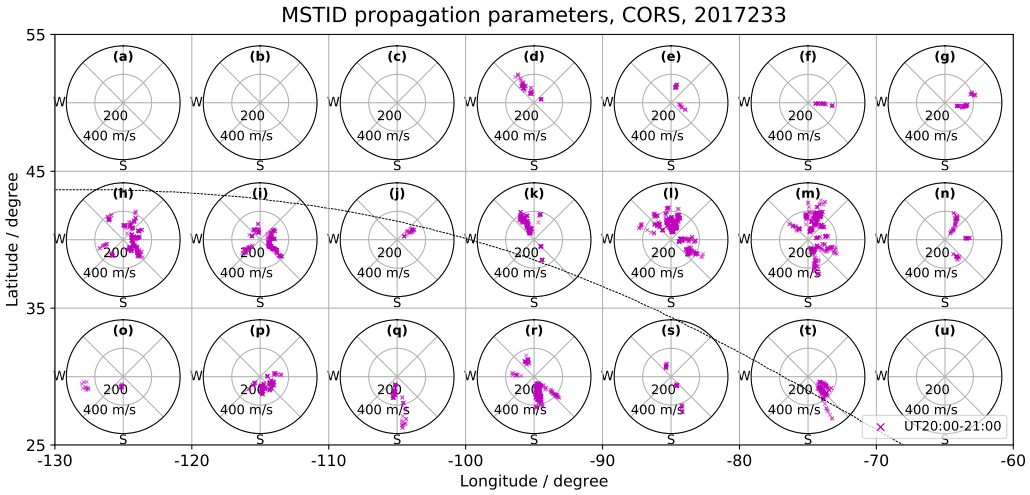

FIGURE 3.20: Grid of polar plots of MSTIDs in 20:00–21:00 UT (in magenta color), organized as in Figure 3.17.

MSTIDs. The size of this grid of plots assures that the plane wave approximation done in the ADDTID will be valid,see for instance the detection of circular wave by an approximation by means of a planar wave model in Yang, Monte-Moreno, and Hernández-Pajares (2017).

Since the MSTID characteristics vary in time and space (see detection in Section 3.5.3), an analysis was performed in a grid, as shown in Figure 3.16 and Figures 3.17–3.21. These grids show the local direction of the MSTIDs that appear as waves in the penumbra area behind the umbra, which as discussed in the previous section, could be originated by the acoustic gravity waves in the middle atmosphere.

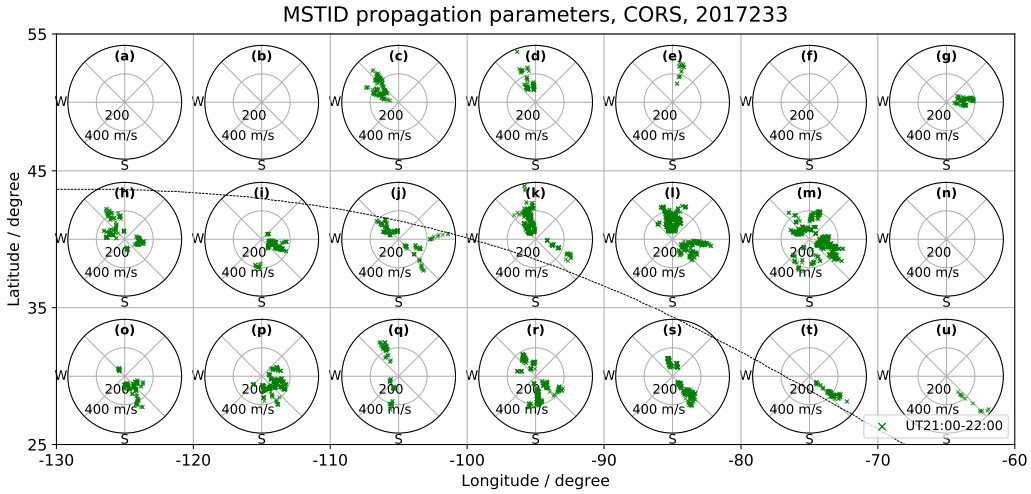

FIGURE 3.21: Grid of polar plots of MSTIDs in 21:00–22:00 UT (in green color), organized as in Figure 3.17.

Figure 3.16 shows at 18:45 UT the overlap of the detrended VTEC map, with the azimuth versus velocity diagrams of the locally detected MSTIDs. In the lower right of the map, is clearly visible the shape of the bow wave from the thermosphere. On the other hand, the ripples appearing in the regions covered by penumbra greater than 50% and with a delay of tens of minutes behind the umbra are compatible with the description given at Chimonas and Hines (1970a). The azimuth vs velocity plots adjacent to the ripples labeled (upper part) with the letters (e), (k), (l), (r) and (s), clearly show the propagation azimuths of the ripples which could be the short period components of the bow wave originated from middle atmosphere, see the similar reports for the long period components at the final eclipse stage in Section 3.5.1. The dominant velocity is in the range between the 200 m/s and 350 m/s. Furthermore, the azimuth vs velocity polar plots on the east side of the umbra, such as (f), (g), (m) and (n), show medium scale disturbances in advance of the umbra, with azimuths compatible with the lines of iso-penumbra, which could be the time-varying ionospheric waves generated in the ionosphere, see the previous description of the early eclipse stage in Section 3.5.1.

Another way to analyze the middle scale ionospheric disturbances due to eclipse transit is by means of the diagram shown in Figures 3.17–3.21, where we show a grid of azimuth vs. velocity diagrams, ordered geographically, in which disturbance detection is done locally inside each $10^\circ \times 10^\circ$ section. In contrast with Figure 3.16, where we show a snapshot at 18:45 UT, in Figures 3.17–3.21 we show all the detected MSTIDs in the interval 17:00–22:00 UT, which includes the whole transit above US and in two hours after the transit. In the figure we also show the eclipse path superimposed over the azimuth vs. velocity diagrams. The path is marked by means

of elliptical to circular shapes spaced temporally at the 3 min intervals. Please note that in each interval of one hour, the color is the same, but the shape has been designed so that it follows the area of the umbra. Therefore, the shape changes from highly elliptical at the upper left of the plot to almost circular at the bottom right, reflecting the inclination of the shadow of the moon with respect to the earth, simultaneously with the position over the continent. The color code that has been used in the azimuth vs. speed graphs follows the code represented in the path, so it can be seen how the umbra at any given time affects the entire US region. Please note that each azimuth vs. velocity diagram is labeled by a letter at the top. The figure shows the MSTID activities in each subdivision of the US CORS network when the umbra passes over the ionosphere at an altitude of 250 km.

Next, we will analyze by means of this figure, the distribution of the MSTIDs for each interval in which the path has been divided.

In the early interval (17:00–18:00 UT), the detected MSTIDs (coded in red), show patterns that differs across the entire network. During this interval, in Figure 3.14, one can observe a bow wave consisting of LSTIDs along the supersonic umbra. However, as for MSTIDs in Figure 3.17, no bow wave is detected along the umbra trajectory, just an irregular activity in the lower part of the trajectory and no detectable activity in the upper part. Meanwhile, in advance to the umbra and geographically more to the east (see subfigures (d) and (k) corresponding to the east part), we detected MSTIDs that show two partial branches of a bow-shaped disturbance, with azimuth angles of 50–70 degrees on the north side and 100–160 degrees on the south side, giving an angle of about 90–100 degrees, which is compatible with an advance response to the southeastward umbra. All these MSTIDs have speeds in the range 150–250 m/s, wavelengths of about 180–250 km, and periods of about 20–50 min. This bow wave in advance of umbra, which appears with transient delay of the penumbra, could originate from the thermosphere, as explained in Section 3.5.1.

During the middle stage when the umbra passes across US (18:00–19:00 UT), the MSTIDs (coded by blue triangles) appear in most of grid subplots. The MSTIDs in eastern subplots show a behavior consistent with the bow wave at the early stage. However, the western part and the part around the transit with southeastward direction (azimuth angles of 45–225 degrees), there are the partial wavefronts of the circular waves as ripples in the penumbra area, see Figure 3.16. These southeastward MSTIDs approximately pointing at the transit of umbra, seen from Figure 3.18, have the following features: 100–300 m/s velocity, 200–400 km of wavelengths, and 30–70 min of periods, with a delay of more than tens of minutes with regard to the umbra. These MSTIDs show compatible propagation parameters with Nayak and

Yiğit (2018). The origin of these MSTIDs (Chimonas and Hines, 1970a) could be the middle atmosphere by way of short period components of bow wave.

At the final stage of the eclipse above US (19:00–20:00 UT) in Figure 3.19, the umbra is leaving from the continent, the delayed MSTIDs show an disperse azimuth distribution of the estimated parameters in the grid regions, such as (h), (i), (o), and (p). Besides most MSTIDs with southeastward directions, the other parts with similar velocity distribution but propagate to the northwest. Please note that the northwest MSTIDs show wavelengths greater than 350–550 km and periods longer than 60–100 min. These northwest MSTIDs have larger scales than the southeast waves. These patterns continue for two hours after the ionosphere above US the umbra has leaved the continent (20:00–22:00 UT, i.e., 14:00–16:00 LT, see Figures 3.20 and 3.21), when the MSTIDs, particularly in the central subnets of US, show omnidirectional azimuths as potential clues of circular waves. MSTIDs in the north subfigures show the northward propagation. The distribution of wavelengths and periods of these MSTIDs shows consistent characteristics within the interval of 19:00–20:00 UT, i.e., the full northwestward (westward / northwestward / northward) MSTIDs have larger wavelengths and longer periods than the full southeastward (southward / southeastward / eastward) MSTIDs. The full northwestward MSTIDs would be the long period component of the bow wave, and the full southeastward MSTIDs might be the short period component of the bow wave, which originates from the middle atmosphere (Chimonas and Hines, 1970b). Furthermore, as for the long period components of bow waves, the northwestward MSTIDs appear approximately 1.5–3 h after the umbra departure, compared with about 30–60 min delay of the short ones.

3.5.6 Early MSTIDs at the East Coast, before the Penumbra Reaches the West Coast

In Figure 3.22 we show the presence of MSTIDs, which indicates a behaviour that differs from that of the typical summer season. The propagation of normal MSTIDs of this season occurs in this season of the year during the night, following a west/polar-west/equator-west direction, while the presence of MSTIDs during the day is almost non-existent, see Hernández-Pajares et al. (2012b). As shown in the polar diagrams, there are two groups of MSTIDs propagating in an eastward direction, with a low intensity between 0.04–0.06 TECU. The map at the top right shows the local noon by means of a magenta line. Note both of the MSTIDs exhibit steady behavior with regard to wavelength and azimuths between 15:40 UT (∼10:10 LT) and 17:30 UT (∼12:00 LT). The effect of the solar terminator is very weak at this moment. These MSTIDs indicate two clear directions of propagation one towards the equator-east,

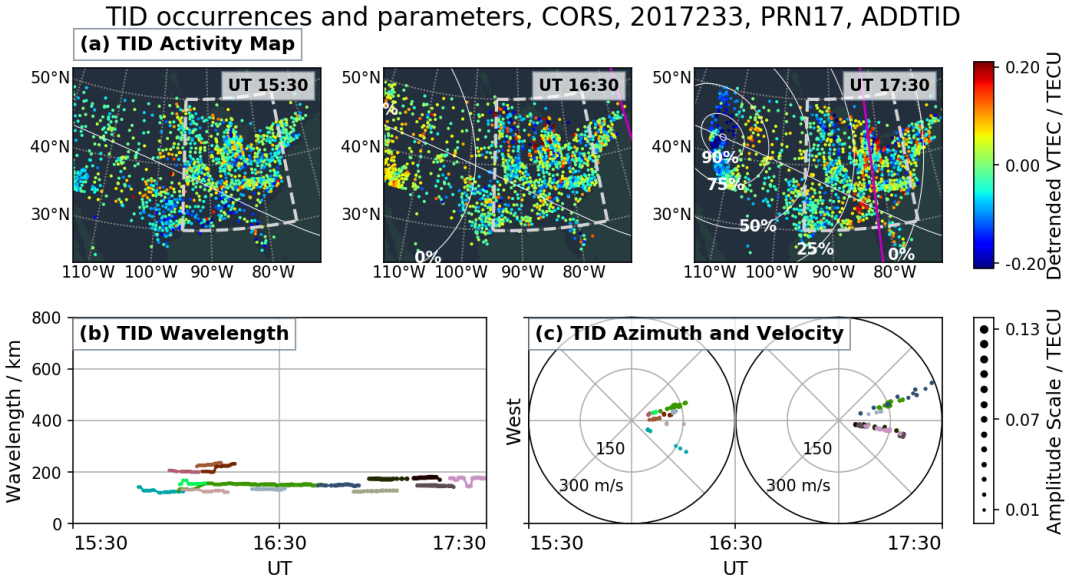

FIGURE 3.22: MSTIDs, over the eastern US, with propagation in the east direction. (**a**) Detrended VTEC maps (in TECUs), where the MSTIDs are visible for three snapshots at 15:30 UT, 16:30 UT and 17:30 UT, (**b**) Time evolution of the MSTID wavelengths of the subnetwork in white dashed rectangular, (**c**) Polar plots at intervals of one hour for MSTID azimuths vs. velocities, organized as Figure 3.10.

and the other in a polar-easterly direction. It is interesting to note that the polar-east direction is present during the whole interval. Please note that the effect of the magnetic field in the horizontal direction is small, because the azimuths are almost perpendicular to the geomagnetic lines. An explanation of why the MSTIDs are so seldom, and difficult to detect during daytime at summer, is given by Kotake et al. (2006), that point out the upward acoustic gravity waves as the potential origin of the daytime MSTIDs. This is because the disturbances cannot propagate through the region of the steep temperature gradient near the mesopause in summer, thus the possibility of gravity waves causing MSTIDs would be further decreased at local noon.

One possible interpretation of the polar diagram (Figure 3.22c) would be that each of the propagation directions actually corresponds to the plane wave approximation of each of the arms of a soliton wave that advances ahead of the shock wave which originate from the thermosphere.

3.6 Summary

In this work we have described the diverse types of ionospheric disturbances that were generated during the US solar eclipse of 21 August 2017, and presented the detection done by means of the ADDTID algorithm, with a visual contrast with VTEC maps for each of the results from the algorithm.

Chapter 4

TID Characterization during Japan Tohoku-Oki Earthquake & Tsunami of 11 March 2011

4.1 Introduction

In this section we aim at analyzing the relationship between tsunamis and TIDs using the algorithm developed in this thesis. In this characterization we will compare the detrended VTEC maps with the estimates given by the algorithm in order to determine the strengths of the algorithm and the points at which the algorithm may have lower performance. As will be shown, the condition in which the algorithm does not detect a particular type of wave is very specific and can be easily corrected. Note that the algorithm is able to detect the tsunami interaction with the atmosphere automatically, without human intervention. Therefore, the comparison between maps and ADDTID measurements, is used to corroborate the properties of the latter. In addition, the main advantage of this method is the possibility of obtaining a local estimate of parameters such as azimuth, wavelength, velocity and period, which are difficult to estimate from the VTEC maps or Keograms.

In addition, in order to be able to distinguish more clearly the properties of the gravity waves and the acoustic waves, we did the analysis with two different detrending lags, i.e. 60-sec interval of double difference, and 300-sec interval of double difference. In summary,

- First we present a visual description of the phenomena by means of detrended VTEC maps and keograms (see section 4.5 for the case of Detrending Filter @ 300 sec and 60 sec Double Difference).

- Next we perform an automatic analysis of the disturbances detected by the ADDTID method, showing locally the velocity, azimuth, intensity, and wavelength. (see section 4.6 for the case of Detrending Filter @ 300 sec and 60 sec Double Difference).

In the context of this thesis, we can cite as antecedents the following articles. The relationship between tsunamis and ionospheric disturbances was first reported by Hines (1972), who suggested that the ionospheric signature could be employed as an early warning of the occurrence of a tsunami. The displacement of the atmosphere on the sea surface induces atmospheric waves that then propagate up to the thermosphere and subsequently generate amplified perturbations in the ionosphere, hence the relation between TIDs and tsunamis. The model proposed by Peltier and Hines (1976) shows that the ionospheric signature of gravity waves is detectable in the form of TIDs, which has been confirmed empirically as the TIDs associated with tsunamis have been observed and researched for many years.

As an example of this effect, Artru et al. (2005a,b), the Japan GEONET GNSS network, clearly detected the small scale ionospheric disturbances resulting from gravity waves generated from a tsunami. This tsunami was triggered by the Mw 8.2 earthquake in Peru took place in June 23, 2001, and reached Japan 22 hours later. The ionospheric disturbances observed above Japan show the similar time delay after the earthquake and the compatible propagation parameters with the tsunami.

Another case in point is the Sumatra Mw 9.3 earthquake of 26 December 2004. This was analyzed by Liu et al. (2006), where the authors reported the presence of significant observational results of tsunami-driven ionospheric signatures caused by the perturbations on the TEC and also give theoretical backgroud of the possible causes. The interest of this work regarding the contribution of this thesis is that the results were obtained from a small number of GPS ground-based receivers in the Indian Ocean area. In addition to the above mentioned report, Lee et al. (2008) measured the ionospheric plasma dynamics, in particular the TIDs related to the tsunami, by the combined observations of the 430 MHz incoherent scatter radar and GNSS. They suggest that coupling at the tsunami sea-atmosphere interface launched gravity waves that propagated for great distances beneath the mesopause and conclude that TIDs were induced on a global scale at the wake of tsunami-launched gravity waves. These results are backed up by the study carried out by Occhipinti et al. (2006) who simulate the ionospheric disturbances by means of the 3D model of ocean-atmosphere-ionosphere coupling and show the overall consistency compared with TEC measurements from Jason-1 and Topex-Poseidon satellite altimeters. In Occhipinti, Kherani, and Lognonné (2008), the authors propose a 3D model for explaining that the observation of electron density perturbation dependency on the

latitude variation is driven by the Earth's magnetic field. In this work the authors also point out that high density coverage of the GNSS receivers can help the data analysis comparing the coherence of the ionospheric perturbation with the tsunami propagation. Another model that supports the relationship between tsunami and ionospheric disturbances is that of Mai and Kiang (2009), which presents a model to analyze the electron density perturbation caused by tsunami-induced gravity waves, considering the loss mechanisms of thermal conduction, viscosity, and ion drag in deriving the dispersion relation of the atmospheric gravity waves. In this model, the authors analyze the electron density perturbation of the same tsunami event and find that the atmospheric gravity waves move horizontally at the same speed with that of the tsunami, and are trapped at about 400 km high.

An article that focuses on the propagation of tsunami-driven gravity waves into the thermosphere and ionosphere is Hickey, Schubert, and Walterscheid (2009), where the authors propose an atmosphere-ionosphere-coupling model that relates the neutral atmosphere response, the electron density response, and the TEC response to a gravity wave packet propagating through the atmosphere. The authors point out that the ion and electron response to a gravity wave is smaller for zonal wave propagation, while the electron density and TEC fluctuations are almost two orders of magnitude larger for meridional wave propagation.

Rolland et al. (2010) reported the detection of ionospheric disturbances hours after an earthquake triggered a transpacific tsunami event. This was done from the measurements of the dense GNSS network Hawaii, which consists of tens of receivers.

The 2015 Illapel earthquake occurred 46 km offshore from Chile Illapel on September 16, with the magnitude of 8.3, also generated a local tsunami of 4.7 meter height. By means of tens of receivers from Centro Sismológico Nacional (CSN) and International GNSS Service (IGS) network, Reddy et al. (2017) report the characteristics of ionospheric perturbations induced by shock acoustic waves of the earthquake / tsunami, proving the advantages of GPS observation networks in imaging tsunami-driven ionospheric perturbations. Nevertheless, from this data it is difficult to discern the ionospheric TEC perturbations caused by Rayleigh waves or/and tsunami under the observations. Grawe and Makela (2017) show ionospheric perturbations appearing in filtered GPS-derived TEC and 630.0 nm airglow above Hawaii during the passing of the 2015 tsunami in Illapel, Chile, and report the parameters of the internal gravity waves from the two observations using a combination of prior methods and developed method of a Gabor filter bank which could be potentially a real time monitoring system of the tsunami.

The analysis that we will carry out in this chapter refers to the Japan Tohoku-Oki tsunami in 2011, which occurred in the Pacific ocean, giving rise to a maximum

height of 40.5 meters. It was triggered by an undersea megathrust earthquake off the north-east coast of Japan, with a magnitude of 9.1, which occurred at 05:46 UT on Friday 11 March 2011 (the 80th day of 2011). This tsunami generated ionospheric perturbations that were recorded by more than 1200 GNSS receivers of the Japan GEONET network. By employing this high-resolution network, Liu et al. (2011a) and Rolland et al. (2011) observed the multiple TIDs in form of the circular wave fronts, distinguished into different patterns of the atmospheric gravity waves such as the signature of seismic Rayleigh waves and tsunami-driven acoustic gravity waves, and demonstrated the GPS network can be a powerful tool to supply the warning signals of tsunamis. In order to explain the origin of the ionospheric disturbances, Saito et al. (2011) show that in the vicinity of the epicentre, a two-dimensional structure of short period perturbations of the ionosphere is generated by the acoustic resonance between the ground surface and the lower thermosphere. Similarly, Tsugawa et al. (2011) show the details of the ionospheric disturbances after the earthquake. These disturbances follow concentric waves indicating the common point source which is not compatible with the epicenter. The authors point out that the concentric waves are induced by three kinds of patterns of atmospheric waves such as: acoustic waves generated from a propagating Rayleigh wave, acoustic waves from the ionospheric epicenter, and atmospheric gravity waves from the ionospheric epicenter. Although there is not a clear coupling model to explain the relationship between ionospheric disturbances, earthquakes and tsunami, there are empirical signs that relate both phenomena. Regarding the Tohoku-Oki seism-driven tsunami of March 11, 2011, the observation data also obtained from the GEONET network allowed for a comparison between the detection of ionospheric disturbances and the earthquake magnitude estimated by atmosphere-ionosphere coupling model as explained by Hickey, Schubert, and Walterscheid (2009). Also the speed of atmosphere gravity wave based on the tsunami computed by sea-surface height model from Song et al. (2012) has been presented in Galvan et al. (2012). The results show a very high similarity between the observed VTEC variation and the prediction based on the atmosphere-ionosphere coupling model. In addition, the ionospheric observations with sea-surface height model seem to be high correlated with the velocity of the ocean tsunami. This indicates that the tsunami created by the earthquake has also generated a series of major ionospheric disturbances. Nevertheless, it is still uncertain whether or not the atmosphere gravity waves that are related to the ionospheric disturbances are generated both by the earthquake and tsunamis. The time lag between the observation of the ionospheric perturbations induced by Raleigh and acoustic waves during the earthquakes, and the co-seismic ionospheric disturbances, is reported by Galvan et al. (2012).

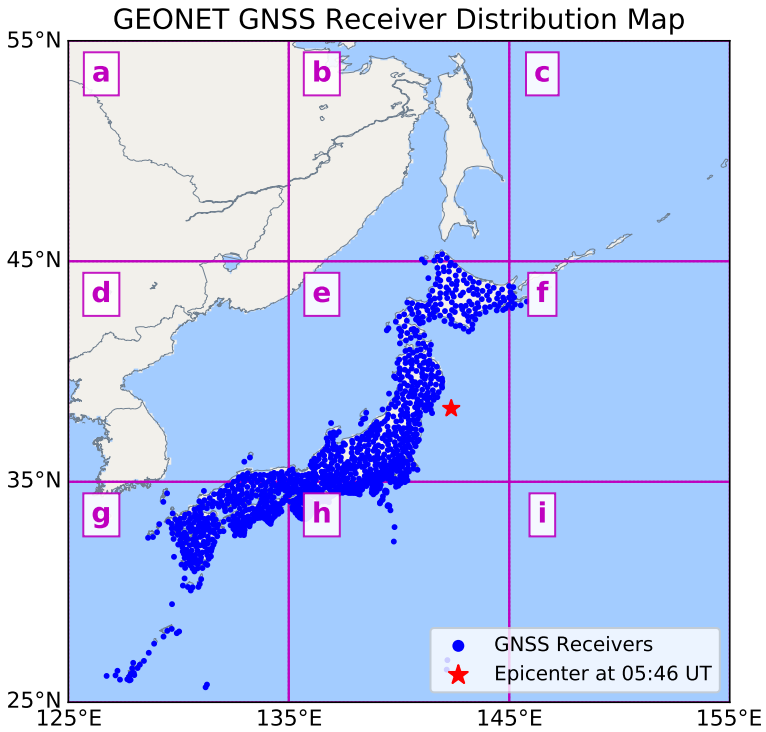

FIGURE 4.1: GNSS receivers distribution of GEONET in Japan. Blue dots denote the location of the GNSS receivers, the red star denotes the epicenter at the time of 5:56 UT, on the 70th day of 2011. The grids in magenta (**a**–**i**) denote the 9 subnetworks consisting of the geographical grid of $10^\circ \times 10^\circ$.

As an alternative way of measuring the perturbations, Maruyama et al. (2011) report the similar disturbances of ionosphere by means of the ionosonde stations. Matsumura et al. (2011) simulate the atmospheric perturbations observed at ionospheric heights during the tsunami, and point out the ionospheric disturbances are mainly due to the motion of the neutral atmosphere. Makela et al. (2011) present the Japan tsunami signature of airglow located at Hawaii, associated with GPS measurements of the ground-based GPS receivers and the Jason-1 satellite. Occhipinti et al. (2011) use the ocean-atmosphere coupling to reproduce the tsunami signature in the same airglow and clearly show the shape of the modeled internal gravity waves.

Finally, with the algorithm developed in this thesis, the ADDTID, the author was able to determine tsunami-driven TIDs, see Yang, Monte-Moreno, and Hernández-Pajares (2017). The multi-TIDs characterization tool, in contrast with other methods that require visual inspection, automatically detects partial circular fronts of TIDs which could correspond to small-scale earthquakes / tsunamis in Japan on 2011.

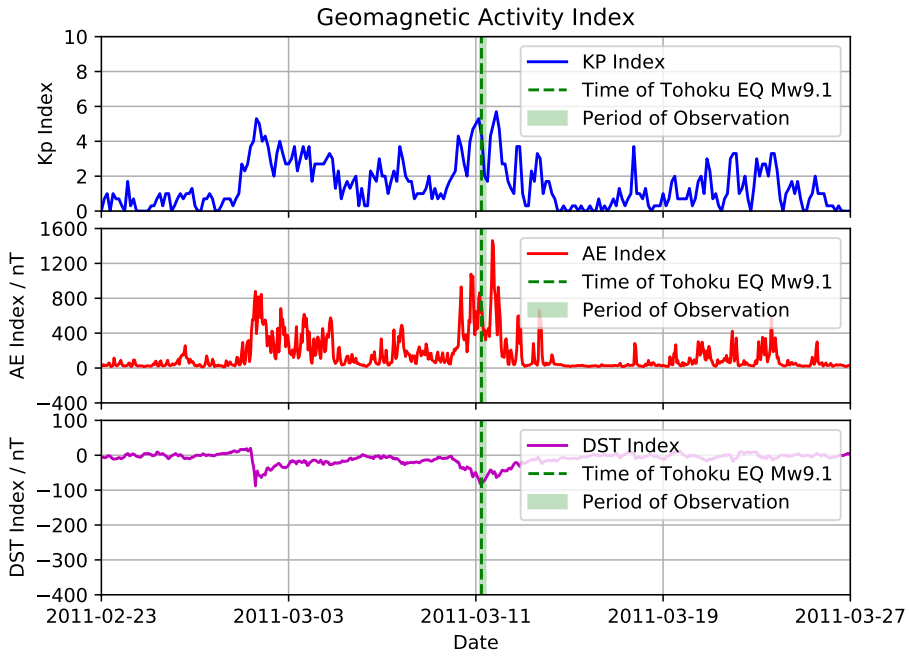

FIGURE 4.2: Geomagnetic Activity Indices, blue line for planetary 3-hour range index (Kp), red line for Geomagnetic Auroral Electrojet (AE) index, magenta line for Geomagnetic Equatorial Disturbance Storm Time (DST) index.

The magnitude in this case was less than 5, see more details in Chapter 1 and 2. In this chapter, we study and describe the behaviour of TID evolutions during the 2011 Tohoku-Oki Earthquake / Tsunami, by means of the ADDTID.

4.2 Observational Data of GNSS network

The data we use in the study are from the GEONET network, which consists of about 1200 GPS stations densely distributed in Japan, see Figure 4.1, and the similar description in chapter 2.2. Note in the figure the location of the epicenter, and the partition of the stations in a $10^\circ \times 10^\circ$ grid.

4.3 Space Weather and Selection of IPP Height

In Figures 4.2 and 4.3 we summarize the Solar and Geomagnetic Activity on the 70th day of 2011 (March 11), wherein it is shown a low activity with no significant disturbances originated by these phenomena such as major solar activities, solar flares, derived from U.S. NOAA National Centers for Environmental Information

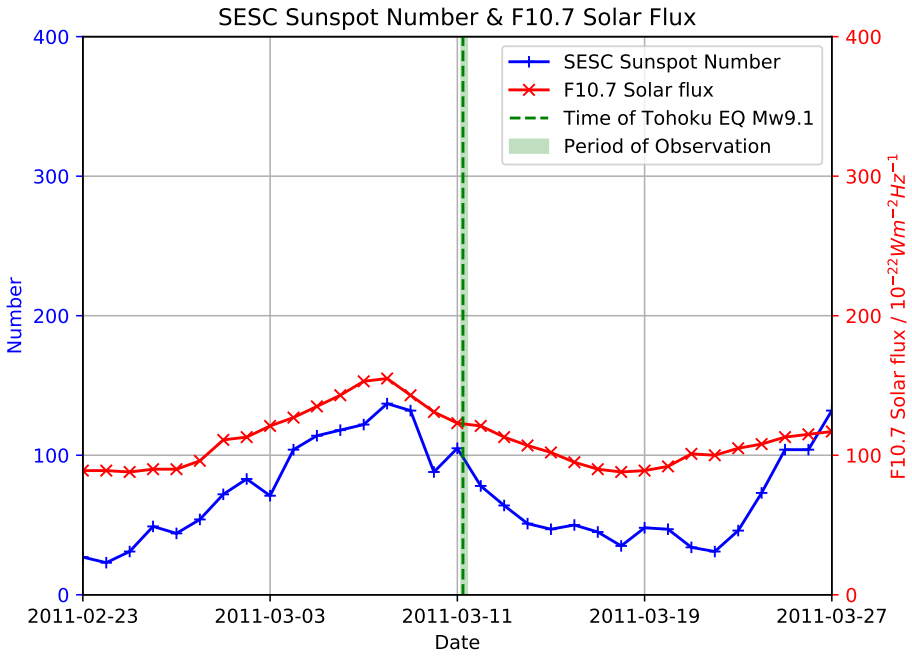

FIGURE 4.3: Observation of Solar Activity Indices, blue line for SESC Sunspot Number, red line for F10.7 Solar Flux index.

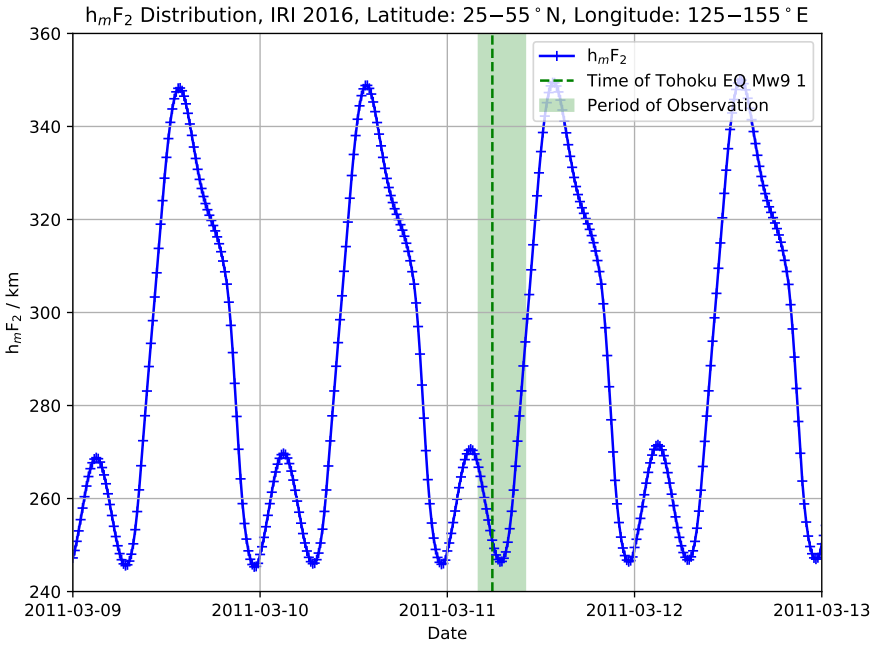

FIGURE 4.4: Climatic hmF2 at the region of 25–55°N & 125–155°E, based on the International Reference Ionosphere (IRI) 2016 model.

(2011d), or strong geomagnetic activities, from U.S. NOAA National Centers for Environmental Information (2011a).

The hourly hmF2 on this day varired from 246 km to 265 km, where the climatic hmF2 values are provided by the IRI 2016 model (see Bilitza et al., 2014), obtained from U.S. NASA Goddard Space Flight Center (2012). According to Hernández-Pajares, Juan, and Sanz (2006), the maximum MSTID generation occurs at the height below hmF2 because the MSTIDs are generated by the interaction between neutral and ion particles.

In order to better characterize the gravity waves, we assumed that the most frequent dominant MSTIDs are generated below hmF2, so we took 240 km as the mean effective height of the MSTIDs, which is lower than the average hmF2.

4.4 Methodology of GNSS Preprocessing and TIDs Characterization

In this section, we divide the TIDs detection process into two phases.

a) The first phase consists in the GNSS data preprocessing technique, i.e., obtaining the ionospheric combination from the GNSS carrier phase data, filtering the trend and bias, and mapping the detrended vertical TEC data, see detailed descriptions in Section 1.2. The technique of detrending employs the double difference to eliminate the trends in the ionospheric combinations. The selection of the double difference delays is justified by the publications listed next: Rolland et al. (2011) by means of the band pass filter with the passband of 1–1000 sec, observed the occurrences of two kinds of TIDs during the earthquake / tsunami, which could be originated from the acoustic resonance and atmospheric gravity waves. They also reported the periods of these two kinds of TIDs concentrate at 500–1000 sec and about 220–270 sec. Galvan et al. (2012) also observed the compatible TIDs behaviours with the bandpass of 200–2000 sec.

Taking into account the above mentioned publications, in this work we use both a 60 sec and a 300 sec interval of the double difference. The 300 sec interval allows a high sensibility to the tsunami-induced TIDs with the dominant periods in the range of 400–1200 sec. The 60 sec interval for the double difference is used to filter the trend and preserve the TIDs with the periods centered around the range 80 to 240 sec. The TIDs in the range 80 to 240 sec are mostly launched by the Rayleigh waves or acoustic resonance after the earthquake.

b) In the second phase, we detect and characterize the medium scale TIDs propagation parameters by means of the comprehensive multi-TID detection technique,

ADDTID, see details in Chapter 1. To obtain the local TIDs propagation characteristics and their geographical information, the GEONET GNSS network is divided into nine $10^\circ \times 10^\circ$ mesh subnetworks, and their propagation parameters are independently studied by the ADDTID algorithm, see the information of subnetworks marked by magenta color in Figure 4.1 (a–i), and the details of ADDTID implementation in Section 3.4.

4.5 Visual Summary of TID behaviour during Earthquake & Tsunami

In this section we will describe the behavior of disturbances during the earthquake by means of detrended VTEC maps and the keogram plots. This section is justified in order to validate the results obtained by the algorithm ADDTID in subsection 4.6, a) visually by the VTEC maps and b) by the partial information given by the keograms, and also confirm new results obtained by the algorithm ADDTID. These results are visually difficult to appreciate and could go unnoticed, whereas they can be appreciated clearly by following the indications given by the algorithm proposed in this thesis.

4.5.1 Detection of Ionospheric Perturbation by GNSS Sounding

In section 4.3, we justified the selection of 240 km as the height of the single ionospheric layer during the period of GNSS observation for the earthquake / tsunami event, see Figure 4.4. We show the locations of IPPs at the assumed height in Figure 4.5, from the moment from the time of earthquake to 30 min later. Each color represents the IPPs set of individual GPS satellite. The locations of the epicenter in red star and the IPPs in brown points clearly show that IPPs of GPS satellite PRN 26 record the ionospheric variation information around the epicenter. For this satellite, the observational data of GNSS receivers whose IPP locations are less than 250 km from the epicenter (marked by the black circle in Figure 4.5) are selected to describe the relationship between the ionospheric perturbation and the earthquake / tsunami. As an additional limitation, the receiver observations are also filtered out if meet the losses of lock on GPS. Figure 4.6 depicts the slant TECs from these receivers by means of LIs which are arbitrarily aligned to clarify the ionospheric variations. This group of STECs from aligned LIs shows there is a large TEC depletion up to 9 TECUs appeared about 10 minutes after the earthquake, and drastic ionospheric oscillations after the depletion. Chen et al. (2011), Saito et al. (2011), and Tsugawa et al. (2011) also reported the compatible observation of the sudden decrease of TEC as the response of ionosphere to the earthquake / tsunami.

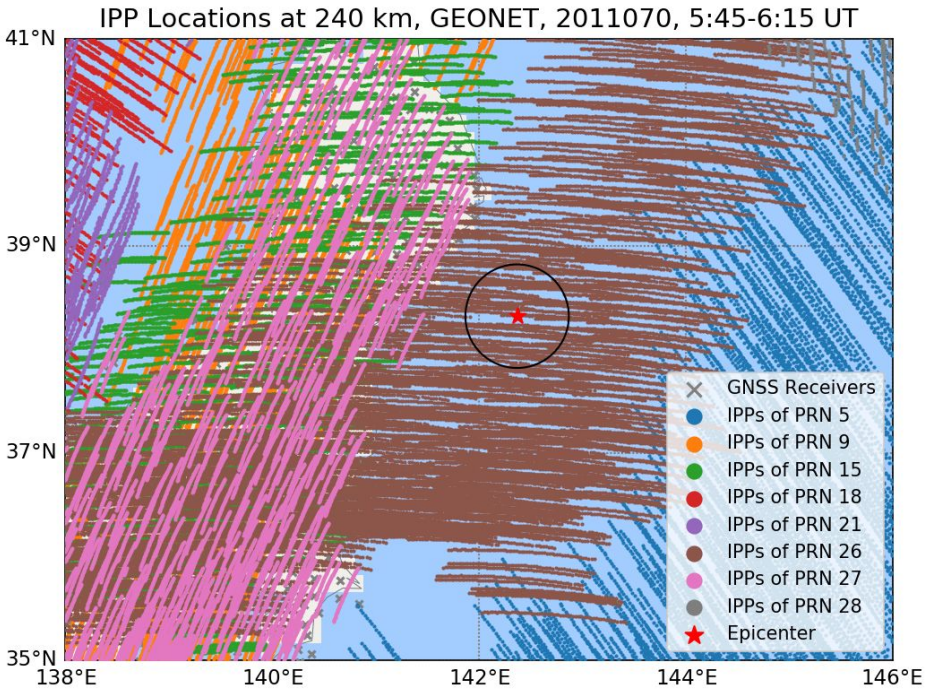

FIGURE 4.5: IPP locations at height of 240 km, corresponding to the GEONET GNSS receivers, from 5:45 to 6:15 UT. The color codes of cycles for the IPP locations of different satellites, the grey cross for the location of GNSS receivers, the red star for the location of epicenter.

In the next two subsections, we present the summary with detrended VTEC maps and Keogram plots.

4.5.2 TID Propagation Description from Detrended VTEC Maps

To facilitate the tracking of the time and space evolution of the induced ionospheric perturbations, we have summarized the TID maps in two movies with time resolution of 30 sec. These two movies can be accessed in the internet at Yang (2019a,b).

Next we summarize the time evolution of the perturbations from these two movies by means of a selection of 6 snapshots taken at selected moments. The case of the double-difference detrending at 300-sec intervals is shown at Figure 4.7, which depicts six moments of ionospheric fluctuations during the period of earthquake / tsunami from 5:50 to 9:00 UT. The behaviour can be summarized as follows: in the early moment after the earthquake Figure 4.7(a) shows a group of strong ionospheric disturbances suddenly appearing with a time delay of 8–10 min. The following snapshot is taken 10 minutes after the first. Figure 4.7(b) shows that the ionosphere

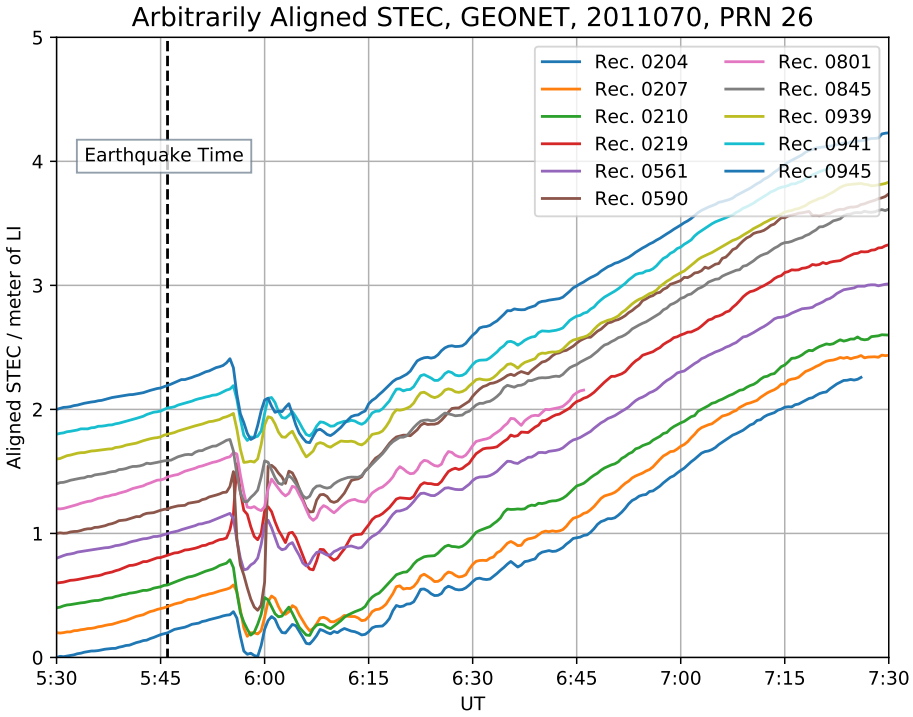

FIGURE 4.6: Time evolution of the arbitrarily aligned slant TECs, for the GPS satellites PRN 26, at the time of 5:30–7:30 UT. The color codes of lines correspond to different GNSS receivers, the black dash line indicates the time of the earthquake at 5:46 UT.

exhibits significant disturbances which can be approximated as a circular wave that propagates with large horizontal wavelengths up to 600 km. At 06:30 UT, as shown in the next subfigure, the disturbances behave more like the circular travelling disturbances that propagate from the epicenter to the outside. The wavelengths show two different scales respectively located in the inner and outer circles in Figure 4.7(c). After that, the propagation of the smaller scale disturbances follows a very clearly circular wave pattern until about 09:00 UT. Then, it fades away slowly, see Figure 4.7 (d–f).

For the 60 sec double difference detrending case, Figure 4.8 shows the same six moments of the detrended VTEC movie in order to highlight the presence of another group of TIDs. Compared to the disturbances in Figure 4.7, one can discern at least two kinds of ionospheric disturbances. The TIDs associated with this case show a shorter wavelength, in particular, as seen in Figure 4.8 (b–c), with higher velocity, lower intensity and shorter duration than the 300 sec detrending case.

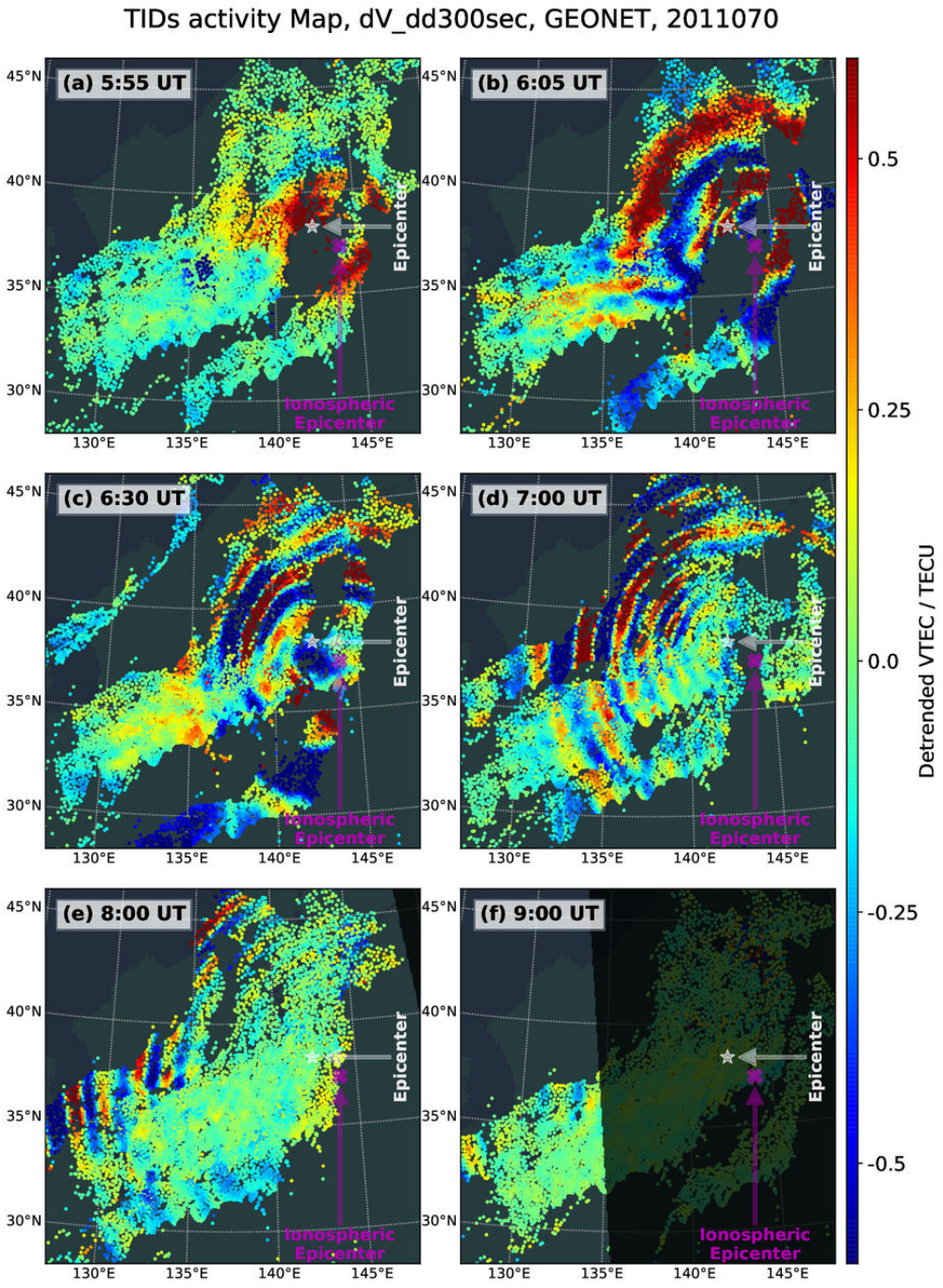

FIGURE 4.7: Evolution of TIDs activity maps, detrended by double difference of time interval of 300 sec, from GEONET network, on the day 70 of 2011, for all the GPS satellites. The maps (**a**–**f**) are at epochs of 05:55, 06:05, 06:30, 07:00, 08:00 and 09:00 UT, respectively.

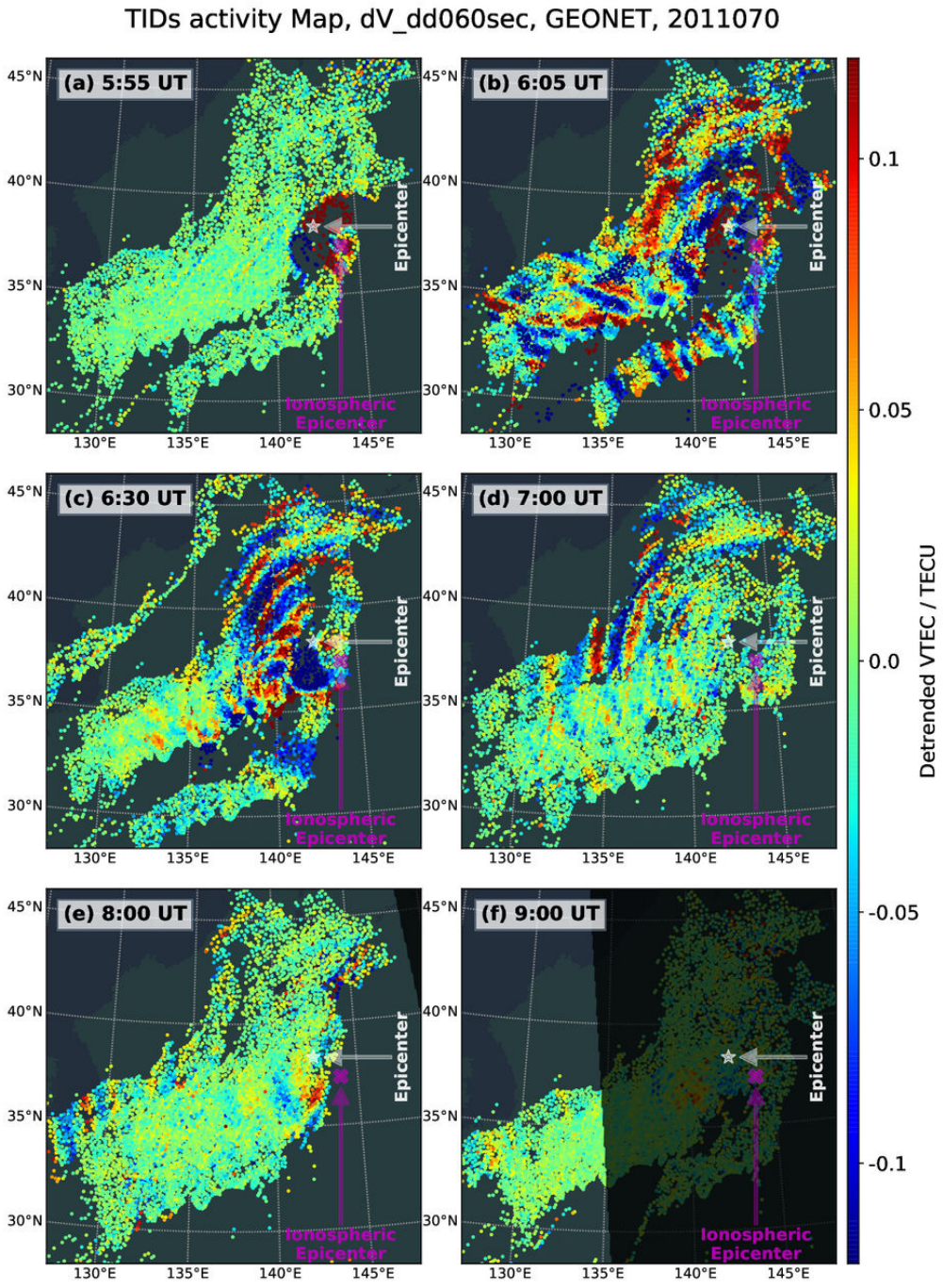

FIGURE 4.8: Evolution of TIDs activity maps, detrended by double difference of time interval of 60 sec. The plot is organized as in Figure 4.7.

Note that the circular TIDs propagate as concentric waves with centers that do not totally coincide with the epicenter, see the magenta cross symbol in the maps of Figure 4.7.

At the assumed height of 240 km, observe that the center of the circular TIDs is located about 200–300 km southeast of the epicenter. Tsugawa et al. (2011) also observe the non-overlapping by assuming the TIDs height of 300 km, and label the center as the ionospheric epicenter. One fact is that the atmospheric waves could be generated by the vertical displacement of the sea surface, and the center of the triggered circular TIDs, i.e. the ionospheric epicenter, should show the agreement regarding to the epicenter. One possible explanation could be a projection error in assuming that the TIDs propagate at 240 km height, however the expense is extremely expensive to compute optimal value for the global effective height of TIDs. In this work we emphasize the study of the TIDs and their propagation properties from the ionospheric center by discarding the inconsistency regarding to the actual epicenter. Also note some IPPs show incompatible locations of the wavefronts of the concentric waves. For example, the wavefronts appear in the southwest corner of the epicenter in spite of different phases, which come from different GPS satellite observation sets, see Figure 4.7(e). This might indicate that the phase of the upward TIDs waves at different heights are measured simultaneously by these GPS satellites, which could be understood as an incomplete tomography scan, while the single layer model of the ionosphere is not enough to analyze the TIDs propagation in this case. Nevertheless, this work only takes into account the horizontal propagation of the TIDs by neglecting the vertical characteristics, and the IPP set of each satellite that avoids the overlapping problem is used to detect the TID parameters by means of ADDTID technique.

4.5.3 TID Characterization and Description from Keogram Plots

The TIDs map in Figure 4.7 and 4.8 show circular wave pattern as the ionospheric response to the earthquake / tsunami. In order to describe the propagation features, the detrended VTECs of the IPPs are organized by their geographical distances from the epicenter at the same epoch, and plotted as time evolution of distances, see the two keogram plots in Figure 4.9. Note the IPPs sets of all the GPS satellites are used to create the keogram plots. Almost all of them show a behavior compatible with the phases of circular waves. The keogram plots for detrended VTECs at 60 sec (upper figure) and 300 sec (lower figure) in Figure 4.9, highlight the presence of circular ionospheric disturbances with different propagation velocities at different stages of the earthquake / tsunami.

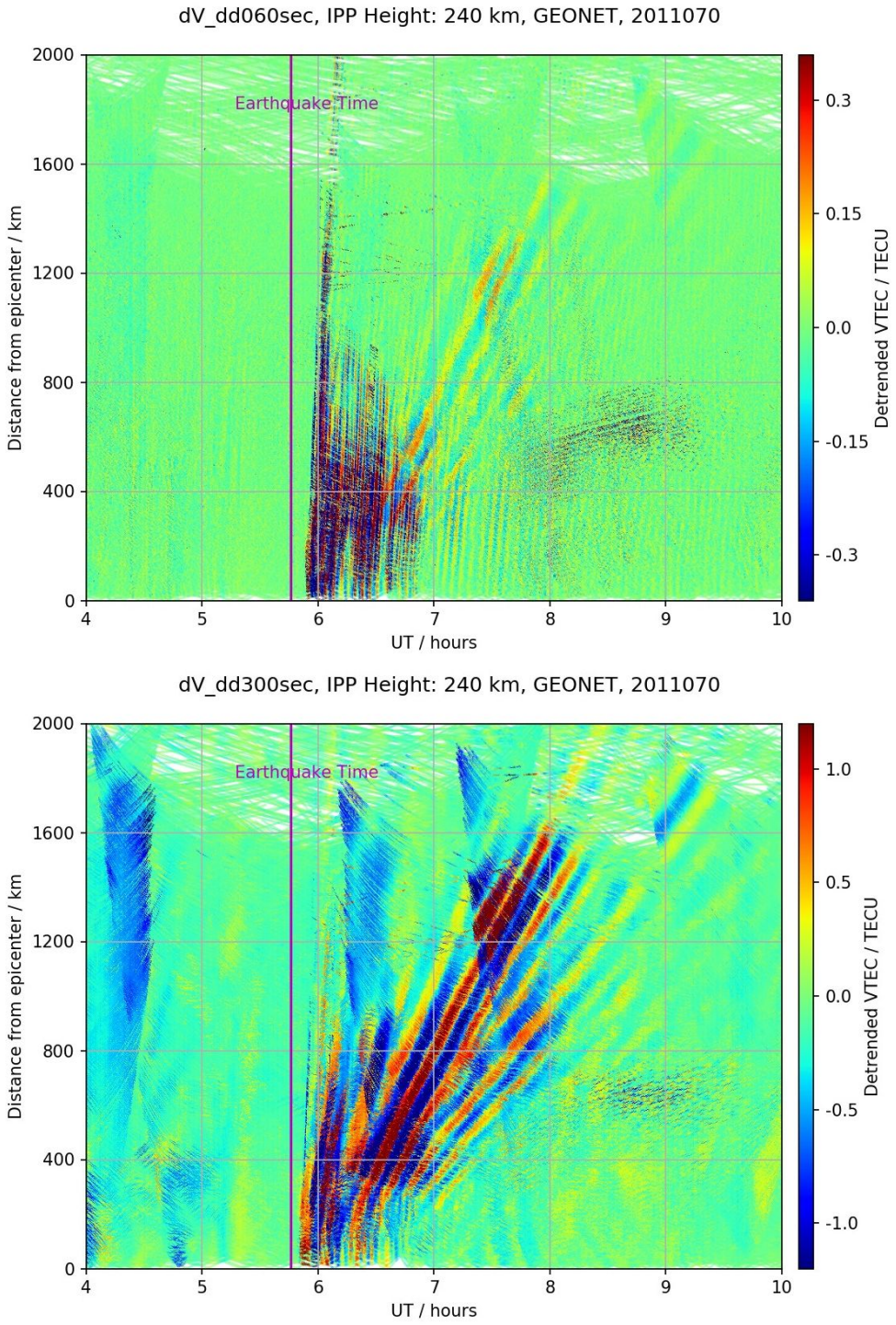

FIGURE 4.9: Evolutions of TID disturbances for 6 hours during the earthquake / tsunami, detrended by double difference of time interval of 60 and 300 sec for upper and lower figures, respectively. The two keogram plots are organized by the geographical distance from the epicenter and the period time from 04:00 to 10:00 UT, from GEONET network, for all the GPS satellites, on the day 70 of 2011.

About 10 min after the earthquake, a set of circular disturbances with over 500 km wavelength appear, and initially display very high velocities of about 3000 m/s. In particular, this can be seen in the figure of the detrended VTEC keogram corresponding to the 60-sec intervals as shown in Figure 4.9 (upper plot). These TIDs appearing with the amplitude up to 0.5 TECU is concentrated in the time period of 6:00–7:00 UT and fade away in the next two hours. During this period several aftershocks of the earthquake occur at lower magnitude, specially during the first hours after the mainshock. Note the propagation radius of the high-speed TID close to the mainshock is more than 2000 km, while the others become shorter over time. This might indicate that the mainshock and the aftershocks could trigger fast TIDs, the intensity of which is positively correlated with the magnitudes of the earthquakes. The another set of TIDs, with the velocity decreasing from about 3000 down to 750 m/s, displays larger wavelengths, see the keogram with 300-sec detrending in lower Figure 4.9.

The third set of TIDs also shows much lower velocities decreasing from 400 to 150 m/s after a short period of time. The circular disturbances can be appreciated clearly in both keograms of Figure 4.7, where the one with 300-sec detrending shows higher amplitude. This has also been reported by other authors, for instance in Galvan et al. (2012), Liu et al. (2011a), Rolland et al. (2011), and Tsugawa et al. (2011). In particular Galvan et al. (2012) and Tsugawa et al. (2011) pointed out the circular TIDs with the velocity of 1000–3000 m/s that is consistent in velocity with the Rayleigh wave as one type of surface wave produced during earthquakes. The ones with the velocity of about 750–1000 m/s should be originated by the an acoustic wave generated from the sea surface, and the medium scale circular TIDs with lower velocities of 400–150 m/s may be induced by the gravity atmospheric waves from the tsunami.

4.6 ADDTID for TIDs Detection and Characterization

In this section we use the ADDTID algorithm to automatically detect and characterize the earthquake-related TIDs. For a detailed introduction see Chapter 1, and the applications in two case studies in Chapter 2 and 3. In the following section, we present the time evolution of the parameters of detected TIDs in the area surrounding the epicenter during the time period of 04:00–09:00 UT.

As described in section 4.5, during the early stage of the earthquake and tsunami, we were able to determine by visual inspection the predominant TIDs that consisted of circular waves with up to 600 km horizontal wavelength. These TIDs exhibited velocities over 1000 m/s, while another group of circular waves of smaller wavelength subsequently showed higher intensities. The fast ionospheric disturbances

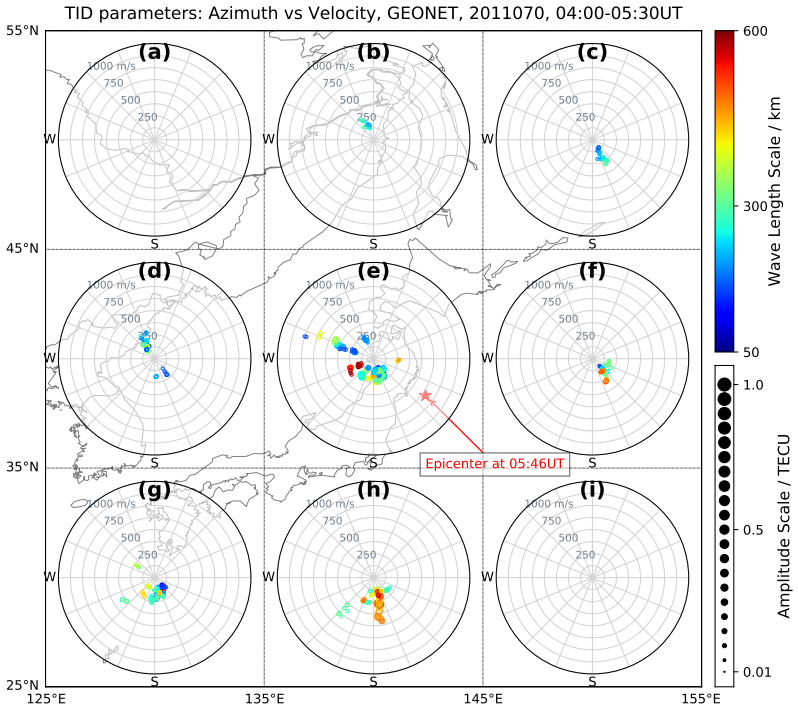

FIGURE 4.10: MSTID parameters in **04:00–05:30** UT, from VTEC maps detrended by double difference of **300** sec, presented by polar plots of azimuth (deg) vs velocity (m/s). TIDs wavelength range is color coded, and the size of the circles denotes their amplitude in TECU.

probably are launched by the Rayleigh wave or acoustic waves and the dominant ones from the acoustic waves or tsunami, as indicated by Galvan et al. (2012) and Tsugawa et al. (2011).

To emphasize the relationships between the earthquake / tsunami and the triggered TIDs, this work analizes the TIDs by means of detrended VTEC maps with double difference intervals of 60 and 300 sec. As justified in subsection 4.5.2, the TIDs were assumed to be at a height of 240 km. The estimation of the disturbances by means of the ADDTID was done in nine geographical grids of $10° \times 10°$. This grid was a partition of the GEONET network (25°N–55°N, 125°E–155°E). The partition of the region is shown in Figure 4.1. The nine corresponding plots that show the parameters of the TIDs, along with their relative locations (note the underlying maps), are depicted Figures 4.10–4.25. These figures show the TID propagation velocities and azimuths represented by the the hallow circles on the nine polar plots, where the wavelengths are coded by the circle color from 50 to 600 km, and the amplitudes by the circle size from 0.01 to 1.0 TECU (note the scales at the right of the figures).

Below we present the temporal analysis of the geographical distribution of TIDs. The analysis has been divided into 8 time intervals, characterized by different behaviors.

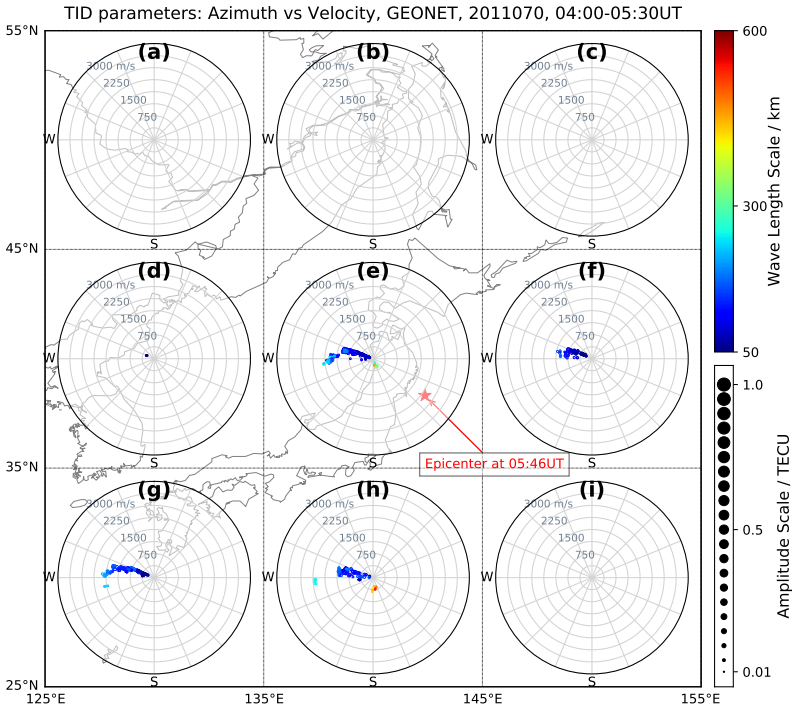

FIGURE 4.11: MSTID parameters in **04:00–05:30** UT, from VTEC maps detrended by double difference of **60** sec, presented by polar plots of azimuth (deg) vs velocity (m/s). TIDs wavelength range is color coded, and the size of the circles denotes their amplitude in TECU.

Before the earthquake during 04:00–05:30 UT (13:30–15:00 LT), the TIDs appear with weak amplitude lower than 0.1 TECU as shown in Figure 4.10, where most TIDs propagate towards the equator, along with several with westward motions. These TIDs show the disperse wavelength and period distributions of 100–500 km and 10–60 min respectively, everything in agreement with the expected climatology of Medium Scale TIDs for winter season and daylight time (see Hernández-Pajares et al., 2012b). Nevertheless, these TIDs cannot be directly observed from the fluctuation of LIs (see Figure 4.6) nor the keogram plot (see Figure 4.9) due to the wide scale of the observation, and the fact that they are planar waves. The TIDs in the local afternoon show an activity very similar to the one observed during the 80th day of 2011 (10 days later), with two different classes: predominant equatorward movements at winter daytime, and a few westward propagations for the period related to the solar terminator. Those can be double checked by the visual inspection from Yang (2019a), also see the similar observations in section 2.5.2. In addition, at the same period, a set of westward TIDs moves with velocities ranging from 300–1000 m/s in the all observable subnetworks of Figure 4.11. Their wavelengths go from 50 to 120 km, and the amplitude is less than 0.1 TECU. These TIDs also can be double checked from Yang (2019b).

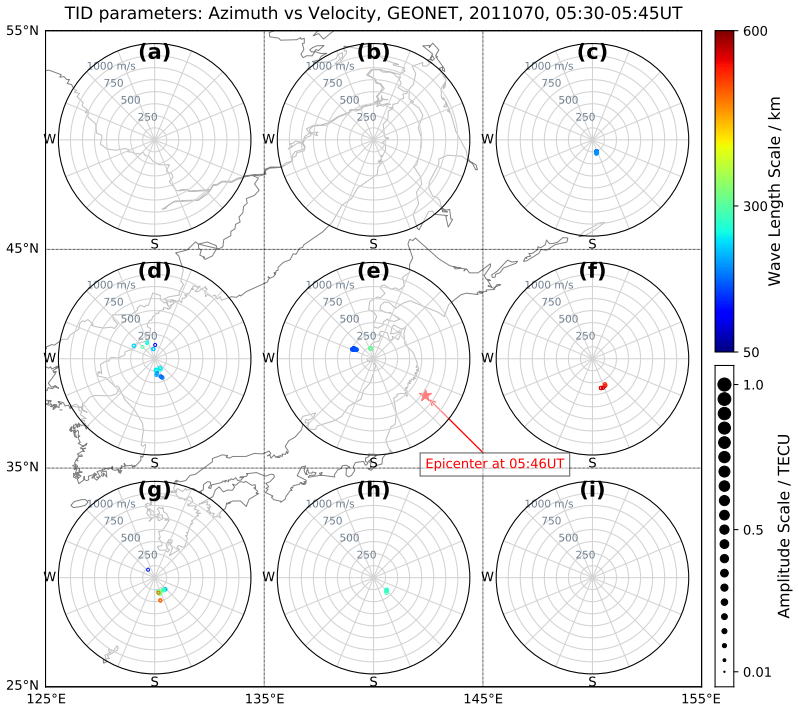

FIGURE 4.12: MSTID parameters in **05:30–05:45** UT, from VTEC maps detrended by double difference of **300** sec, organized as Figure 4.10.

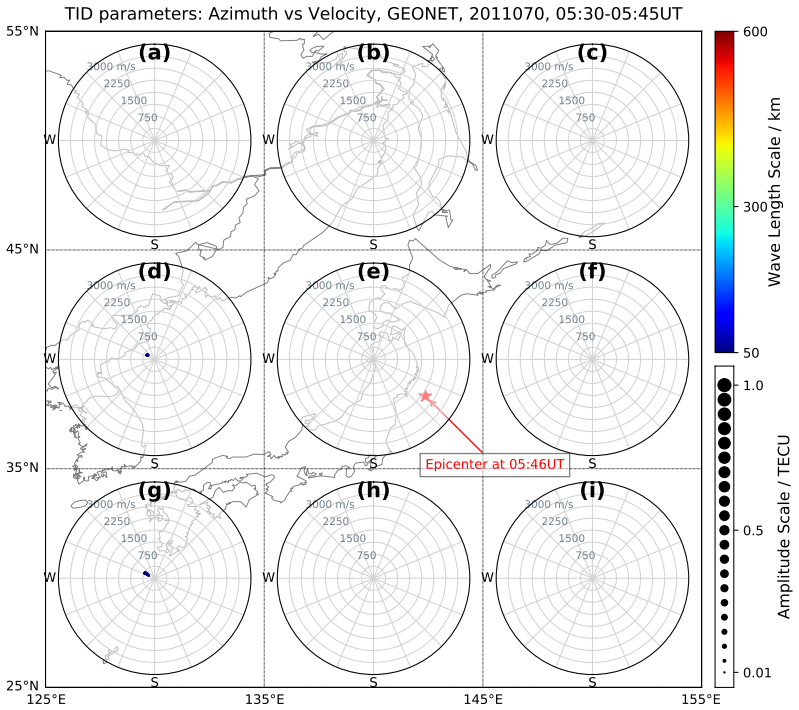

FIGURE 4.13: MSTID parameters in **05:30–05:45** UT, from VTEC maps detrended by double difference of **60** sec, organized as Figure 4.11.

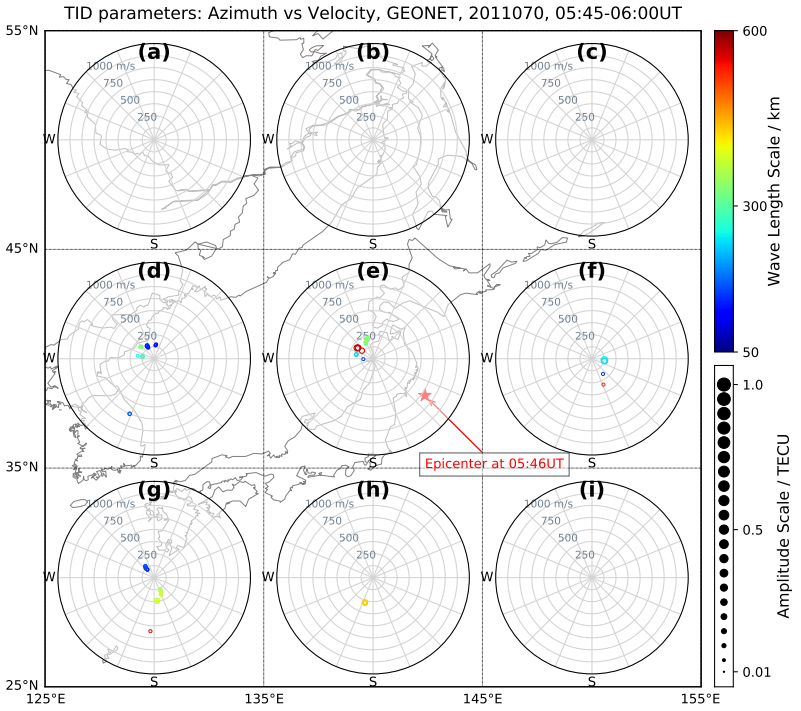

FIGURE 4.14: MSTID parameters in **05:45–06:00** UT, from VTEC maps detrended by double difference of **300** sec, organized as Figure 4.10.

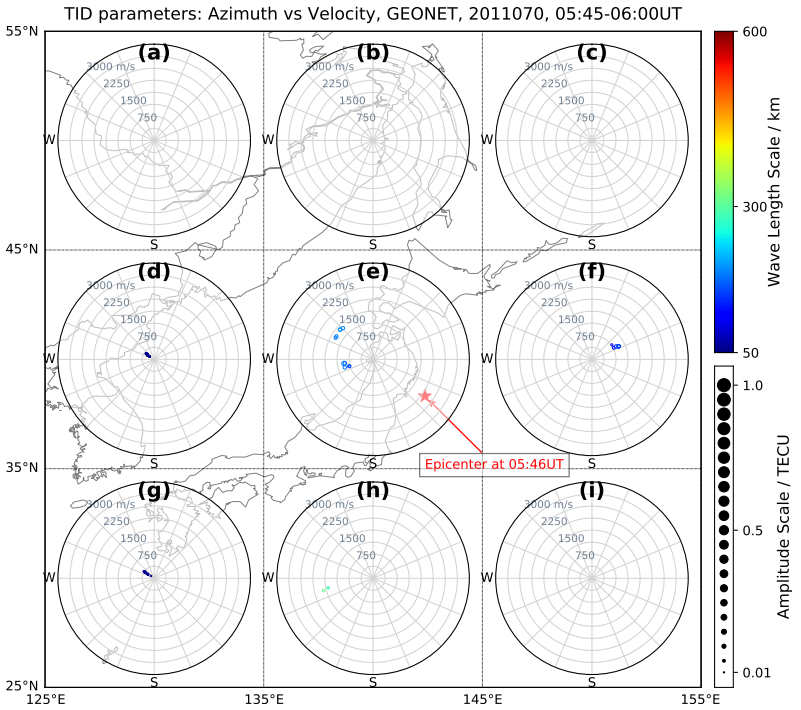

FIGURE 4.15: MSTID parameters in **05:45–06:00** UT, from VTEC maps detrended by double difference of **60** sec, organized as Figure 4.11.

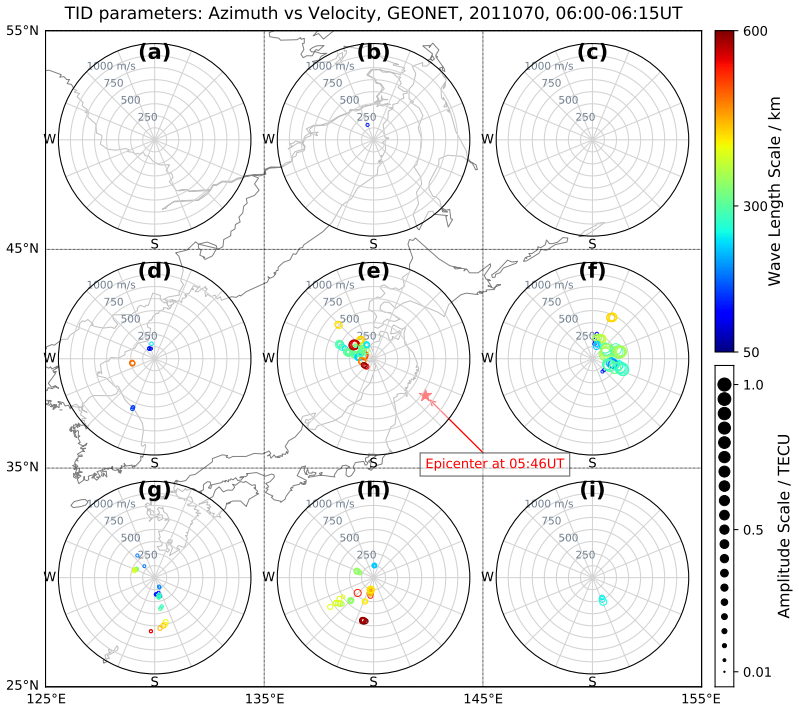

FIGURE 4.16: MSTID parameters in **06:00–06:15** UT, from VTEC maps detrended by double difference of **300** sec, organized as Figure 4.10.

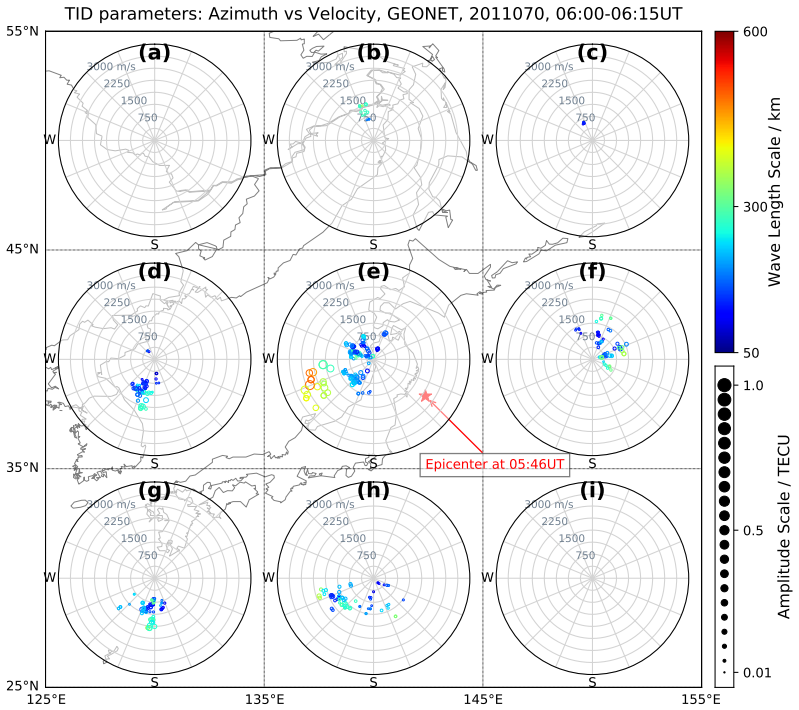

FIGURE 4.17: MSTID parameters in **06:00–06:15** UT, from VTEC maps detrended by double difference of **60** sec, organized as Figure 4.11.

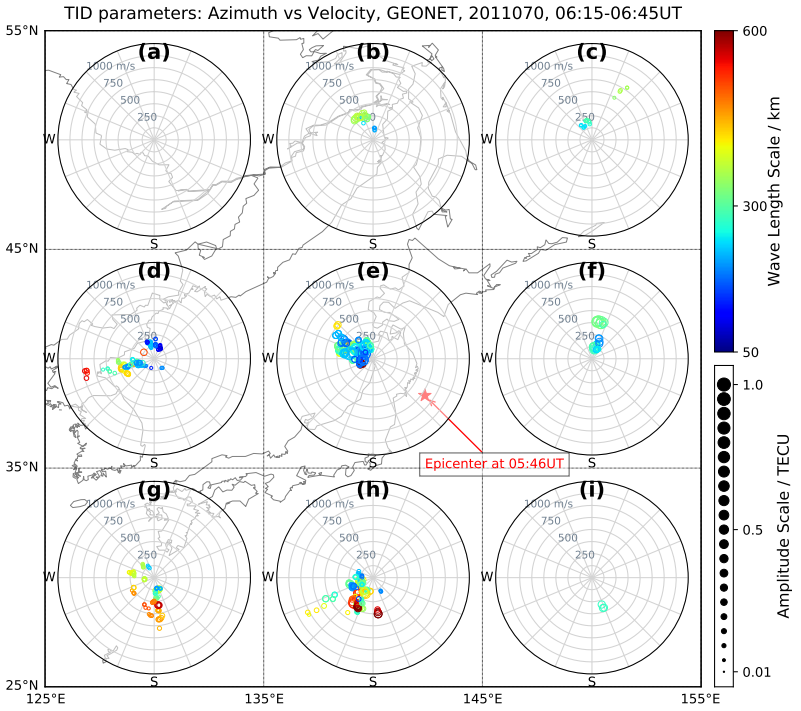

FIGURE 4.18: MSTID parameters in **06:15–06:45** UT, from VTEC maps detrended by double difference of **300** sec, organized as Figure 4.10.

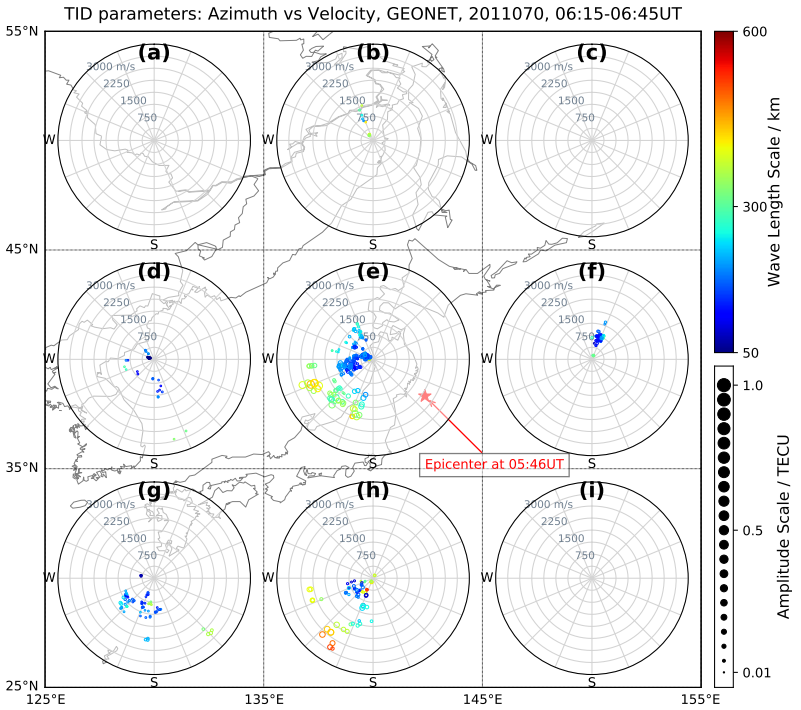

FIGURE 4.19: MSTID parameters in **06:15–06:45** UT, from VTEC maps detrended by double difference of **60** sec, organized as Figure 4.11.

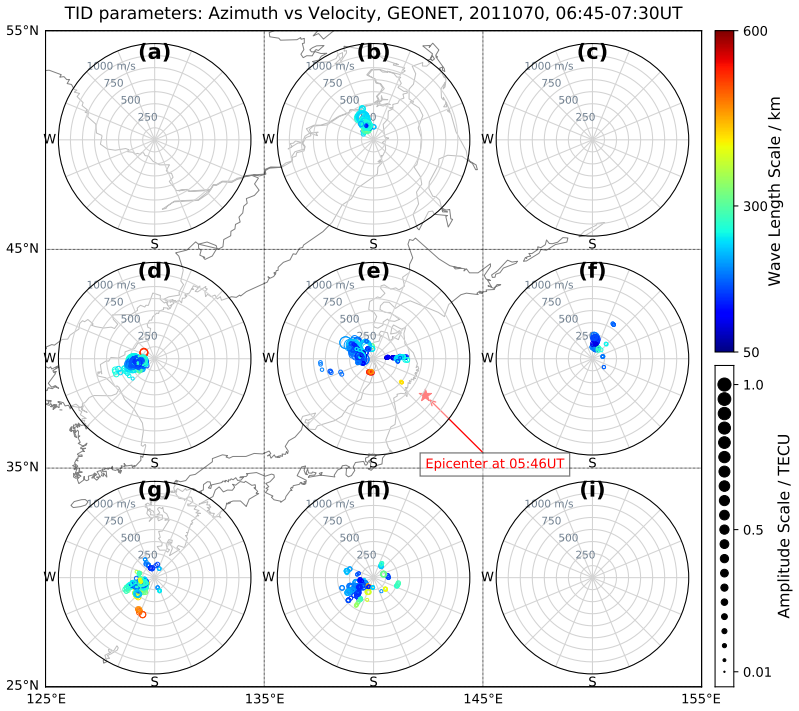

FIGURE 4.20: MSTID parameters in **06:45–07:30** UT, from VTEC maps detrended by double difference of **300** sec, organized as Figure 4.10.

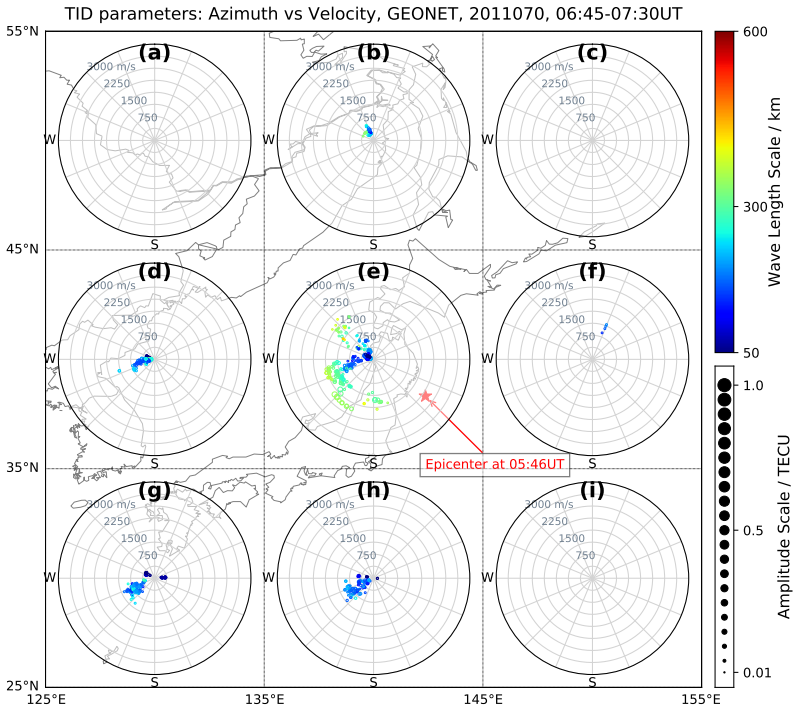

FIGURE 4.21: MSTID parameters in **06:45–07:30** UT, from VTEC maps detrended by double difference of **60** sec, organized as Figure 4.11.

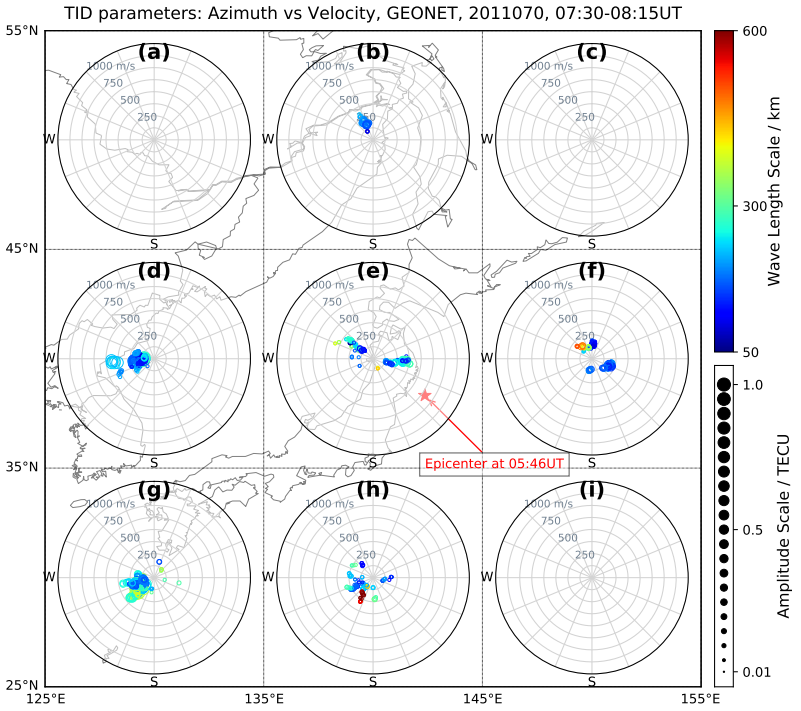

FIGURE 4.22: MSTID parameters in **07:30–08:15** UT, from VTEC maps detrended by double difference of **300** sec, organized as Figure 4.10.

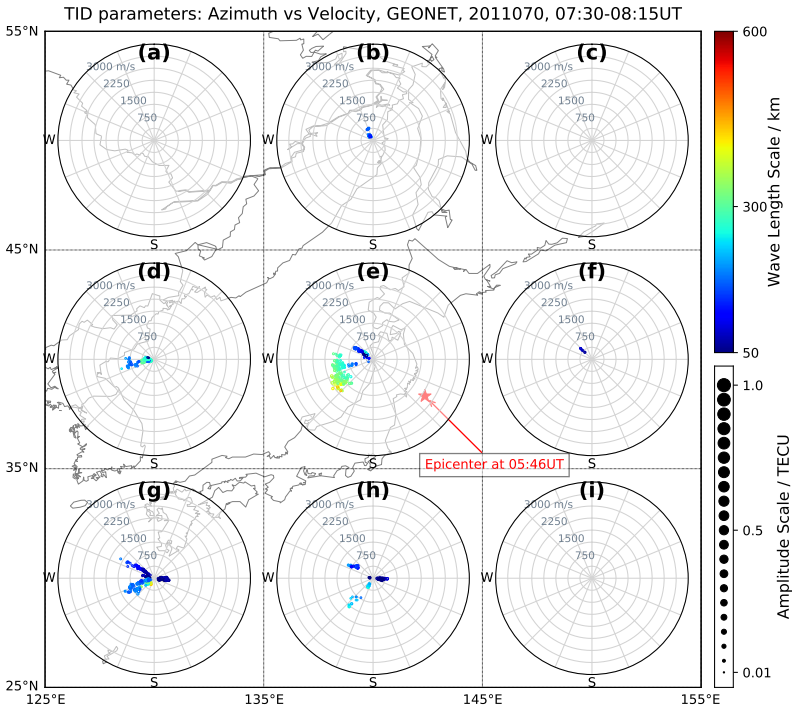

FIGURE 4.23: MSTID parameters in **07:30–08:15** UT, from VTEC maps detrended by double difference of **60** sec, organized as Figure 4.11.

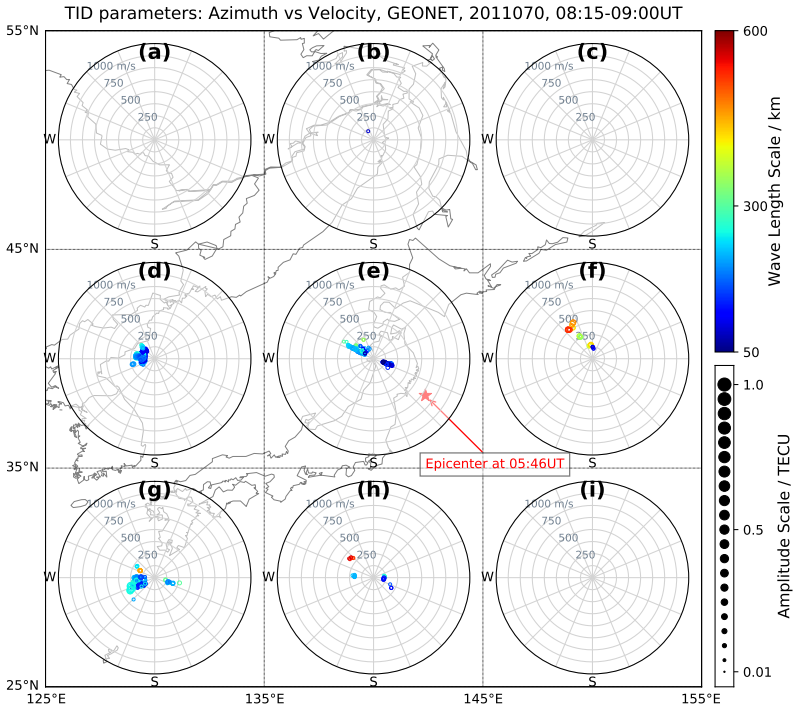

FIGURE 4.24: MSTID parameters in **08:15–09:00** UT, from VTEC maps detrended by double difference of **300** sec, organized as Figure 4.10.

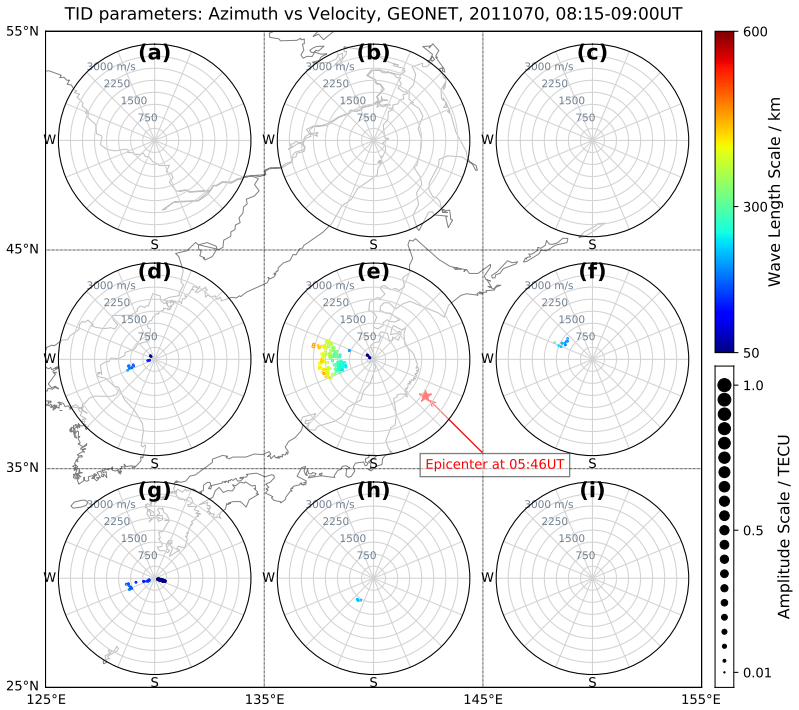

FIGURE 4.25: MSTID parameters in **08:15–09:00** UT, from VTEC maps detrended by double difference of **60** sec, organized as Figure 4.11.

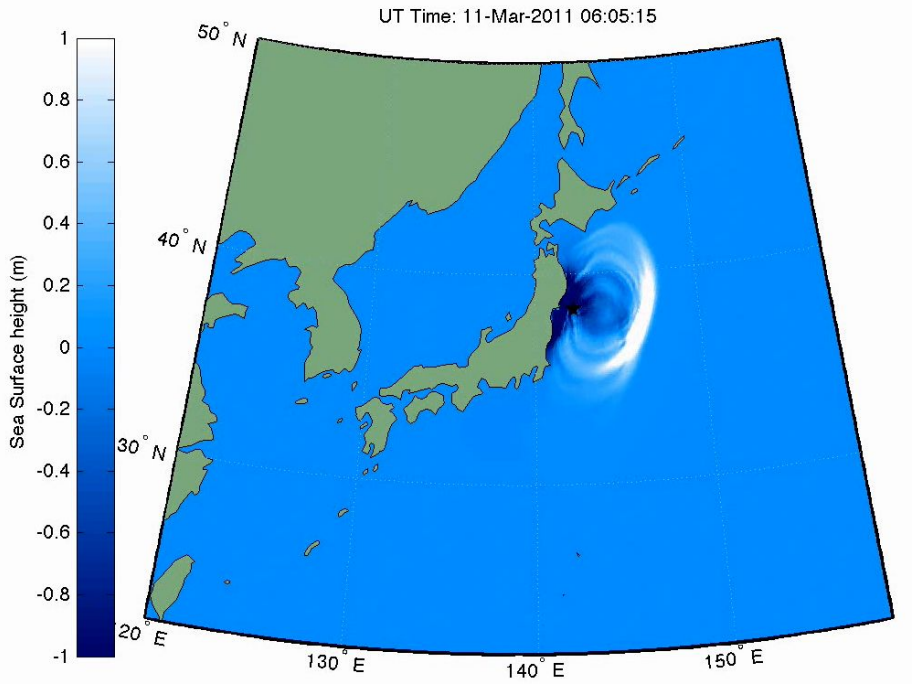

FIGURE 4.26: Tsunami simulation by Song model of sea surface wave heights at 06:05 UT, reproduced from Galvan et al. (2012).

Within 15 minutes before the earthquakes, both Figures 4.12 and 4.13 show only the regular TIDs as before, which is compatible with the observations of LIs in Figure 4.6 and the keogram plots of detrended VTEC in Figure 4.9.

At the time of 05:46 UT, the magnitude 9.1 Mw undersea earthquake occurred 70 km east of the pacific coast of Japan Tohoku, and the great tsunami (with the height up to 40.5 meters) was triggered sequentially (see Mori, Takahashi, and Group, 2012). Although the large scale TEC depletion appears around the epicenter from 05:55–06:00 UT (see Figure 4.6), no irregular TID is detected from detrended VTEC maps @ 300 sec in Figure 4.14. However, Figure 4.15 shows that several TIDs with wavelengths of about 150–200 km, appear in the two subnetworks (e, f), which are located on the west side and east side of the epicenter, respectively.

Note that the estimated velocity is in the range of 500–1400 m/s, which is not compatible with the visual inspection, see subsection 4.5. This is justified because: a) for the sake of that ADDTID can not correctly recover the TID velocity if the distance of TID propagation during the sampling period (i.e. time resolution, for instance 30 sec in this work) was over the half wavelength. b) In the one hand, the set of circular TIDs with extremely high velocity of about 3000 m/s are considered to be the disturbances from the Rayleigh waves originated from the earthquake, but the current implementation of the algorithm is not well prepared for this case because it assumes plane wave propagation, and, at the beginning of the tsunami, at the scale

of the first minutes, the front waves cannot be locally approximated as plane waves. In despite the present version of the ADDTID algorithm could not deal well with the TEC depletion because of the design of the searching dictionary, a natural solution for the early detection of concentric waves related to a tsunami is to introduce a few elements in the dictionary that characterize the initial circular waves, following a morphology as seen in Figure 4.7(a). This improvement will be introduced in the near future, and would be able to allow for an alarm with a delay of 15 minutes.

Since 06:00 UT, a couple of MSTIDs suddenly appear in the subnetworks close to the epicenter in Figure 4.16, particularly in subplots (e), (f) and (h), propagating with almost omnidirectional azimuths as the circular characteristics, compatible to the concentric waves on the detrended VTEC maps in Figure 4.7. Note that the geographical partition of the area around the epicenter allows us at this scale to approximate a circular wave by local planar waves. The estimation of the parameters of most MSTIDs yields wavelengths in the range of 300–400 km, amplitudes in the range of 0.4–1.0 TECU, periods in the range of 1200–1800 sec, and velocities in the range of 100–300 m/s. Note that these MSTIDs could not be directly seen from the keogram plot (see lower part of Figure 4.9), whereas the visible waves with extremely fast velocity have not been detected. This is because the most part energy of fast waves (within periods of about 80–240 sec) have been filtered out in the detrended VTEC maps @ 300 sec, and only the slower MSTIDs have been studied by means of ADDTID. From the propagation parameters of the MSTIDs driven by the atmospheric wave, one can relate these TIDs to the tsunami that is located near the epicenter at this moment. Also note that the set of MSTIDs in subplot 4.16(f) that travels toward east exhibit the most significant amplitudes up to 1 TECU. Taking into account that these MSTIDs might be observed at IPP locations away from the receiver with a low elevation angle, in this work, the elevation mask of above 15 degrees has been used to filter out the distortion of the MSTIDs. These MSTIDs could be originated by the tsunami, and could have different heights of wavefronts in different directions of propagation. One justification is the tsunami simulation from Song's model (see Song et al., 2012), shows the similar sea surface wave height distribution of tsunami at 06:05 UT, i.e. the height at the eastern part is much higher than the other part, see Figure 4.26, reproduced from Galvan et al. (2012). Furthermore, some MSTIDs with larger wavelengths of 500–600 km and the faster velocities of about 400–700 m/s, also show the almost omnidirectional azimuth propagations, by taking into account very few of valid GNSS observational data east of the epicenter (see Figure 4.16). These could be the ones originated from the acoustics waves of the sea surface, which show the consistent features with the keogram plots.

We will use the detrended VTEC maps @ 60 sec to detect and characterize the TIDs by ADDTID, in order to deal with the ionospheric disturbances induced by acoustic

waves of earthquake. Figure 4.17, in particular the subnetwork (e), clearly shows two kinds of TIDs surrounding the epicenter, i.e. the large wavelength TIDs, as the predominant waves show the highest velocities of about 1500–2300 m/s, whereas the weaker ones with smaller wavelength propagate at the velocities of about 500–1500 m/s. These TID propagation parameters are consistent with the visual inspection in section 4.5, which are regarding to the Rayleigh and acoustic waves of earthquakes.

From 06:15 to 06:45 UT, the circular MSTIDs have reached the subnetworks which are far away from the epicenter, as shown in the subplots of Figure 4.18 (b), (c), (d) and (g). There are two types of MSTIDs with different scale wavelengths in the subplots: the large wavelength disturbances with the velocity of 400–700 m/s, while the small ones with lower velocities. Similarly, they could be also respectively originated from the acoustics waves of the sea surface and the atmospheric waves of the tsunami, which seems to be consistent features with the keogram plots. Note that the MSTIDs still occur in the subnetworks near the epicenter, which corresponds to the continuous outward spreading of the concentric circular MSTIDs. In spite of the very rough geographical information presented by the division into nine subnetworks, yet the MSTIDs can indicate the approximate location of their center which is adjacent or in the subnetworks (e), (f), (h) and (i). Meanwhile, the fast circular TIDs in Figure 4.19 still show two scales of waves, the propagation characteristics of which are similar to those shown in Figure 4.17.

In the observation time of 06:45–08:15 UT, the circular MSTIDs with wavelengths of 200-300 km appearing in all subnetworks spread from the center to farther locations, see Figure 4.20 and 4.22. With similar intensities and wavelengths distribution of these two moments, MSTIDs show lower velocities concentrated in the range of 125–300 m/s, which shows a consistent propagation pattern with the measurements from keogram plots. Note that the intensity of MSTIDs is much lower than before, which indicates that the origin, the tsunami continuously generated in the epicenter, is spreading less and less in the GNSS observing region.

At that moment, the TIDs related to the Raleigh waves disappear in Figure 4.21 and 4.23 and the ones launched by acoustic waves occur with lower frequency. Some of the detected TIDs show a circular pattern which might be associated to the tsunami.

In the observation time of 08:15–09:00 UT, most of the MSTIDs disappear and only a few ones located subnetworks far from the center can be detected with similar propagation parameters, see Figure 4.24. Likewise, in Figure 4.25, the TIDs related to the tsunami almost gone, and the ones related to the acoustic waves move westward propagations similar to the moment before the earthquake, distinguishing themselves by having a higher intensity. This shows that the tsunami is fading away

from this moment on, which is compatible with the detrended VTEC maps and the keogram plots, see Figures 4.8, 4.7 and 4.9. In another phase, the TIDs with large wavelength in the range 400–600 km and high velocity over 1000 m/s, occur at 6:00–7:00 UT and subsequently spread out of the observable area, and no more have been detected from the subnetworks, see Figure 4.20–4.25. It might indicate that the Rayleigh waves induced by the earthquakes reach the ionosphere a few minutes after the earthquake. Then they trigger the circular TIDs with similar propagation parameters, in particular the compatible intensities regarding the mainshock and some subsequent smaller aftershocks. Finally, these waves disappear and do not reappear during the tsunami propagation.

4.7 Summary

In this chapter we have described the propagation characteristics of circular TIDs generated by the Japan Tohoku earthquake / tsunami on the 70th day of 2011, after presenting the detected TIDs. In particular the MSTIDs estimated by means of the ADDTID algorithm, were verified by visual inspection from the ionospheric combination series, the detrended VTEC maps and the keogram plots for the whole time evolution of the tsunami. Furthermore, we have detected the different wavefront intensities between the east and west MSTIDs around the epicenter, which are consistent with the height distribution of the tsunami propagation modelling by Galvan et al. (2012). Finally, note that the detection is automatic, without human intervention, with a short delay, due to the initial transient of the perturbation.

Conclusion

Discussions and Conclusions

The core of the thesis has been the development of the Atomic Decomposition Detector of TIDs (ADDTID), which is an automatic method for determining the presence of an unknown number of disturbances over the ionosphere. This method allows to characterize without human intervention the state of the disturbances over the ionosphere, and detect new phenomena. It should be emphasized that for low level activity of the TIDs, unless one expressly seeks a specific phenomenon, it may go unnoticed. In this document, for each of the phenomena found with the algorithm we have presented the accompanying maps, one can see the movies where the phenomena is observed.

Also, we would like to emphasize that several of the phenomena that we present in the document have been discovered a posteriori, that is, after observing an anomaly in the results of the ADDTID, we have looked into the detrended VTEC maps, and found visually, patterns compatible with the results of the algorithm. This allowed us, for instance, to determine the disturbances generated by a low energy earthquake in Japan, the early arriving soliton waves before the eclipse reaches the continent or the detection of MSTIDs with velocities much higher than $400-600$ m/s during nighttime and the solar terminator.

As the specific conclusions related to each chapter:

In chapter 1, we have presented the mathematical derivation of the Atomic Decomposition Detector of MSTIDs (ADDTID), a comprehensive multi-MSTID detection technique, including the model description, justification and solution. And finally, we have successfully applied ADDTID in the simulated dense GNSS networks. The main conclusions in this chapter are the following:

- As a new and robust GNSS TIDs determining technique, ADDTID, shows a high sensitivity in detecting the TID propagation parameters from dense and large GNSS receiver networks. This has been tested in the Japan GEONET and the U.S. CORS networks.

- ADDTID can correctly recover TIDs from the 2D detrended VTEC maps in spite of the distortion due to the projection from the 3D maps, for instance about 2.35% in processing the GEONET GNSS network.
- ADDTID can correctly detect TIDs from the detrended VTEC maps with ground-based GNSS data with an elevation mask of 30 degree elevation angles.
- ADDTID shows the high robustness to the noise and distortion in maps, in particular the low signal noise ratio of the maps or data inaccuracy in the local maps.
- ADDTID can determine all the wave parameters of the TIDs, including the wavelength, propagation azimuth, propagation velocity, period, and amplitude.
- ADDTID can simultaneously detect multiple TIDs similar to the planar waves, regardless of the energies, wavelengths, azimuths, velocity, periods and unknown number of TIDs superimposed in the maps.

In chapter 2, we have studied the performance of the multi-MSTID detection algorithm on a spring equinox day of March 21, 2011. This was done by applying the ADDTID on a wide and dense networks of GNSS permanent receivers, as described in chapter 1. The method that we have presented performs better than the previous cGII method (see Hernández-Pajares et al., 2012b) in the sense that it simultaneously can detect the number of MSTID planar waves present and estimate their parameters. The method is compared with the cGII method as a benchmark. The general features of the MSTIDs estimated by the algorithm are consistent with results of previous studies, e.g. Hernández-Pajares, Juan, and Sanz (2006), Hernández-Pajares et al. (2012b), Jacobson et al. (1995), Otsuka et al. (2013), and Tsugawa et al. (2007a,b). The main contribution of the method for the study of MSTIDs can be summarized as follows:

- The distribution and tracking of simultaneous MSTID, i.e., temporal variation of the azimuth, velocity, amplitude and wavelength, and the determination of the number of MSTIDs present at a given moment.
- The observation of MSTIDs with velocities much higher than $400-600$ m/s during nighttime and the solar teminator.
- The detection of different simultaneous MSTIDs with the same azimuth, or differences of azimuth of 180 degrees.
- The detection of circular waves that are compatible (in time and space) with the occurrence of two consecutive earthquakes of low magnitude.

- The possibility of creating rules for automatically finding special distributions of the MSTIDs without a visual inspection of the VTEC maps.

In chapter 3, we have described the diverse types of ionospheric disturbances that were generated during the transit of the US solar eclipse of 21 August 2017, and compared visually with the VTEC maps and movies. The multi-TIDs detection technique, is the improved ADDTID technique, which has been used to automatically characterize the disturbances and their locations, see Yang, Monte Moreno, and Hernández-Pajares (2018). These disturbances show a rich set of different features related with the changing angle of the umbra with respect to the surface of the earth, such as the footprint, size, azimuths and velocity of umbra. Due to different patterns of behavior, the TIDs in this work have been categorized into the following phases:

- The time-varying TIDs observed in the early stage, beginning with the arrival of penumbra with 50–75% obscuration. These TID wavelengths show a global downward trend from 1125 km, and finally converge at 400 km about 4 min after the umbra arrival, when a new set of large scale TIDs appear suddenly. The time-varying and large scale TIDs show, respectively, propagation in the southeastward and northeastward directions, and are consistent with the umbra movement. These TIDs might originate from the thermosphere.
- Another set of time-varying TIDs was detected at the final stage when the penumbra was leaving the West coast. With increased wavelengths, these TIDs show the periods from 1 up to 5 h, and appear with a delay of about 1.5 h after the departure of the umbra. The TIDs could be the long-period component of bow waves originating in the middle atmosphere.
- The global LSTIDs illustrate the consistent bow wave behavior with a variable opening angle. The location and appearance of the in situ bow waves respectively follow the umbra and penumbra movement with transient delays. In particular, the opening angle of the bow related to the umbra reaches a maximum at about 3–5 min after the minimum of the velocity of umbra center at height of 250 km.
- Despite having similar wave parameters, the two MSTIDs depict two kinds of bow wave characteristics at different locations and times. For instance, the in situ MSTIDs occur in advance to the umbra, whereas the others from the middle atmosphere are present in the penumbra after the umbra departure.
- As possible effects to the ionosphere, the MSTIDs in the east US might be the soliton waves of the bow waves.

In Chapter 4, we have studied the circular MSTID associated with the Japan Tohoku earthquake / tsunami of 11 March 2011. The application of the ADDTID algorithm developed in this thesis allowed for the following contributions:

- the reliable and robust simultaneous multi-TID detection and estimation of the propagation parameters by means of the ADDTID. The results have been double checked by the additional visual inspection from detrended VTEC maps and keogram plots;
- The detection of several wavefronts between the west and east MSTIDs from the epicenter, which are consistent with the tsunami during the similar time;
- The analysis and description of the whole propagation process of the circular MSTIDs driven by the tsunami during the GNSS observable area;
- The fast and short propagation of the circular MSTIDs related to the acoustic waves of the earthquake.

As future work, we will explore extensions of the wave model to include MSTID circular or elliptic waves, which appear in the case of earthquakes and are of interest for and complement the study that we have presented. Note also that in some cases the planar wave model detects multiple distinct MSTIDs with azimuthal patterns consistent with a spherical wave. This further justifies future work to incorporate circular or ecliptic wave models. In another phase, we plan to further improve the wave detection model in order to better characterize the various wave fronts of bow waves in the ionosphere, also developing a robust discrimination tool to recognize disturbances related to different bow waves, and explore the determining technique of the bow wave parameters by means of the detected ionospheric disturbances. This model will include rules and machine learning techniques for determining automatically the different phenomena of interest. Finally, as the current implementation is retrospective, and needs high computational resources, we plan to do a reimplementation of the ADDTID algorithm, that works in real time and is able to use the Graphical Processing Units (GPUs), that would take care of the high computational load, and give real time performance. As the core part of the algorithm consists in solving linear problems, we believe that this implementation of the ADDTID algorithm might be helpful in real time, with a delay lower than one minute.

List of Related Work and Activities

Yang, Heng, Enrique Monte Moreno, and Manuel Hernández-Pajares (2018). "Detection and Description of the Different Ionospheric Disturbances that Appeared during the Solar Eclipse of 21 August 2017". In: *Remote Sensing*, 10.11, pp. 1710-1723. DOI: 10.3390/rs10111710.

Yang, Heng, Enrique Monte Moreno, and Manuel Hernández-Pajares (2017). "Multi-TID detection and characterization in a dense Global Navigation Satellite System receiver network". In: *Journal of Geophysical Research: Space Physics*, 122.9, pp. 9554-9575. DOI: 10.1002/2017JA023988.

Monte Moreno, Enrique, Alberto García-Rigo, Manuel Hernández-Pajares, and **Heng Yang** (2018). "TEC forecasting based on manifold trajectories". In: *Remote Sensing*, 10.7, pp. 2072-4292. DOI: 10.3390/rs10070988.

Hernández-Pajares, Manuel, ..., Enrique Monte-Moreno, **Heng Yang**, ... (2017). "Direct MSTID mitigation in precise GPS processing". In: *Radio Science*, 52.3, pp. 321–337. DOI: 10.1002/2016RS006159.

Graffigna, Victoria, Hernández-Pajares, Manuel, ..., **Heng Yang**, Enrique Monte-Moreno, ... (2016). "Assessing different components of the real- time GNSS precise positioning "sudoku" with TOMION software". In: *Second Satellite Geodesy and Ionosphere Research Workshop*, Berlin, Germany: august 8-9, 2016.

Hernández-Pajares, Manuel, **Heng Yang**, Enrique Monte-Moreno (2016). "New improvements on GNSS modelling of the most frequent ionospheric waves signatures". In: *Annual Meeting of the Asia Oceania Geosciences Society*, Beijing, China: Jul, 2016.

Hernández-Pajares, Manuel, ..., **Heng Yang**, Enrique Monte-Moreno, ... (2015). "Improved MSTID modelling and impact on precise GNSS processing". In: *International Colloquium Scientific and Fundamental Aspects of the Galileo Programme*, Braunschweig: Oct, 2015

Hernández-Pajares, Manuel, Enrique Monte-Moreno, **Heng Yang**, ... (2015). "Recent progress in characterizing multiscale ionospheric phenomena with GNSS and applications: Solar Flare over-ionization & Medium Scale Travelling Ionospheric Disturbances". In: *Second Satellite Geodesy and Ionosphere Research Workshop*, Berlin, Germany: July 7-8, 2015.

Hernández-Pajares, Manuel, ..., Enrique Monte-Moreno, **Heng Yang**, ... (2015). "New approaches in Medium Scale Traveling Ionospheric Disturbances modeling". In: *EGU General Assembly Conference Abstracts*, vol. 17.

Hernández-Pajares, Manuel, Enrique Monte-Moreno, **Heng Yang**, ... (2015). "PIOM-FIPP CCN: Ambiguity Resolution in GNSS Ionospheric Interferometry (ARGII) technique: consolidation and update", *Tech. rep. for Project: PIOM-FIPP CCN - Precise Ionospheric Modelling For Improved GNSS Positioning in Poland*.

Yang, Heng, Enrique Monte Moreno, and Manuel Hernández Pajares (2015). Spectral methods for time delay estimation of MSTIDs signal. *Tech. rep. Barcelona: Open institutional repositories of UPC*. URL: `http://upcommons.upc.edu/e-prints/handle/2117/26830`.

Yang, Heng, Enrique Monte Moreno, and Manuel Hernández Pajares (2015). Numerical methods for medium scale traveling ionospheric disturbances signal preprocessing. *Tech. rep. Barcelona: Open institutional repositories of UPC*. URL: `http://upcommons.upc.edu/e-prints/handle/2117/26832`.

Yang, Heng, Enrique Monte Moreno, and Manuel Hernández Pajares (2014). Solving mixed integer non-linear programming problem applied to GNSS data. *Tech. rep. Barcelona: Open institutional repositories of UPC*. URL: `http://upcommons.upc.edu/e-prints/handle/2117/26831`.

List of Publications in Preparation

Yang, Heng, Enrique Monte Moreno, and Manuel Hernández-Pajares (2019). “Detection and Determination of the Circular Ionospheric Disturbances launched by the 2011 Tohoku Earthquake / Tsunami”.

Yang, Heng, Enrique Monte Moreno, and Manuel Hernández-Pajares (2019). “Characterization of Seasonal Medium Scale Traveling Ionospheric Disturbances above North America”.

Bibliography

Afraimovich, EL et al. (2009). "MHD nature of night-time MSTIDs excited by the solar terminator". In: *Geophysical Research Letters* 36.15.

Andrews, Robert W et al. (2014). *Introduction to the Open Source PV LIB for Python Photovoltaic System Modeling Package.* Tech. rep. Sandia National Lab.(SNL-NM), Albuquerque, NM (United States).

Artru, Juliette et al. (2005a). "Ionospheric detection of gravity waves induced by tsunamis". In: *Geophysical Journal International* 160.3, pp. 840–848.

Artru, Juliette et al. (2005b). "Tsunami detection in the ionosphere". In: *Space Research Today* 163, pp. 23–27.

Bartlett, Marian Stewart, Javier R Movellan, and Terrence J Sejnowski (2002). "Face recognition by independent component analysis". In: *Neural Networks, IEEE Transactions on* 13.6, pp. 1450–1464.

Bilitza, D et al. (2017). "International Reference Ionosphere 2016: From ionospheric climate to real-time weather predictions". In: *Space Weather* 15.2, pp. 418–429.

Bilitza, Dieter et al. (2014). "The International Reference Ionosphere 2012–a model of international collaboration". In: *Journal of Space Weather and Space Climate* 4, A07.

Bullett, Terence and Justin Mabie (2018). "Vertical and Oblique Ionosphere Sounding During the 21 August 2017 Solar Eclipse". In: *Geophysical Research Letters* 45.8, pp. 3690–3697.

Candes, Emmanuel J, Michael B Wakin, and Stephen P Boyd (2008). "Enhancing sparsity by reweighted $\ell 1$ minimization". In: *Journal of Fourier analysis and applications* 14.5-6, pp. 877–905.

Chen, CH et al. (2011). "Long-distance propagation of ionospheric disturbance generated by the 2011 off the Pacific coast of Tohoku Earthquake". In: *Earth, planets and space* 63.7, p. 67.

Chen, CH et al. (2016). "Medium-scale traveling ionospheric disturbances by three-dimensional ionospheric GPS tomography". In: *Earth, Planets and Space* 68.1, pp. 1–9.

Chen, Scott Shaobing, David L Donoho, and Michael A Saunders (2001). "Atomic decomposition by basis pursuit". In: *SIAM review* 43.1, pp. 129–159.

Cheng, Kang, Yinn-Nien Huang, and Sen-Wen Chen (1992). "Ionospheric effects of the solar eclipse of September 23, 1987, around the equatorial anomaly crest region". In: *Journal of Geophysical Research: Space Physics* 97.A1, pp. 103–111.

Chilcote, M et al. (2015). "Detection of traveling ionospheric disturbances by medium-frequency Doppler sounding using AM radio transmissions". In: *Radio Science* 50.3, pp. 249–263.

Chimonas, G (1970). "Internal gravity-wave motions induced in the Earth's atmosphere by a solar eclipse". In: *Journal of Geophysical Research* 75.28, pp. 5545–5551.

Chimonas, G and CO Hines (1970a). "Atmospheric gravity waves induced by a solar eclipse". In: *Journal of Geophysical Research* 75.4, pp. 875–875.

– (1970b). "Atmospheric gravity waves launched by auroral currents". In: *Planetary and Space Science* 18.4, pp. 565–582.

Coster, Anthea J et al. (2017). "GNSS Observations of Ionospheric Variations During the 21 August 2017 Solar Eclipse". In: *Geophysical Research Letters*.

Davis, M. J. and A. V. Da Rosa (1970). "Possible Detection of Atmospheric Gravity Waves generated by the Solar Eclipse". In: *Nature* 226.5251, p. 1123.

Deng, Zhiguo et al. (2013). "Medium-scale traveling ionospheric disturbances (MSTID) modeling using a dense German GPS network". In: *Advances in Space Research* 51.6, pp. 1001–1007.

Ding, Feng et al. (2011). "Climatology of medium-scale traveling ionospheric disturbances observed by a GPS network in central China". In: *Journal of Geophysical Research: Space Physics* 116.A9.

Dow, John M, RE Neilan, and C Rizos (2009). "The international GNSS service in a changing landscape of global navigation satellite systems". In: *Journal of Geodesy* 83.3-4, pp. 191–198.

Duda, Richard O and Peter E Hart (1972). "Use of the Hough transformation to detect lines and curves in pictures". In: *Communications of the ACM* 15.1, pp. 11–15.

Eckermann, Stephen Drew et al. (2007). "Atmospheric effects of the total solar eclipse of 4 December 2002 simulated with a high-altitude global model". In: *Journal of Geophysical Research: Atmospheres* 112.D14.

Efron, Bradley et al. (2004). "Least angle regression". In: *The Annals of statistics* 32.2, pp. 407–499.

Fischler, Martin A and Robert C Bolles (1981). "Random sample consensus: a paradigm for model fitting with applications to image analysis and automated cartography". In: *Communications of the ACM* 24.6, pp. 381–395.

Fritts, David C and Zhangai Luo (1993). "Gravity wave forcing in the middle atmosphere due to reduced ozone heating during a solar eclipse". In: *Journal of Geophysical Research: Atmospheres* 98.D2, pp. 3011–3021.

Galvan, David A et al. (2012). "Ionospheric signatures of Tohoku-Oki tsunami of March 11, 2011: Model comparisons near the epicenter". In: *Radio Science* 47.4.

Grawe, Matthew A and Jonathan J Makela (2017). "Observation of tsunami-generated ionospheric signatures over Hawaii caused by the 16 September 2015 Illapel earthquake". In: *Journal of Geophysical Research: Space Physics* 122.1, pp. 1128–1136.

Hastie, T., R. Tibshirani, and J. Friedman (2009). *The Elements of Statistical Learning: Data Mining, Inference, and Prediction, Second Edition*. Springer Series in Statistics. Springer New York. ISBN: 9780387848587.

Hastie, Trevor, Robert Tibshirani, and Martin Wainwright (2015). *Statistical learning with sparsity: the lasso and generalizations*. CRC Press.

Hernández-Pajares, M., JM Juan, and J Sanz (2006). "Medium-scale traveling ionospheric disturbances affecting GPS measurements: Spatial and temporal analysis". In: *Journal of Geophysical Research: Space Physics (1978–2012)* 111.A7.

Hernández-Pajares, M. et al. (2002). "Improving the real-time ionospheric determination from GPS sites at very long distances over the equator". In: *Journal of Geophysical Research: Space Physics (1978–2012)* 107.A10, SIA–10.

Hernández-Pajares, M. et al. (2009). "The IGS VTEC maps: a reliable source of ionospheric information since 1998". In: *Journal of Geodesy* 83.3-4, pp. 263–275.

Hernández-Pajares, M. et al. (2011). "The ionosphere: effects, GPS modeling and the benefits for space geodetic techniques". In: *Journal of Geodesy* 85.12, pp. 887–907.

Hernández-Pajares, M. et al. (2012a). "GNSS measurement of EUV photons flux rate during strong and mid solar flares". In: *Space Weather* 10.12.

Hernández-Pajares, M. et al. (2012b). "Propagation of medium scale traveling ionospheric disturbances at different latitudes and solar cycle conditions". In: *Radio Science* 47.6.

Hernández-Pajares, M. et al. (2017). "Direct MSTID mitigation in precise GPS processing". In: *Radio Science* 52.3, pp. 321–337.

Hernández-Pajares, Manuel et al. (2018). "Precise ionospheric electron content monitoring from single-frequency GPS receivers". In: *GPS Solutions* 22.4, p. 102.

Hickey, MP, G Schubert, and RL Walterscheid (2009). "Propagation of tsunami-driven gravity waves into the thermosphere and ionosphere". In: *Journal of Geophysical Research: Space Physics (1978–2012)* 114.A8.

Hines, CO (1972). "Gravity waves in the atmosphere". In: *Nature* 239, pp. 73–78.

Hocke, K and K Schlegel (1996). "A review of atmospheric gravity waves and travelling ionospheric disturbances: 1982–1995". In: *Annales Geophysicae* 14.9, p. 917.

Huang, Fuqing et al. (2016). "Statistical analysis of nighttime medium-scale traveling ionospheric disturbances using airglow images and GPS observations over central China". In: *Journal of Geophysical Research: Space Physics* 121.9, pp. 8887–8899.

Huba, JD and D Drob (2017). "SAMI3 prediction of the impact of the 21 August 2017 total solar eclipse on the ionosphere/plasmasphere system". In: *Geophysical Research Letters* 44.12, pp. 5928–5935.

Hunsucker, Robert D (1982). "Atmospheric gravity waves generated in the high-latitude ionosphere: A review". In: *Reviews of Geophysics* 20.2, pp. 293–315.

Hyvärinen, Aapo, Juha Karhunen, and Erkki Oja (2004). *Independent component analysis*. Vol. 46. John Wiley & Sons.

Jacobson, Abram R et al. (1995). "Observations of traveling ionospheric disturbances with a satellite-beacon radio interferometer: Seasonal and local time behavior". In: *Journal of Geophysical Research: Space Physics (1978–2012)* 100.A2, pp. 1653–1665.

Japan World Data Center for Geomagnetism (2018). *Auroral electrojet activity index*. accessed on 4 October 2018. URL: http://wdc.kugi.kyoto-u.ac.jp/ae_provisional/201708/index_20170821.html.

Kazadzis, S et al. (2007). "Effects of total solar eclipse of 29 March 2006 on surface radiation". In: *Atmospheric Chemistry and Physics* 7.22, pp. 5775–5783.

Kelley, M. C. (2011). "On the origin of mesoscale TIDs at midlatitudes". In: *Annales Geophysicae* 29.2, pp. 361–366.

Kotake, Nobuki et al. (2006). "Climatological study of GPS total electron content variations caused by medium-scale traveling ionospheric disturbances". In: *Journal of Geophysical Research: Space Physics* 111.A4.

Kotake, Nobuki et al. (2007). "Statistical study of medium-scale traveling ionospheric disturbances observed with the GPS networks in Southern California". In: *Earth, planets and space* 59.2, pp. 95–102.

Kremer, Katrina, Guy Simpson, and Stéphanie Girardclos (2012). "Giant Lake Geneva tsunami in ad 563". In: *Nature Geoscience* 5.11, pp. 756–757.

Le, H et al. (2008). "The ionospheric responses to the 11 August 1999 solar eclipse: observations and modeling". In: *Annales geophysicae: atmospheres, hydrospheres and space sciences* 26, pp. 107–116.

Lee, Jeffrey K, Farzad Kamalabadi, and Jonathan J Makela (2008). "Three-dimensional tomography of ionospheric variability using a dense GPS receiver array". In: *Radio Science* 43.3.

Lee, MC et al. (2008). "Did tsunami-launched gravity waves trigger ionospheric turbulence over Arecibo?" In: *Journal of Geophysical Research: Space Physics* 113.A1.

Liu, Jann-Yenq et al. (2006). "Ionospheric GPS total electron content (TEC) disturbances triggered by the 26 December 2004 Indian Ocean tsunami". In: *Journal of Geophysical Research: Space Physics* 111.A5.

Liu, Jann-Yenq et al. (2011a). "Ionospheric disturbances triggered by the 11 March 2011 M9.0 Tohoku earthquake". In: *Journal of Geophysical Research: Space Physics* 116.A6.

Liu, JY et al. (2011b). "Bow and stern waves triggered by the Moon's shadow boat". In: *Geophysical Research Letters* 38.17.

Mai, Chao-Lun and Jean-Fu Kiang (2009). "Modeling of ionospheric perturbation by 2004 Sumatra tsunami". In: *Radio Science* 44.3.

Makela, JJ et al. (2011). "Imaging and modeling the ionospheric airglow response over Hawaii to the tsunami generated by the Tohoku earthquake of 11 March 2011". In: *Geophysical Research Letters* 38.24.

Maruyama, Takashi et al. (2011). "Ionospheric multiple stratifications and irregularities induced by the 2011 off the Pacific coast of Tohoku Earthquake". In: *Earth, planets and space* 63.7, p. 65.

Matsumura, M et al. (2011). "Numerical simulations of atmospheric waves excited by the 2011 off the Pacific coast of Tohoku Earthquake". In: *Earth, planets and space* 63.7, p. 68.

McInerney, Joseph M et al. (2018). "Simulation of the 21 August 2017 Solar Eclipse Using the Whole Atmosphere Community Climate Model-eXtended". In: *Geophysical Research Letters* 45.9, pp. 3793–3800.

Mevius, M et al. (2016). "Probing ionospheric structures using the LOFAR radio telescope". In: *Radio Science* 51.7, pp. 927–941.

Montenbruck, Oliver and Thomas Pfleger (2013). *Astronomy on the personal computer*. Springer.

Mori, Nobuhito, Tomoyuki Takahashi, and 2011 Tohoku Earthquake Tsunami Joint Survey Group (2012). "Nationwide post event survey and analysis of the 2011 Tohoku earthquake tsunami". In: *Coastal Engineering Journal* 54.01, pp. 1250001–1–1250001–27. DOI: 10.1142/S0578563412500015.

Müller-Wodarg, ICF, AD Aylward, and Mike Lockwood (1998). "Effects of a mid-latitude solar eclipse on the thermosphere and ionosphere-A modelling study". In: *Geophysical Research Letters* 25.20, pp. 3787–3790.

Nayak, Chinmaya and Erdal Yiğit (2018). "GPS-TEC Observation of Gravity Waves Generated in the Ionosphere During 21 August 2017 Total Solar Eclipse". In: *Journal of Geophysical Research: Space Physics* 123.1, pp. 725–738.

Occhipinti, Giovanni, E Alam Kherani, and Philippe Lognonné (2008). "Geomagnetic dependence of ionospheric disturbances induced by tsunamigenic internal gravity waves". In: *Geophysical Journal International* 173.3, pp. 753–765.

Occhipinti, Giovanni et al. (2006). "Three-dimensional waveform modeling of ionospheric signature induced by the 2004 Sumatra tsunami". In: *Geophysical research letters* 33.20.

Occhipinti, Giovanni et al. (2011). "Three-dimensional numerical modeling of tsunami-related internal gravity waves in the Hawaiian atmosphere". In: *Earth, planets and space* 63.7, p. 61.

Ogawa, T et al. (2009). "Medium-scale traveling ionospheric disturbances observed with the SuperDARN Hokkaido radar, all-sky imager, and GPS network and their relation to concurrent sporadic E irregularities". In: *Journal of Geophysical Research: Space Physics* 114.A3.

Oinats, Alexey V, Vladimir I Kurkin, and Nozomu Nishitani (2015). "Statistical study of medium-scale traveling ionospheric disturbances using SuperDARN Hokkaido ground backscatter data for 2011". In: *Earth, Planets and Space* 67.1, pp. 1–9.

Otsuka, Y et al. (2004). "Geomagnetic conjugate observations of medium-scale travelling ionospheric disturbances at midlatitude using all-sky airglow imagers". In: *Geophysical research letters* 31.15.

Otsuka, Y et al. (2011). "Statistical study of medium-scale traveling ionospheric disturbances observed with a GPS receiver network in Japan". In: *Aeronomy of the Earth's Atmosphere and Ionosphere*. Springer, pp. 291–299.

Otsuka, Y et al. (2013). "GPS observations of medium-scale traveling ionospheric disturbances over Europe". In: *Annales Geophysicae* 31.2, pp. 163–172.

Peltier, WR and CO Hines (1976). "On the possible detection of tsunamis by a monitoring of the ionosphere". In: *Journal of Geophysical Research* 81.12, pp. 1995–2000.

Rasmussen, Carl Edward and Christopher K. I. Williams (2005). *Gaussian Processes for Machine Learning (Adaptive Computation and Machine Learning)*. The MIT Press. ISBN: 026218253X.

Reddy, CD et al. (2017). "Ionospheric Plasma Response to Mw 8.3 Chile Illapel Earthquake on September 16, 2015". In: *The Chile-2015 (Illapel) Earthquake and Tsunami*. Springer, pp. 145–155.

Reinisch, BW et al. (2018). "Investigation of the electron density variation during the 21 August 2017 solar eclipse". In: *Geophysical Research Letters* 45.3, pp. 1253–1261.

Rolland, Lucie M et al. (2010). "Ionospheric gravity waves detected offshore Hawaii after tsunamis". In: *Geophysical Research Letters* 37.17.

Rolland, Lucie M et al. (2011). "The resonant response of the ionosphere imaged after the 2011 off the Pacific coast of Tohoku Earthquake". In: *Earth, planets and space* 63.7, p. 62.

Sagiya, Takeshi (2004). "A decade of GEONET: 1994–2003". In: *Earth, planets and space* 56.8, pp. xxix–xli.

Saito, A, S Fukao, and S Miyazaki (1998). "High resolution mapping of TEC perturbations with the GSI GPS network over Japan". In: *Geophysical research letters* 25.16, pp. 3079–3082.

Saito, A et al. (2011). "Acoustic resonance and plasma depletion detected by GPS total electron content observation after the 2011 off the Pacific coast of Tohoku Earthquake". In: *Earth, planets and space* 63.7, pp. 863–867.

Salah, JE et al. (1986). "Observations of the May 30, 1984, annular solar eclipse at Millstone Hill". In: *Journal of Geophysical Research: Space Physics* 91.A2, pp. 1651–1660.

Shiokawa, K et al. (2003). "Statistical study of nighttime medium-scale traveling ionospheric disturbances using midlatitude airglow images". In: *Journal of Geophysical Research: Space Physics (1978–2012)* 108.A1.

Snay, Richard A and Tomás Soler (2008). "Continuously operating reference station (CORS): history, applications, and future enhancements". In: *Journal of Surveying Engineering* 134.4, pp. 95–104.

Song, Y Tony et al. (2012). "Merging tsunamis of the 2011 Tohoku-Oki earthquake detected over the open ocean". In: *Geophysical Research Letters* 39.5.

Ssessanga, Nicholas, Yong Ha Kim, and Eunsol Kim (2015). "Vertical structure of medium-scale traveling ionospheric disturbances". In: *Geophysical Research Letters* 42.21, pp. 9156–9165.

Stankov, Stanimir M et al. (2017). "Multi-instrument observations of the solar eclipse on 20 March 2015 and its effects on the ionosphere over Belgium and Europe". In: *Journal of Space Weather and Space Climate* 7, A19.

Stefanello, MB et al. (2015). "OI 630.0 nm all-sky image observations of medium-scale traveling ionospheric disturbances at geomagnetic conjugate points". In: *Journal of Atmospheric and Solar-Terrestrial Physics* 128, pp. 58–69.

Sun, Yang-Yi et al. (2018). "Ionospheric bow wave induced by the moon shadow ship over the continent of United States on 21 August 2017". In: *Geophysical Research Letters*.

Tibshirani, Robert (1996). "Regression shrinkage and selection via the lasso". In: *Journal of the Royal Statistical Society. Series B (Methodological)*, pp. 267–288.

Tsugawa, T, A Saito, and Y Otsuka (2004). "A statistical study of large-scale traveling ionospheric disturbances using the GPS network in Japan". In: *Journal of Geophysical Research: Space Physics* 109.A6.

Tsugawa, T et al. (2011). "Ionospheric disturbances detected by GPS total electron content observation after the 2011 off the Pacific coast of Tohoku Earthquake". In: *Earth, planets and space* 63.7, pp. 875–879.

Tsugawa, Takuya et al. (2006). "Geomagnetic conjugate observations of large-scale traveling ionospheric disturbances using GPS networks in Japan and Australia". In: *Journal of Geophysical Research: Space Physics* 111.A2.

Tsugawa, Takuya et al. (2007a). "Medium-scale traveling ionospheric disturbances detected with dense and wide TEC maps over North America". In: *Geophysical Research Letters* 34.22.

Tsugawa, Takuya et al. (2007b). "Medium-scale traveling ionospheric disturbances observed by GPS receiver network in Japan: A short review". In: *GPS Solutions* 11.2, pp. 139–144.

U.S. Geological Survey (2011a). *Earthquake Facts and Statistics*. Date: 2011-03-21 08:06:22 UTC, Mw 4.9, Location: 36.452°N, 141.537°E, Depth: 21.4 km, near the east coast of Honshu, Japan, accessed on 8 April, 2019. URL: https://earthquake.usgs.gov/earthquakes/eventpage/usp000hy50#executive.

– (2011b). *Earthquake Facts and Statistics*. Date: 2011-03-21 08:09:26 UTC, Mw 4.6, Location: 39.195°N, 142.625°E, Depth: 49.9 km, near the east coast of Honshu, Japan, accessed on 8 April, 2019. URL: https://earthquake.usgs.gov/earthquakes/eventpage/usp000hy51#executive.

U.S. NASA Goddard Space Flight Center (2012). *Community Coordinated Modeling Center: International Reference Ionosphere 2012 Database*. accessed on 1 March 2019. URL: https://ccmc.gsfc.nasa.gov/modelweb/models/iri2012_vitmo.php.

– (2016). *Community Coordinated Modeling Center: International Reference Ionosphere 2016 Database*. accessed on 1 March 2019. URL: https://ccmc.gsfc.nasa.gov/modelweb/models/iri2016_vitmo.php.

U.S. NOAA National Centers for Environmental Information (2011a). *Geomagnetic Data*. accessed on 20 July 2016. URL: https://www.ngdc.noaa.gov/geomag/data.shtml.

– (2011b). *National Geophysical Data Center / World Data Service: Global Historical Tsunami Database*. accessed on 20 July 2016. DOI: 10.7289/V5PN93H7.

– (2011c). *National Geophysical Data Center / World Data Service: Global Significant Earthquake Database*. accessed on 20 July 2016. DOI: 10.7289/V5TD9V7K.

– (2011d). *Solar Data Services: Sun, solar activity and upper atmosphere data*. accessed on 20 July 2016. URL: https://www.ngdc.noaa.gov/stp/solar/solardataservices.html.

– (2017a). *Geomagnetic Data*. accessed on 1 March 2018. URL: https://www.ngdc.noaa.gov/geomag/data.shtml.

– (2017b). *National Geophysical Data Center / World Data Service: Global Historical Tsunami Database*. accessed on 1 March 2018. DOI: 10.7289/V5PN93H7.

– (2017c). *National Geophysical Data Center / World Data Service: Global Significant Earthquake Database*. accessed on 1 March 2018. DOI: 10.7289/V5TD9V7K.

– (2017d). *Solar Data Services: Sun, solar activity and upper atmosphere data*. accessed on 1 March 2018. URL: https://www.ngdc.noaa.gov/stp/solar/solardataservices.html.

Wright, John et al. (2009). "Robust face recognition via sparse representation". In: *Pattern Analysis and Machine Intelligence, IEEE Transactions on* 31.2, pp. 210–227.

Wu, Chen et al. (2018). "GITM-Data Comparisons of the Depletion and Enhancement During the 2017 Solar Eclipse". In: *Geophysical Research Letters* 45.8, pp. 3319–3327.

Yang, Heng (2018a). *Ionospheric disturbance movie, from CORS GNSS network, for all GPS satellites, Aug. 21, 2017, 15:00-22:00 UT*. accessed on 8 October 2018. URL: https://youtu.be/zsWsSRD3bcQ.

– (2018b). *Ionospheric disturbance movie, from CORS GNSS network, for GPS satellite PRN12, Aug. 21, 2017, 15:00-22:00 UT*. accessed on 8 October 2018. URL: https://youtu.be/O8eYn-0jLX4.

– (2018c). *Ionospheric disturbance movie, from CORS GNSS network, for GPS satellite PRN2, Aug. 21, 2017, 15:00-22:00 UT*. accessed on 8 October 2018. URL: https://youtu.be/g1IQnLBX6cc.

– (2019a). *Ionospheric disturbance movie, detrended by 300 sec interval double difference, from GEONET GNSS network, for all GPS satellites, March 11, 2011, 04:00-10:00 UT*. accessed on 4 Apr. 2019. URL: https://youtu.be/oWtDLQ8OL30.

– (2019b). *Ionospheric disturbance movie, detrended by 60 sec interval double difference, from GEONET GNSS network, for all GPS satellites, March 11, 2011, 04:00-10:00 UT*. accessed on 4 Apr. 2019. URL: https://youtu.be/gTwKM-XKtoA.

Yang, Heng, Enrique Monte-Moreno, and Manuel Hernández-Pajares (2017). "Multi-TID detection and characterization in a dense Global Navigation Satellite System receiver network". In: *Journal of Geophysical Research: Space Physics* 122.9, pp. 9554–9575. DOI: 10.1002/2017JA023988.

– (2018). "Detection and Description of the Different Ionospheric Disturbances that Appeared during the Solar Eclipse of 21 August 2017". In: *Remote Sensing* 10.11, pp. 1710–1723. DOI: 10.3390/rs10111710.

Zerefos, CS et al. (2007). "Evidence of gravity waves into the atmosphere during the March 2006 total solar eclipse". In: *Atmospheric Chemistry and Physics* 7.18, pp. 4943–4951.

Zhang, Shun-Rong et al. (2017). "Ionospheric bow waves and perturbations induced by the 21 August 2017 solar eclipse". In: *Geophysical Research Letters* 44.24.